



1992-03

# Nonlinear Response of Cylindrical Shells to Underwater Explosion: Testings and Numerical Prediction Using USA/DYNA3D / June 1, 1991 - March 1, 1992



Calhoun is a project of the Dudley Knox Library at NPS, furthering the precepts and goals of open government and government transparency. All information contained herein has been approved for release by the NPS Public Affairs Officer.

**Dudley Knox Library / Naval Postgraduate School  
411 Dyer Road / 1 University Circle  
Monterey, California USA 93943**

AD-A251 945

NPS-ME-92-002



2

# NAVAL POSTGRADUATE SCHOOL Monterey, California



**S** DTIC  
ELECTE  
JUN 05 1992  
**A** **D**

NONLINEAR RESPONSE OF CYLINDRICAL  
SHELLS TO UNDERWATER EXPLOSION:  
TESTINGS AND NUMERICAL PREDICTION  
USING USA/DYNA3D

by

LCDR P. K. Fox, USN  
Professor Y. W. Kwon, Co-Investigator  
Professor Y. S. Shin, Principal Investigator

June 1, 1991 - March 1, 1992

Approved for public release; distribution unlimited

92-14818

Prepared for: Defense Nuclear Agency  
Alexandria, VA. 20311

Naval Postgraduate School  
Monterey, CA 93943

2 6 01 037

Naval Postgraduate School  
Monterey, California

Real Admiral R. W. West, Jr.  
Superintendent

H. Shull  
Provost

This report was prepared for and funded by both Defense Nuclear Agency,  
Alexandria, VA 20311 and Naval Postgraduate School, Monterey, CA 93943.

This report was prepared by:

[Redacted]

P. K. Fox  
LCDR, USN

[Redacted]

Y. W. Kwon  
Assistant Professor of Mechanical Engineering

[Redacted]

Y. S. Shin  
Professor of Mechanical Engineering

Reviewed by:

[Redacted]

Anthony J. Healey  
Chairman  
Dept. of Mechanical Engineering

Released by:

[Redacted]

Paul J. Marto  
Dean of Research

Unclassified

SECURITY CLASSIFICATION OF THIS PAGE

REPORT DOCUMENTATION PAGE

1a. REPORT SECURITY CLASSIFICATION <b>Unclassified</b>		1b. RESTRICTIVE MARKINGS	
2a. SECURITY CLASSIFICATION AUTHORITY		3. DISTRIBUTION/AVAILABILITY OF REPORT	
2b. DECLASSIFICATION/DOWNGRADING SCHEDULE		Approved for public release: Distribution is unlimited.	
4. PERFORMING ORGANIZATION REPORT NUMBER(S)		5. MONITORING ORGANIZATION REPORT NUMBER(S)	
6a. NAME OF PERFORMING ORGANIZATION Naval Postgraduate School	6b. OFFICE SYMBOL (if applicable) ME	7a. NAME OF MONITORING ORGANIZATION Naval Postgraduate School	
6c. ADDRESS (City, State, and ZIP Code) Monterey, CA 93943-5000		7b. ADDRESS (City, State, and ZIP Code) Monterey, CA 93943-5000	
8a. NAME OF FUNDING/SPONSORING ORGANIZATION Defense Nuclear Agency/NPS	8b. OFFICE SYMBOL (if applicable)	9. PROCUREMENT INSTRUMENT IDENTIFICATION NUMBER	
8c. ADDRESS (City, State, and ZIP Code) DNA: Alexandria, VA 22310 NPS: Monterey, CA 93943		10. SOURCE OF FUNDING NUMBERS	
		PROGRAM ELEMENT NO.	PROJECT NO.
		TASK NO.	WORK UNIT ACCESSION NO.
11. TITLE (Include Security Classification) Nonlinear Response of Cylindrical Shells To Underwater Explosion: Testings and Numerical Prediction Using USA/DYNA3D			
12. PERSONAL AUTHOR(S) P. K. Fox, Y. K. Kwon and Y. S. Shin			
13a. TYPE OF REPORT Progress Report	13b. TIME COVERED FROM 6/91 TO 3/92	14. DATE OF REPORT (Year, Month, Day) 1992, March 1	15. PAGE COUNT 135
16. SUPPLEMENTARY NOTATION The views expressed are those of the authors and do not reflect the official policy or position of DoD or US Government.			
17. COSATI CODES		18. SUBJECT TERMS (Continue on reverse if necessary and identify by block number)	
FIELD	GROUP	SUB-GROUP	
		Underwater Explosion	
19. ABSTRACT (Continue on reverse if necessary and identify by block number) Nonlinear 3-D Dynamic Analysis Code (VEC/DYNA3D) has been interfaced with Underwater Shock Analysis Code (USA) and capabilities were developed to perform numerical analysis of submerged and semi-submerged marine structures subjected to underwater explosion. A series of numerical analysis were performed to determine the elastic and elasto-plastic responses of cylindrical shell type structures. The results were favorably compared with those of underwater explosion testings. The coupled code USA/DYNA3D makes possible to predict shock-induced damage response of naval structure. In addition, numerical sensitivity analyses were undertaken to determine the importance of various physical and numerical modeling factors. This study showed clearly three types of response modes of cylinder subjected to a side-on explosion: accordion mode, breathing mode and whipping mode.			
20. DISTRIBUTION/AVAILABILITY OF ABSTRACT <input checked="" type="checkbox"/> UNCLASSIFIED/UNLIMITED <input type="checkbox"/> SAME AS RPT <input type="checkbox"/> DTIC USERS		21. ABSTRACT SECURITY CLASSIFICATION <b>Unclassified</b>	
22a. NAME OF RESPONSIBLE INDIVIDUAL Y.W. Kwon/Y.S. Shin		22b. TELEPHONE (Include Area Code) 408-646-3385	22c. OFFICE SYMBOL

**Best  
Available  
Copy**

### ABSTRACT

The coupling was made between a structural analysis code (VEC/DYNA3D) and an underwater shock analysis code (USA). The coupled computer program (USA/DYNA3D) was verified using a set of benchmark problems which had known analytical solutions. The benchmark problems were elastic analyses of a spherical and an infinite cylinder subjected to a plane wave. The comparison between the numerical and analytical solutions was very good.

An underwater explosion test was performed with an aluminum cylinder subjected to a far field, side on explosion. A pre-shot calculation using USA/DYNA3D determined critical locations to measure both axial and hoop strains of the cylinder. After the experiments, a post-shot calculation was undertaken using the free field pressure obtained from the physical experiment. The numerical results obtained using the elastoplastic analysis were very comparable to the experimental data except for some positions.

A series of numerical experiments were performed to determine the cause of the difference between the numerical and experimental results at some positions. It was found from the experimental data that there might be some rotation in the cylinder relative to the explosive. Considering the rotation in the numerical model improved the comparison. In addition, numerical sensitivity analyses were undertaken to determine the importance of various physical and numerical modelling factors.

Finally, this study showed there were three major response modes of the cylinder subjected to a side on explosion. They were the accordion mode, breathing mode as well as the whipping mode. Large plastic strains occurred at the center of the cylinder on the reverse side to the explosive and near the ends of the cylinder on the near side to the explosive. The large plastic strains seemed to be related to the whipping motion.



Accession For	
NTIS CRA&I	<input checked="" type="checkbox"/>
DTIC TAB	<input type="checkbox"/>
Unannounced	<input type="checkbox"/>
Justification .....	
By .....	
Distribution /	
Availability Codes	
Dist	Avail and/or Special
A-1	

## TABLE OF CONTENTS

I.	INTRODUCTION . . . . .	1
II.	NUMERICAL CODE DESCRIPTION AND VALIDATION . . . . .	3
	A. GENERAL DESCRIPTION OF THE METHOD . . . . .	3
	B. VEC/DYNA3D FINITE ELEMENT METHOD CODE . . . . .	3
	C. USA BOUNDARY ELEMENT METHOD CODE . . . . .	6
	D. COMPUTER CODE VERIFICATION . . . . .	7
	1. DETAILED DESCRIPTION OF THE SPHERICAL MODEL . . . . .	7
	2. DETAILED DESCRIPTION OF THE INFINITE CYLINDER MODEL . . . . .	11
III.	EXPERIMENTAL METHOD AND DESCRIPTION OF MODELS . . . . .	23
	A. DESCRIPTION OF PHYSICAL MODEL USED FOR THE FAR FIELD STUDY . . . . .	23
	B. UNDERWATER EXPLOSION TEST . . . . .	24
	C. NUMERICAL MODEL . . . . .	29
IV.	FAR FIELD STUDY RESULTS . . . . .	39
	A. EXPERIMENTAL TO NUMERICAL COMPARISON . . . . .	39
	B. SENSITIVITY ANALYSES . . . . .	47
	1. END EFFECT SENSITIVITY ANALYSIS . . . . .	48
	2. SHELL FORMULATION, QUADRATURE RULE AND INTEGRATION TIME INCREMENT SENSITIVITY ANALYSES . . . . .	53
	3. ROTATION SENSITIVITY ANALYSIS . . . . .	64
	4. PHYSICAL FINDINGS . . . . .	72
	a. RESPONSE MODES . . . . .	72
	b. ROTATIONAL EFFECTS . . . . .	76
V.	CONCLUSIONS AND RECOMMENDATIONS . . . . .	80
	A. CONCLUSIONS. . . . .	80
	1. NUMERICAL MODELLING . . . . .	80
	2. PHYSICAL ASPECTS . . . . .	81
	B. RECOMMENDATIONS. . . . .	81
	1. TOPICS FOR ADDITIONAL STUDY. . . . .	81
	a. WELDING FABRICATION EFFECTS. . . . .	81
	b. EIGHT NODE BRICK SHELL SENSITIVITY ANALYSES. . . . .	82
	c. FAILURE CRITERIA. . . . .	82
	d. NEAR FIELD EXPERIMENTATION . . . . .	82
	2. RECOMMENDATIONS TO IMPROVE TEST CONTROL. . . . .	83

APPENDIX A - SPHERICAL VALIDATION MODEL . . . . .	86
A. INGRID PRE-PROCESSOR INPUT DATA . . . . .	87
B. INGRID PRE-PROCESSOR OUTPUT DATA . . . . .	88
C. FLUMAS PRE-PROCESSOR DATA . . . . .	100
D. AUGMAT PRE-PROCESSOR DATA . . . . .	101
E. TIMINT PRE-PROCESSOR INPUT DATA . . . . .	102
APPENDIX B - INFINITE CYLINDER VALIDATION INPUT DATA .	103
A. INGRID PRE-PROCESSOR INPUT DATA . . . . .	104
B. INGRID PRE-PROCESSOR OUTPUT DATA . . . . .	105
C. FLUMAS PRE-PROCESSOR INPUT DATA . . . . .	108
D. AUGMAT PRE-PROCESSOR DATA . . . . .	109
E. TIMINT PRE-PROCESSOR DATA . . . . .	110
APPENDIX C - UNDEX TEST REPORT . . . . .	109



## LIST OF TABLES

Figure II.1.	Elastic sphere test case model. . . . .	8
Figure II.2.	Elastic cylinder test case geometry. . .	8
Figure II.3.	Spherical model verification results. . .	10
Figure II.4.	Infinite cylinder problem geometry. . .	12
Figure II.5.	Infinite cylinder validation model. . .	13
Figure II.6.	Infinite cylinder oscillation reduction (near element). . . . .	14
Figure II.7.	Infinite cylinder model oscillation removal (far element). . . . .	15
Figure II.8.	Infinite cylinder results with $\eta=0.0$ . . .	17
Figure II.9.	Infinite cylinder results with $\eta=0.25$ . . .	18
Figure II.10.	Infinite cylinder results with $\eta=0.50$ . . .	19
Figure II.11.	Infinite cylinder results with $\eta=0.75$ . . .	20
Figure II.12.	Infinite cylinder results with $\eta=1.0$ . . .	21
Figure III.1.	Undex test profile. . . . .	26
Figure III.2.	Undex test general arrangement. . . . .	27
Figure III.3.	Undex test instrumentation diagram. . . .	28
Figure III.4.	Low density, full model . . . . .	29
Figure III.5.	Refined mesh model. . . . .	30
Figure III.6.	Effective plastic strain pattern on cylinder side nearest the explosive charge. . . . .	32
Figure III.7.	Effective plastic strain pattern on cylinder side most remote from the charge. . . . .	32
Figure III.8.	Mesh sensitivity comparison for surface of shell located nearest the explosive charge (location B1). . . . .	34
Figure III.9.	Mesh sensitivity comparison for position with largest plastic strain (locations A1 and C1). . . . .	35
Figure III.10.	Mesh sensitivity comparison for point on cylinder most circumferentially remote from the charge (location B3). . . . .	36
Figure III.11.	Undex pressure profile. . . . .	38
Figure IV.1.	Experimental/numerical comparison for position A1 axial strain. . . . .	42
Figure IV.2.	Experimental/numerical comparison for position A2 hoop strain. . . . .	42
Figure IV.3.	Experimental/numerical comparison for position A2 axial strain. . . . .	43
Figure IV.4.	Experimental/numerical comparison for position B1 hoop strain. . . . .	43
Figure IV.5.	Experimental/numerical comparison for position B1 axial strain. . . . .	44

Figure IV.6.	Experimental/numerical comparison for position B2 hoop strain. . . . .	44
Figure IV.7.	Experimental/numerical comparison for position B2 axial strain. . . . .	45
Figure IV.8.	Experimental/numerical comparison for position B3 hoop strain. . . . .	45
Figure IV.9.	Experimental/numerical comparison for position B3 axial strain. . . . .	46
Figure IV.10.	Experimental/numerical comparison for position C1 axial strain. . . . .	46
Figure IV.11.	Experimental/numerical comparison for position C2 hoop strain. . . . .	47
Figure IV.12.	End effect sensitivity results. (A1 axial) . . . . .	50
Figure IV.13.	End effect sensitivity results. (A2 Hoop) . . . . .	51
Figure IV.14.	End effect sensitivity results. (A2 Axial) . . . . .	51
Figure IV.15.	End effect sensitivity results. (C1 Axial) . . . . .	52
Figure IV.16.	End effect sensitivity results. (C2 Hoop) . . . . .	52
Figure IV.17.	Shell formulation sensitivity results. (A1 Axial) . . . . .	56
Figure IV.18.	Shell formulation sensitivity results. (A2 Hoop) . . . . .	57
Figure IV.19.	Shell formulation sensitivity results (A2 Axial) . . . . .	57
Figure IV.20.	Shell formulation sensitivity results. (B1 Hoop) . . . . .	58
Figure IV.21.	Shell formulation sensitivity results. (B1 Axial) . . . . .	58
Figure IV.22.	Shell formulation sensitivity results. (B2 Hoop) . . . . .	59
Figure IV.23.	Shell formulation sensitivity results. (B2 Axial) . . . . .	59
Figure IV.24.	Shell formulation sensitivity results. (B3 Hoop) . . . . .	60
Figure IV.25.	Shell formulation sensitivity results. (B3 Axial) . . . . .	60
Figure IV.26.	Shell formulation sensitivity results. (C1 Axial) . . . . .	61
Figure IV.27.	Shell formulation sensitivity results. (C2 Hoop) . . . . .	61
Figure IV.28.	Effect of changing quadrature rule and time integration increment at location of highest strain (A1 and C1 hoop). . . . .	62
Figure IV.29.	Rotation sensitivity results. (A1 Hoop) . . . . .	65
Figure IV.30.	Rotation sensitivity results. (A1 Axial) . . . . .	65

Figure IV.31.	Rotation sensitivity results. (A2 Hoop) . . . . .	66
Figure IV.32.	Rotation sensitivity results. (A2 Axial) . . . . .	66
Figure IV.33.	Rotation sensitivity results. (B1 Hoop) . . . . .	67
Figure IV.34.	Rotation sensitivity results. (B1 Axial) . . . . .	67
Figure IV.35.	Rotation sensitivity results. (B2 Hoop) . . . . .	68
Figure IV.36.	Rotation sensitivity results. (B2 Axial) . . . . .	68
Figure IV.37.	Rotation sensitivity results. (B3 Hoop) . . . . .	69
Figure IV.38.	Rotation sensitivity results. (B3 Axial) . . . . .	69
Figure IV.39.	Rotation sensitivity results. (C1 Hoop) . . . . .	70
Figure IV.40.	Rotation sensitivity results. (C1 Axial) . . . . .	70
Figure IV.41.	Rotation sensitivity results. (C2 Hoop) . . . . .	71
Figure IV.42.	Rotation sensitivity results. (C2 Axial) . . . . .	71
Figure IV.43.	Cylinder accordion motion. . . . .	73
Figure IV.44.	Cylinder whipping motion in plane parallel to shock wave direction. . . . .	74
Figure IV.45.	Cylinder curvature as a result of whipping motion (scale factor 20). . . . .	75
Figure IV.46.	Cylinder breathing motion perpendicular to the shock wave direction of travel. . . . .	76
Figure IV.47.	Illustration of cylinder breathing mode at two different times (scale factor 40). . . . .	77
Figure IV.48.	Effective plastic strain distribution for near and remote side of cylinder with 7.5 degrees of rotation. . . . .	79

## I. INTRODUCTION

A research program is underway at the Naval Post Graduate School to study numerical modeling of ship structures subjected to both near and far field underwater explosions. This program is expected to improve the understanding of factors affecting the reliability of numerical models. In addition, it will provide insight into the dynamic response of surface ship and submarine hulls and the physics that lead to failure when a hull is subjected to an underwater shock wave. The current study centers around simple cylinders constructed of a homogenous material. Future studies will include more complex materials and structures as experience increases and the reliability of the numerical models is proven.

This paper describes progress of the research program to date and the expected line of future research. Previous results of this research program were provided in references 1-2. This report will describe the results of two numerical verification tests which were performed to prove the validity of a computer code software link which was developed for this project. It will also compare the numerical results with experimental results obtained from a underwater explosion test of an aluminum cylinder subjected to a side on attack. In addition, analyses were performed to determine the sensitivity of the results to mesh refinement, boundary effects, rotation

from expected configuration, and use of different types of shell elements. Results show that the computer code closely models simple known analytic results, and can provide close correlation to experimental results. Most of the inconsistencies between experimental and numerical results are most likely caused by uncertainties associated with physical model fabrication and the underwater explosion test rather than a failure of the numerical method to provide correct answers. Recommendations will be provided to improve control of future underwater explosion tests. Finally, preparations for future testing will be described and recommendations for additional study are provided.

## II. NUMERICAL CODE DESCRIPTION AND VALIDATION

### A. GENERAL DESCRIPTION OF THE METHOD

The primary purpose of this study was to match numerical results obtained from a computer program with experimental results from an underwater explosion test. For this initial study of a side on attack, a relatively simple model was used. The model consisted of a unstiffened, right circular cylinder constructed of a homogeneous material submerged in water. The cylinder was modelled using a dynamic finite element method (FEM) code called VEC/DYNA3D and the water was modelled using a boundary element method (BEM) code called USA (Underwater Shock Analyzer). The linkage between the two codes was developed in 1991 at the request of the Naval Post Graduate school under funding provided by the Defense Nuclear Agency (DNA).

### B. VEC/DYNA3D FINITE ELEMENT METHOD CODE

VEC/DYNA3D [Ref. 3] is an explicit finite element code. It has been used successfully for various types of nonlinear engineering problems since its conception in 1976. VEC/DYNA3D was selected for this study for several reasons. First, as stated above, VEC/DYNA3D is an explicit code. This attribute has two distinct advantages and two disadvantages. The advantages are its relatively high speed and its ability to be

implemented on a relatively small stand alone engineering work station. Initial work for this study is being performed on IBM RISC 6000 work stations. Once the USA/DYNA3D interface is proven to be reliable and accurate and experience has been gained in the use of the software, work will begin on more complex models using main frame type computers. Therefore it was important to obtain a code that was able to work significant problems on a small work station and yet be compatible with the main frames expected to be used in the future. DYNA3D is compatible with a full range of engineering work stations and has been implemented on the Los Alamos CRAY computer. Problems including up to 20000 solid elements have been run on work stations with 16 megabytes of random access memory.

The first disadvantage associated with the explicit numerical code is that the code is not inherently stable. This means that any problems dealing with time integration, including the underwater shock problems included in this study must be treated with care. Integration time steps must be matched closely with the size of the elements in the problem. This is performed automatically by DYNA3D in the stand alone mode. However, when coupled with the USA code, this automation is no longer functional. Incorrect selection of integration time steps can lead to significant oscillations and inaccuracies in the final solution. The second problem associated with the explicit codes is the mesh reflection

effect. Non-uniform meshes result in inaccurate solutions due to mesh reflection. Two factors appear to be important in ensuring that correct solution was obtained. The first is mesh size and the second is total mass of neighboring elements. Sensitivity analyses indicate that error in the final solution is relatively small if neighboring elements are kept within ten percent of each other in size. This was used as a rule of thumb in performance of this study. This led to some inefficiency in obtaining solutions since often refinement had to be performed over a larger area of the mesh to obtain a mesh independent solution than might normally be required in an implicit code. The additional area means more total elements and a subsequent increase in computation time to obtain the problem solution. These disadvantages can be overcome through careful planning. In general, they did not significantly overshadow the benefits associated with using an explicit code.

The second reason for selecting VEC/DYNA3D was its wide range of available material models and equations of state including the ability to model strain rate sensitivity, explosive materials and acoustic media. In addition, VEC/DYNA3D has a large degree of interactivity when used with the INGRID pre-processor [Ref. 4] and TAURUS post-processor [Ref. 5]. Changes can be entered with relative ease using the pre-processor and most physical components can be obtained



through knowledgeable use of the post-processor once the calculations are complete.

### **C. USA BOUNDARY ELEMENT METHOD CODE**

The Underwater Shock Analyzer (USA) computer code [Ref. 6] is a boundary element computer code based on the Doubly Asymptotic Approximation (DAA) theory developed by Geers in 1971 (Ref. 7). Through the use of the DAA theory and the boundary element formulation, USA computes the acoustic pressure loading and added mass matrices which represent the fluid surrounding the submerged shell. The acoustic pressure loading and added mass are applied at selected wetted nodes. This formulation has the benefit of significantly decreasing the number of elements required to model the submerged system since external water elements need not be included in the calculations. The reduced number of elements requires substantially less time and storage space to obtain a solution.

However, it must be noted that this code has limitations which result directly from the fundamental assumptions associated with the DAA theory (Ref. 6). First, DAA is not theoretically appropriate for concave or multiple structures or near surface problems involving convex bodies. However, studies show that only results in highly shadowed, closely spaced areas or regions of strong concavity are affected. Secondly, DAA requires that the source of the incident wave be

sufficiently removed from the structure since it can only account for acoustic waves and not hydrodynamic flow. Finally, the DAA theory is based on an early time (high frequency) approximation coupled with a late time (low frequency) approximation. Therefore, although the DAA solution will be very good at early times when the high frequency approximation is dominant and at late times when the low frequency approximation is dominant, it can vary significantly from the analytic or exact solution during intermediate times when neither the high or low frequency solution is dominant. A detailed description of DAA theory is provided by reference 7.

#### **D. COMPUTER CODE VERIFICATION**

Since the USA/DYNA3D interface was new and had not been tested, some effort was expended on performing a verification of the performance of the code. To perform the verification, two cases with known analytic results were modelled using the USA/DYNA3D code. The first case was a quarter cylinder and the second was an infinite cylinder. Results were satisfactory for both cases and the code interface is believed to be performing correctly.

##### **1. DETAILED DESCRIPTION OF THE SPHERICAL MODEL**

The numerical study was performed on a quarter symmetry model of a sphere containing 150 elements. Figure II.1 shows the model and figure II.2 shows the test geometry.

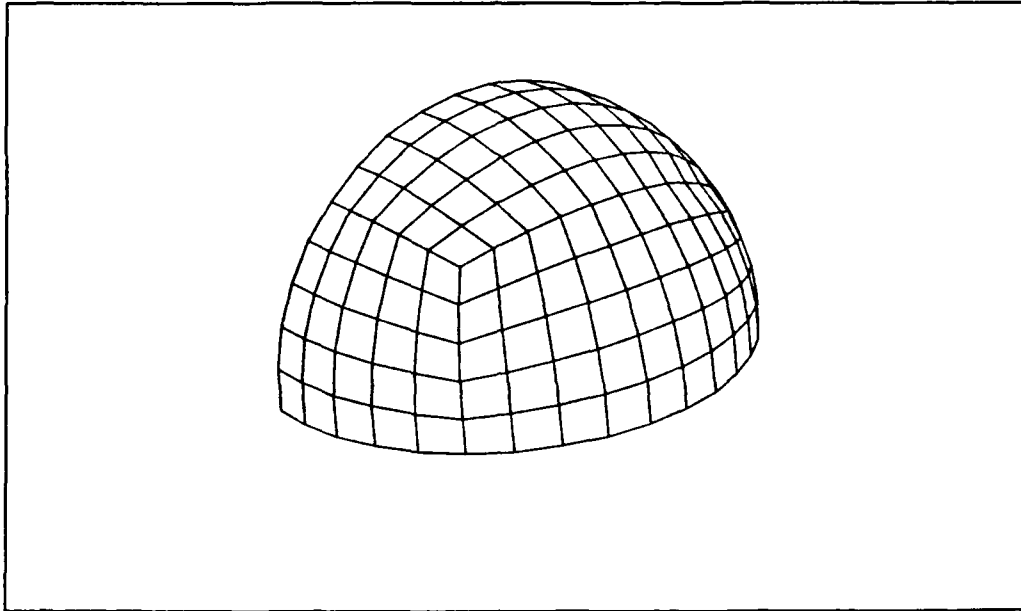


Figure II.1. Elastic sphere test case model.

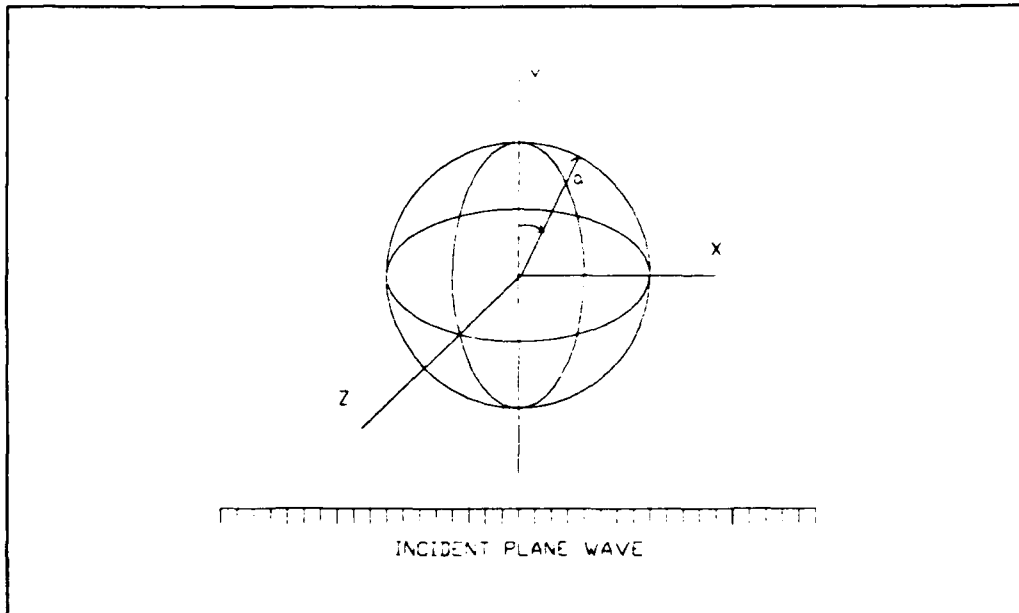


Figure II.2. Elastic cylinder test case geometry.

The thickness to diameter ratio of the shell is 1 to 50 and the shell is constructed of steel. The excitation is provided by a very small step pressure wave. As a result, the shell response is considered to be completely elastic. The case was run using the elastic material model of DYNA3D and, since results are being compared to the analytic results found in reference 8, the same material and water properties as those found in reference 8 were used. As stated in reference 8, the exact solution is obtained from separation of variables as shown in reference 9. The material and water properties used are listed below:

Steel Properties

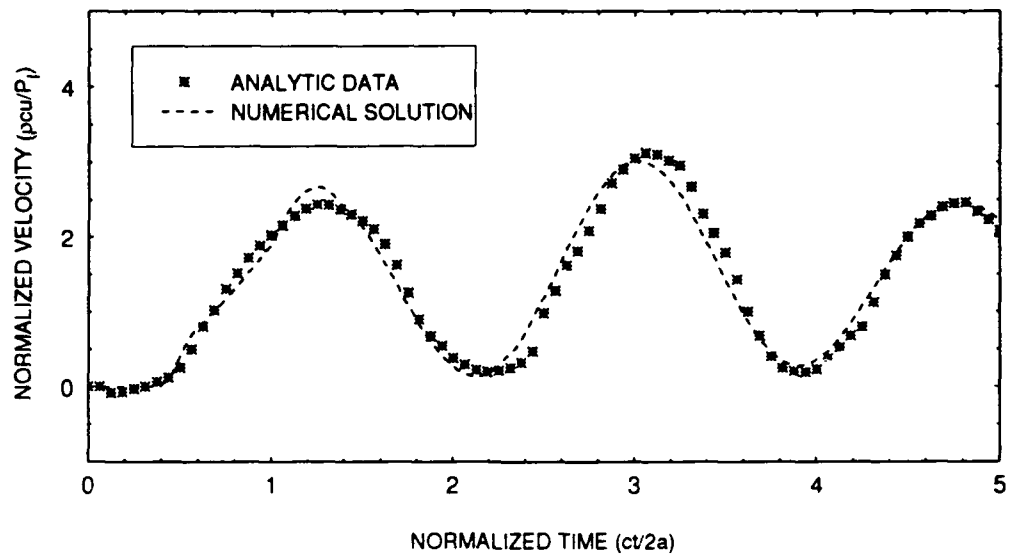
Young's Modulus	E=206.84 GPa
Poisson's ratio	$\nu=0.33$
Mass density	$\rho=7784.5$ kg/m

Water Properties

Sound speed	c=1461.2 m/s
Density	$\rho=999.6$ kg/m

The numerical results using the USA/DYNA3D combination for the above test case compare favorably with the exact results. The normalized results are shown in figure II.3. It can be seen that the numerical results lag the exact results, but the difference is negligible. Copies of the INGRID pre-processor input and output as well as the USA pre-processor inputs are provided in Appendix A.

$\theta = 0$



$\theta = \pi$

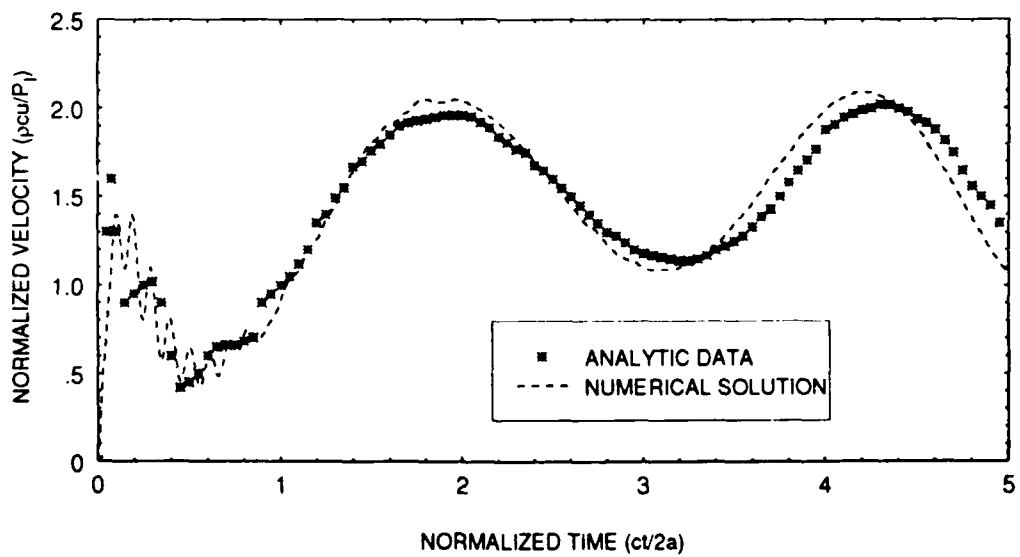


Figure II.3. Spherical model verification results.

## 2. DETAILED DESCRIPTION OF THE INFINITE CYLINDER MODEL

The infinite cylinder model was run using the same material and water properties shown above. Figure II.4 shows the geometry used for the analyses and, as shown in figure II.5, a single ring of elements was used to model the infinite cylinder by enforcing symmetry boundary conditions on each end of the model. In addition, since this is a two dimensional problem, the TWODIM option in USA was used to generate the added mass and DAA matrices. Further, the value of the  $\eta$  variable was set to 0.0.  $\eta$  is the factor that accounts for curvature. This resulted in a DAA1 solution for comparison to a known analytic DAA1 solution. The first model attempted had a longitudinal length of 0.1 inches. However, it was discovered that this resulted in a oscillatory solution as shown in the first graph in Figure II.6. A similar oscillation occurred on the reverse side of the cylinder as shown in Figure II.7. After a check of the input data to ensure that the problem was not caused by numerical instability, it was hypothesized that the oscillation was caused by residual three dimensional effects caused by the finite width of the model. As a test of this hypothesis, two additional models were run with widths of 0.01 and 0.001 inches. As shown in Figure II.6 and II.7, reduction in width progressively reduced the oscillations on both the front and back of the cylinder. At 0.001 inches, oscillations are absent.

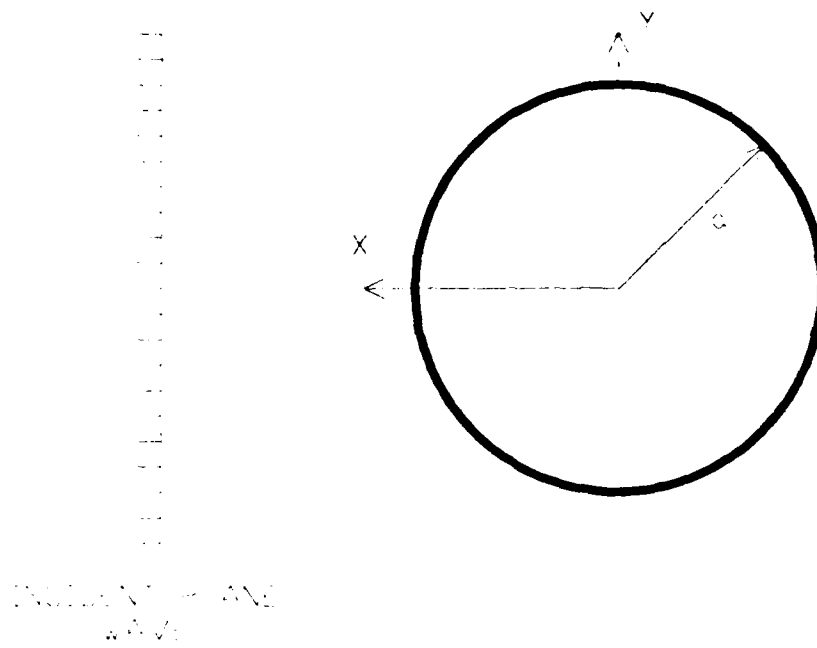


Figure II.4. Infinite cylinder problem geometry.

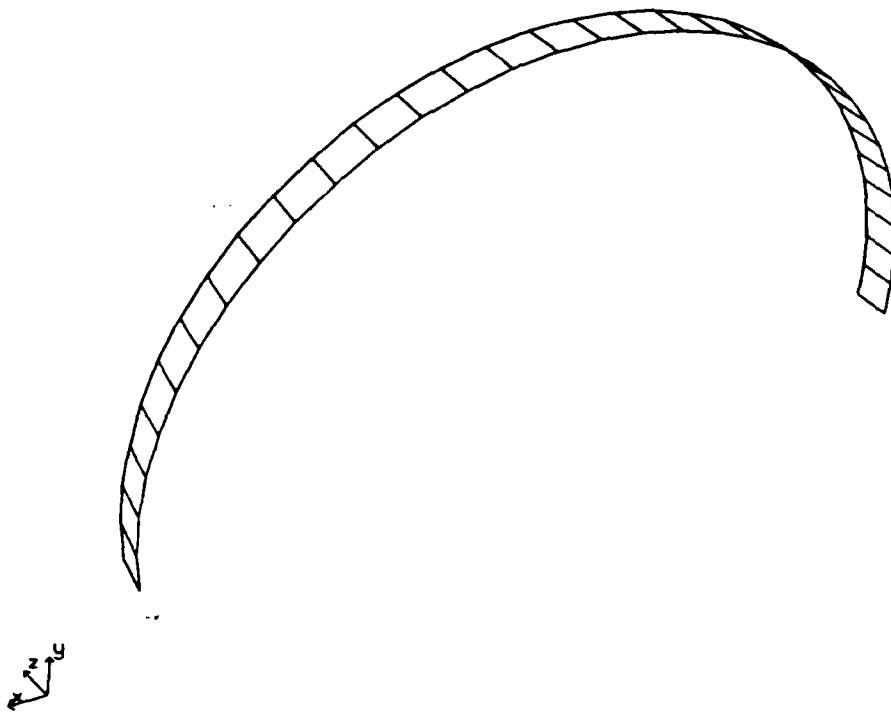
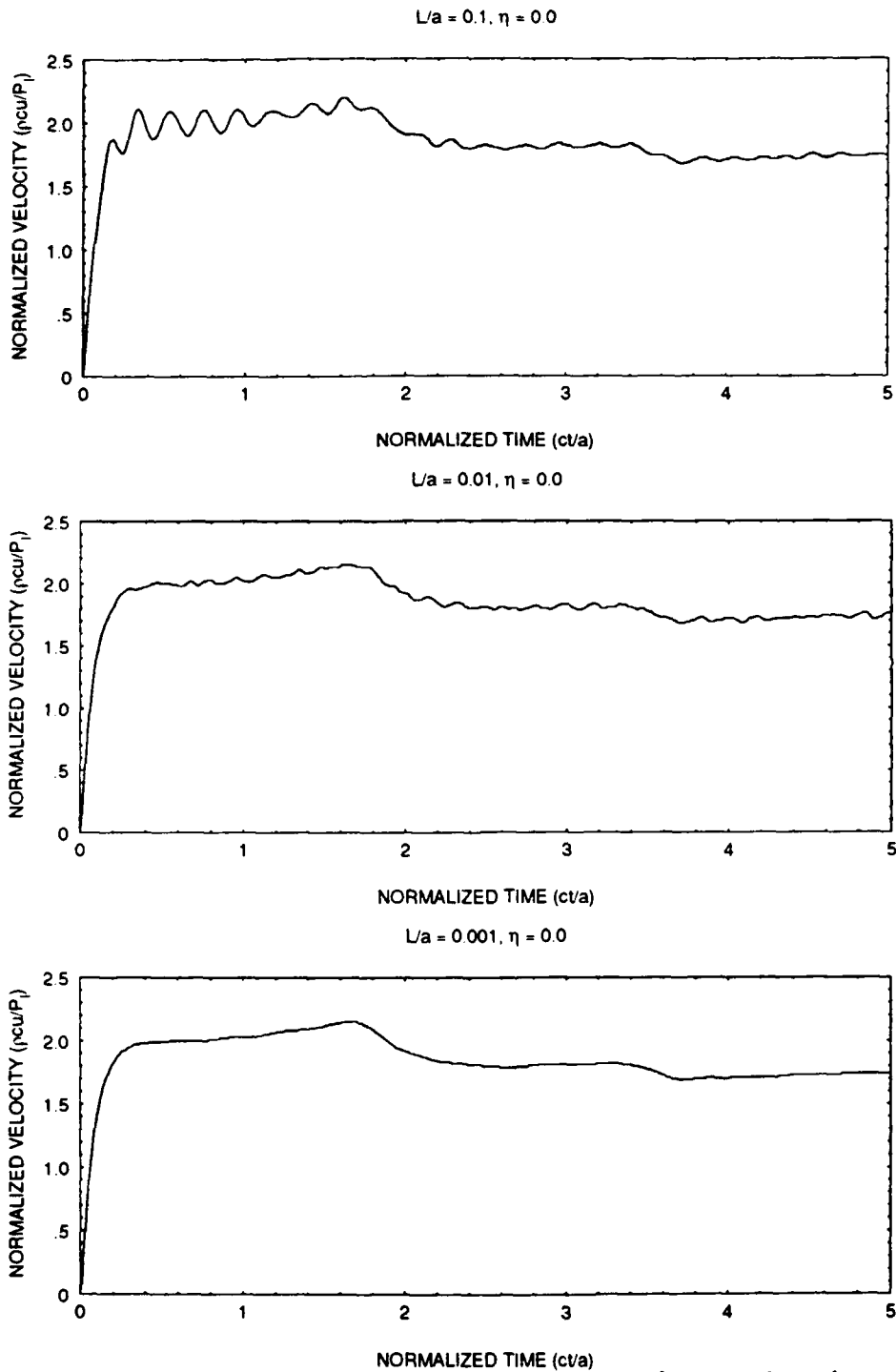
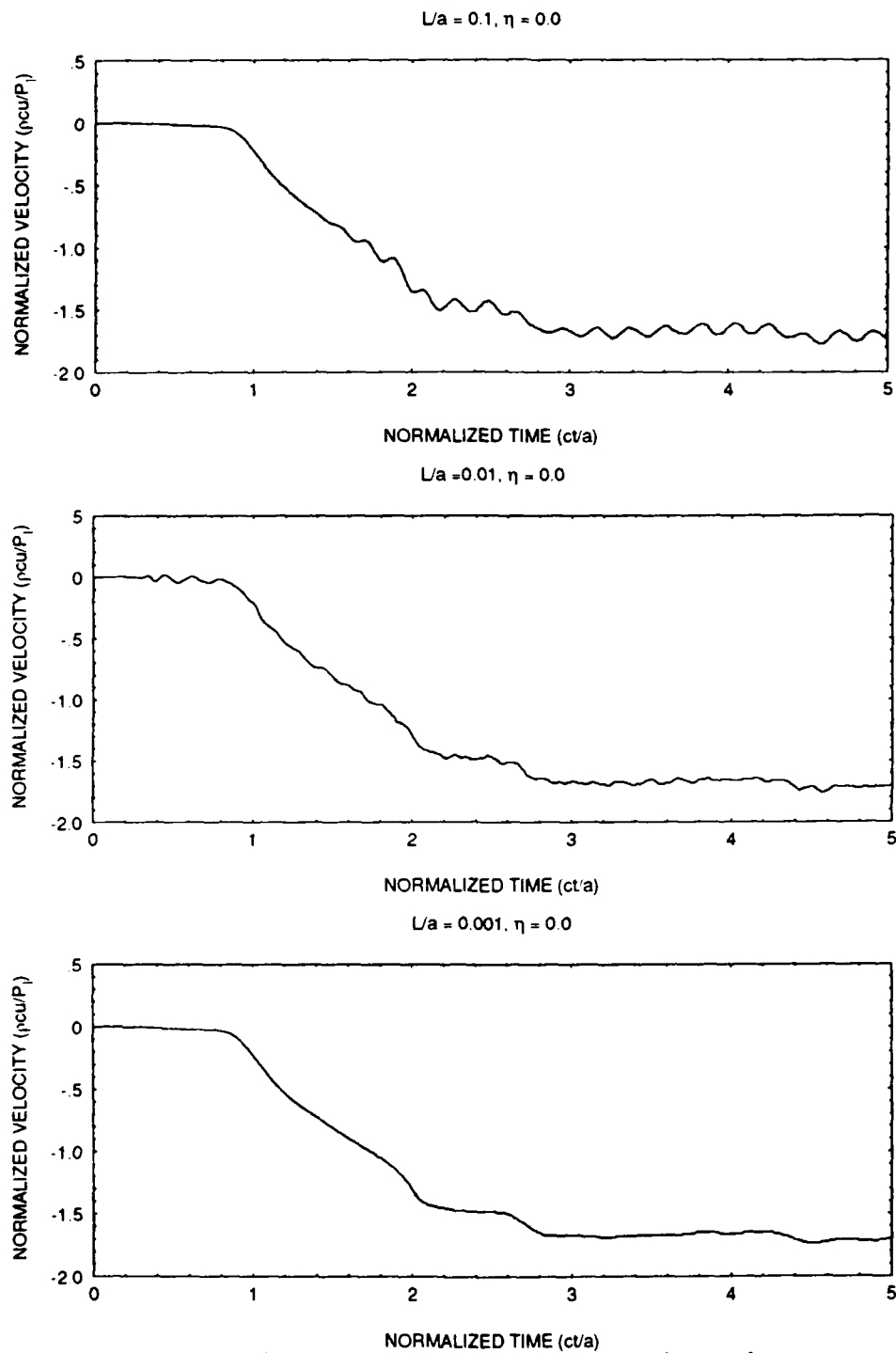


Figure II.5. Infinite cylinder validation model.





**Figure II.6. Infinite cylinder oscillation reduction (near element).**



**Figure II.7. Infinite cylinder model oscillation removal (far element).**

The final results from the 0.001 inch model with a  $\eta$  variable value of 0.0 were compared to the analytical exact and analytical DAA1 solutions with favorable results as shown in figure II.8. It can be seen that the results on both the front and back sides of the cylinder lie very close to the analytic DAA1 solution.

A further investigation was conducted to determine what value of the  $\eta$  variable would result in the numerical solution closest to the analytic modal solution. Values of 0.0, 0.25, 0.5, 0.75 and 1.0 were tested. The results are shown in figures II.8 through II.12. Review of the results show that the value of the  $\eta$  variable that provides the results nearest the analytical modal solution varies depending on time and position on the cylinder.

For the front of the cylinder, a DAA2 variable value of 0.0 gives results fairly close to the analytical solution for all times. However, values of 0.25 and 0.5, although they do not match closely at early times, match more closely at late times.

On the reverse side, a value of 0.0 provides a result very near the analytical DAA1 solution, but varies substantially from the analytical modal solution. Values of 0.5 and 0.75 provide results near the analytical modal solution with 0.75 being the best result.

Assuming that interest lies in late time results over

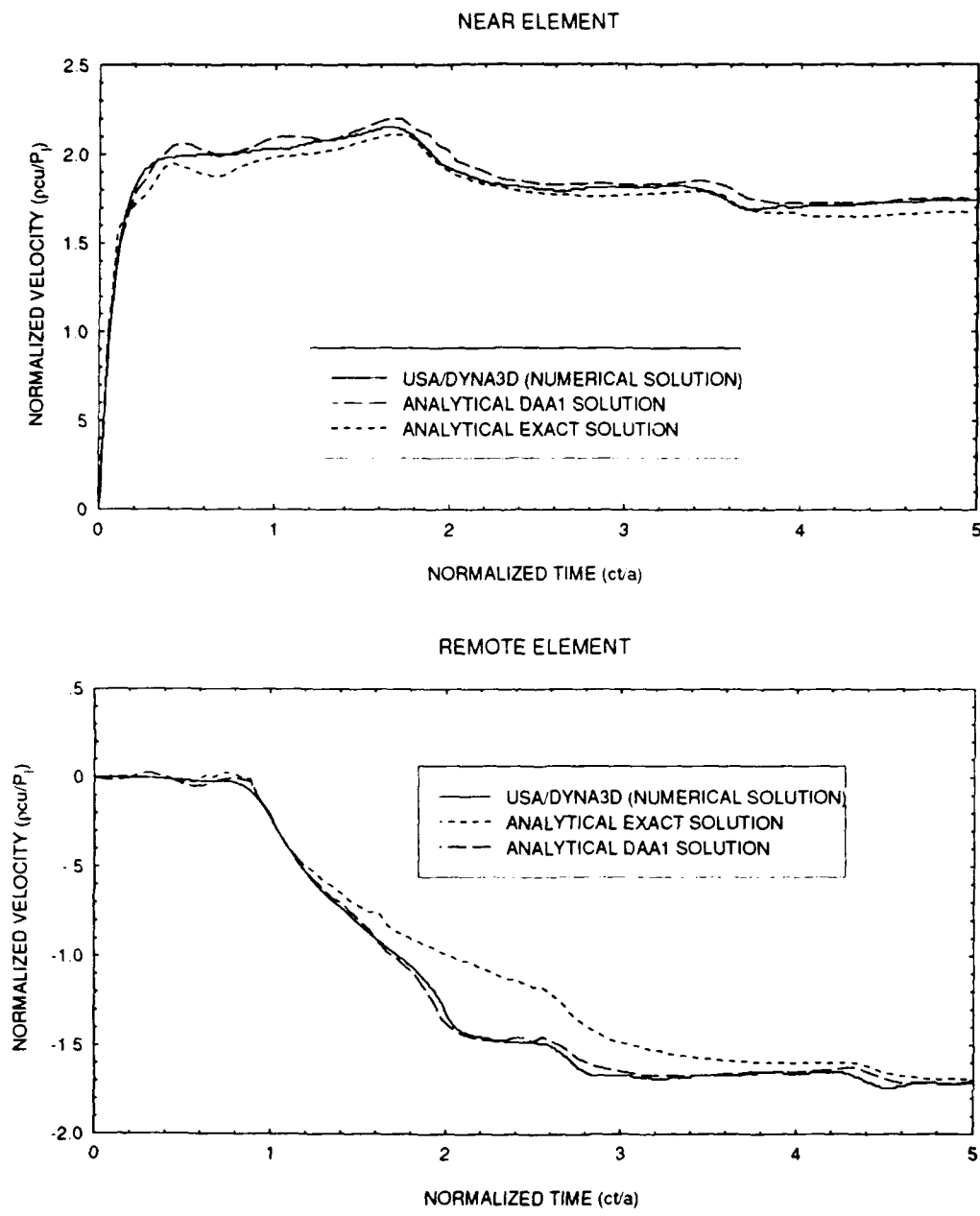


Figure II.8. Infinite cylinder results with  $\eta=0.0$ .

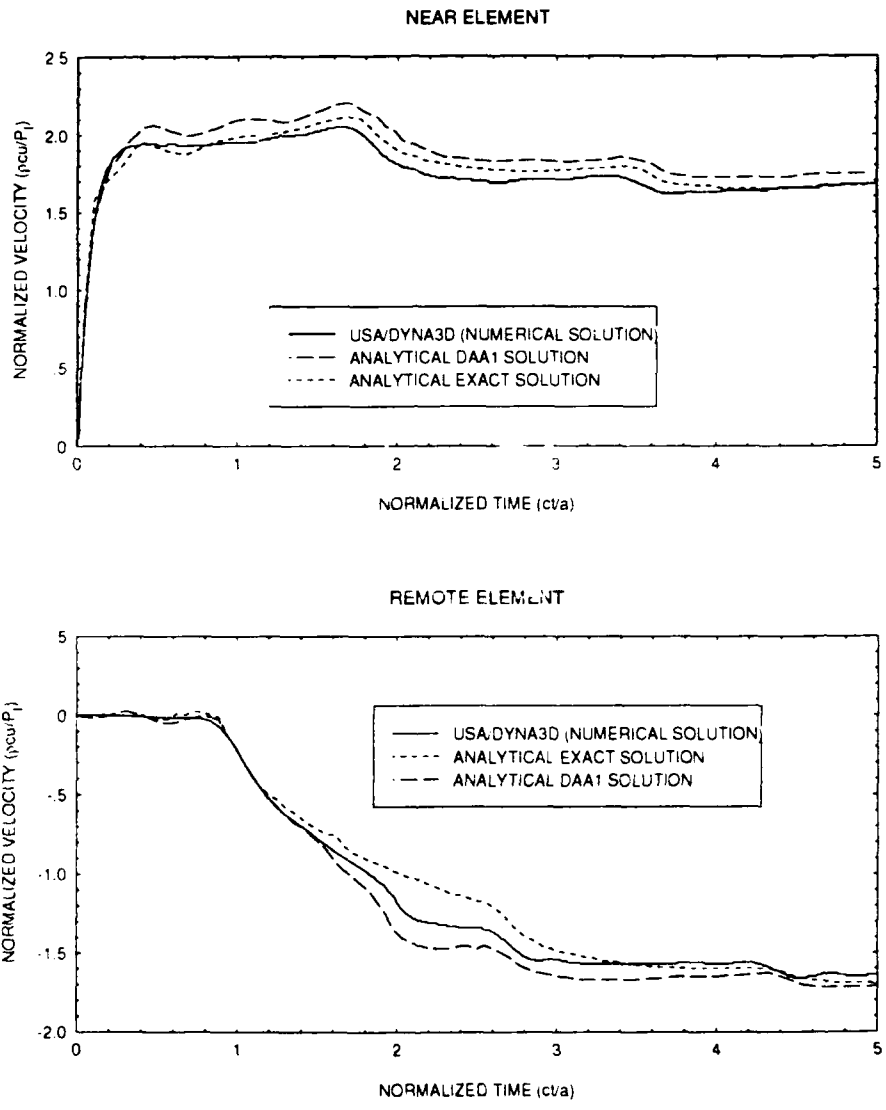
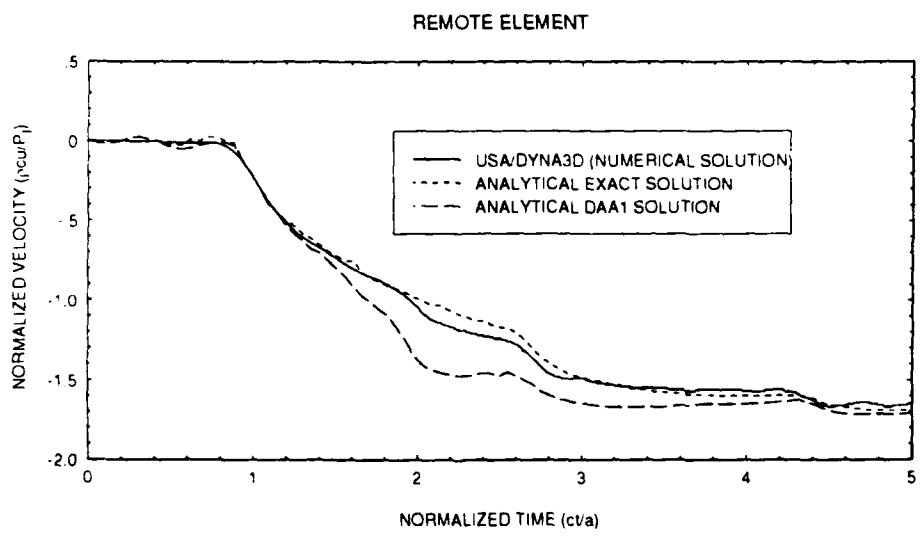
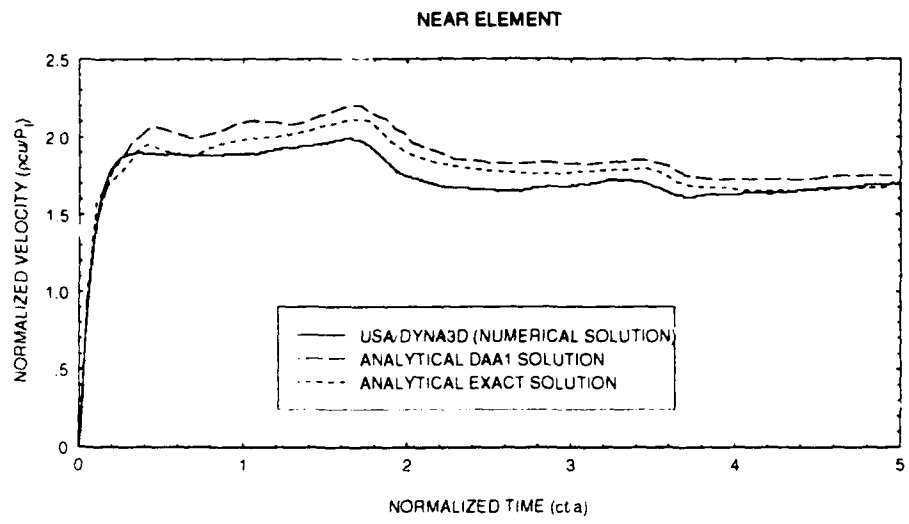


Figure II.9. Infinite cylinder results with  $\eta=0.25$ .



**Figure II.10. Infinite cylinder results with  $\eta=0.50$ .**

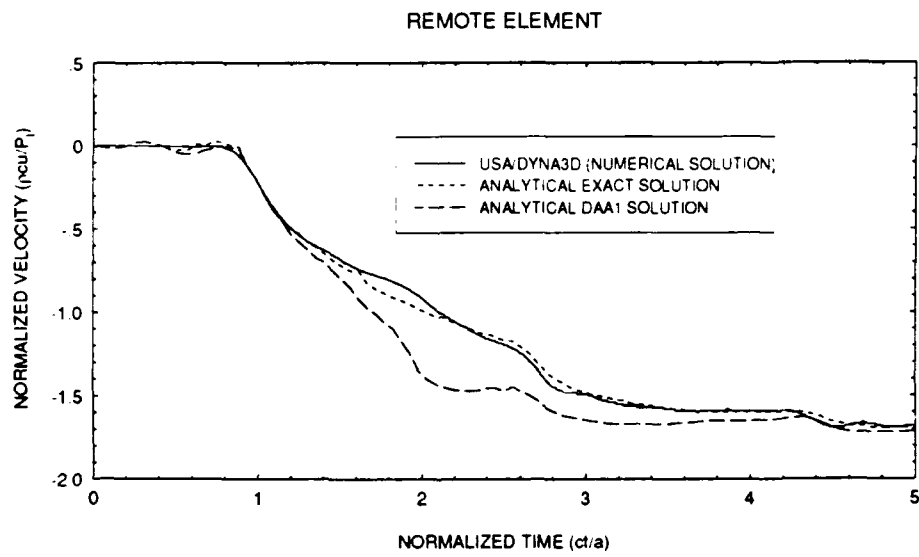
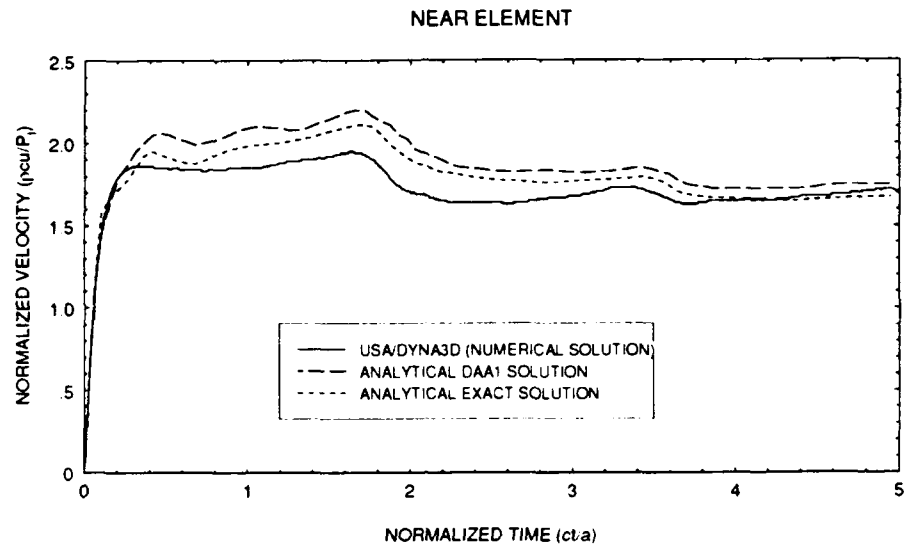


Figure II.11. Infinite cylinder results with  $\eta=0.75$ .

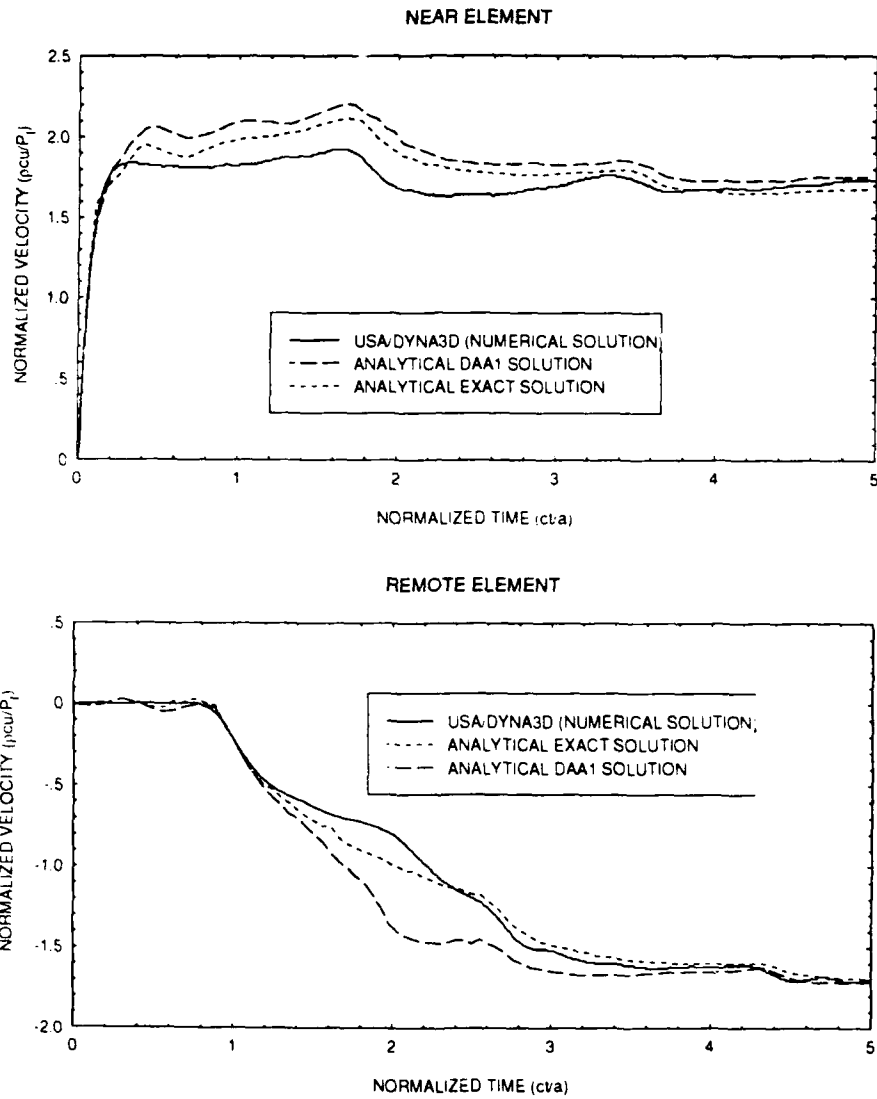


Figure II.12. Infinite cylinder results with  $\eta=1.0$ .



the entire cylinder, the results show that the best overall value of  $\eta$  for an infinite cylinder lies between 0.5 and 0.75. More compact bodies will have best results with higher  $\eta$  values.

The INGRID pre-processor input and output for the infinite cylinder verification, as well as the USA code pre-processor input are provided in Appendix B.

### III. EXPERIMENTAL METHOD AND DESCRIPTION OF MODELS

#### A. DESCRIPTION OF PHYSICAL MODEL USED FOR THE FAR FIELD STUDY

The physical model was an unstiffened right circular cylinder with the following characteristics.

Dimensions:

Length	42 inches (1.067 m)
Diameter	12 inches (0.305 m)
Weight	60.5 pounds (27.5 Kg)

Materials:

Shell	1/4 inch thick 6061-T6 Aluminum (0.64 cm)
End Plates	1 inch thick 6061-T6 Aluminum (2.54 cm)

The cylinders used for this test were constructed from commercially available material. Fabrication was performed at the Naval Postgraduate School. The end plates were welded to the shell using a Tungsten Inert Gas (TIG) process.

The 6061-T6 aluminum was selected on the basis of its high strength and strain rate insensitivity. The material properties of the aluminum used for the shell were verified using the MTS machine at the Naval Postgraduate School. Results of tensile testing determined that the material

properties were near nominal with a Young's modulus of 10800 ksi (75.6 GPa) and yield strength of 43 ksi (300 MPa).

#### **B. UNDERWATER EXPLOSION TEST**

The underwater explosion test was performed at the Dynamic Testing Incorporated (DTI) facilities in Rustburg, Virginia. The facility is in a quarry and the depth of the water is approximately 130 feet (39.6 m) at the location of the test. As a result, bottom reflection was not a factor in the test.

The charge used for the test was 60 pounds (27.3 Kg) of HBX-1. The peak pressure generated by the charge was 2360 psig (16.3 MPa) which was substantially lower than the calculated peak pressure of 2680 psig (18.5 MPa) for the 60 pound (27.3 Kg) charge at a 25 foot (7.62 m) standoff distance. The test charge was activated by a radio control device.

The test depth for both the charge and the cylinder was 12 feet (3.66 m). This depth allowed the bubble generated by the explosion to vent at the surface prior to encountering the cylinder and eliminated the possibility of a bubble pulse. In addition, the 12 foot (3.66 m) depth provided a clear pressure cutoff.

The cylinder was held in place with a crane rig and the charge was suspended from a float. Distance and alignment of the charge to the cylinder was established and maintained using a tensioned span wire from the charge float to the

cylinder support rig. Post-shot calculations found the arrival time of the shock wave to be consistent with a distance of 25 feet (3.66 m) and sound of speed in water of 4800 ft/sec (1463 m/s). Test profile and arrangement are provided as figures III.1 and III.2.

Strain measurement was performed using CEA-06-250UW-350 strain gages. These are general purpose strain gages with an optimum range of  $\pm 1500$  microstrain and are good for both static and dynamic test measurements. The strain gages were bonded to the cylinder using a M bond 200 by a instrumentation technician employed by DTI. All pre-shot calibration and connection were performed by DTI technicians.

The test called for 14 total strain gages (seven to measure hoop strains and seven to measure axial strains). Of the fourteen strain gages, three failed. The dynamic range of the test exceeded the optimum range of the strain gages by a significant factor. This is the most probable cause of the high strain gage failure rate. The instrumentation diagram for the test is provided as figure III.3. The strain gage located at B1 was placed nearest the charge during the test. Strain gage output was filtered at 2000 Hz. Locations noted on figure III.3 will be used for reference throughout the remainder of the report.

Slight damage to the cylinder was noted upon completion of the test. Post-shot investigations found all strain gages firmly attached to the cylinder at the locations specified in

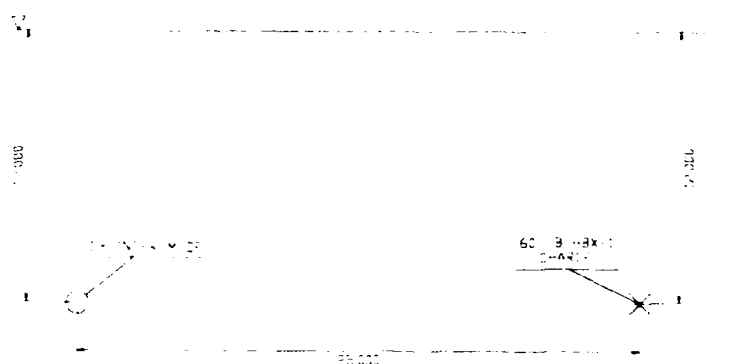


Figure III.1. Undex test profile.

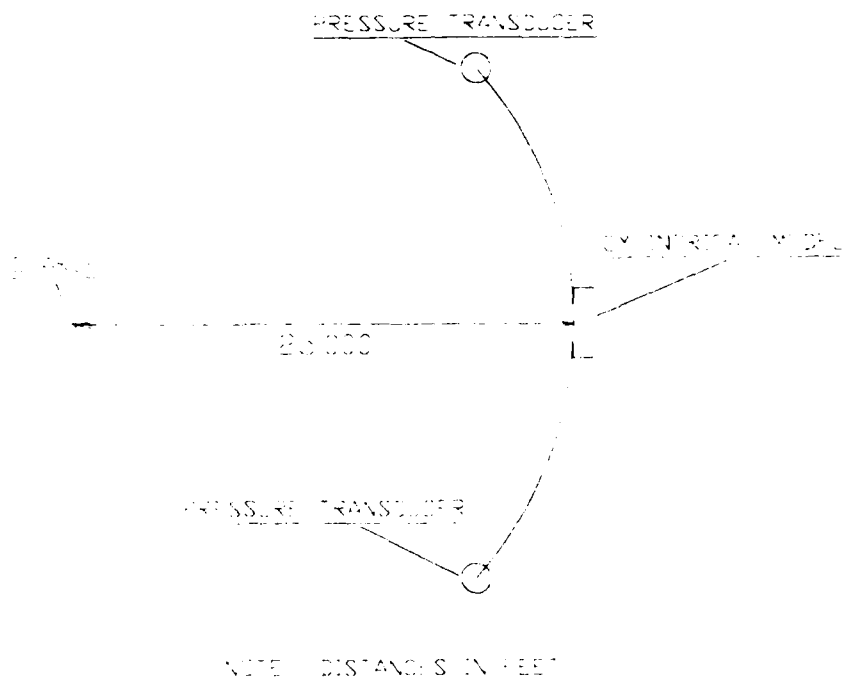


Figure III.2. Undex test general arrangement.

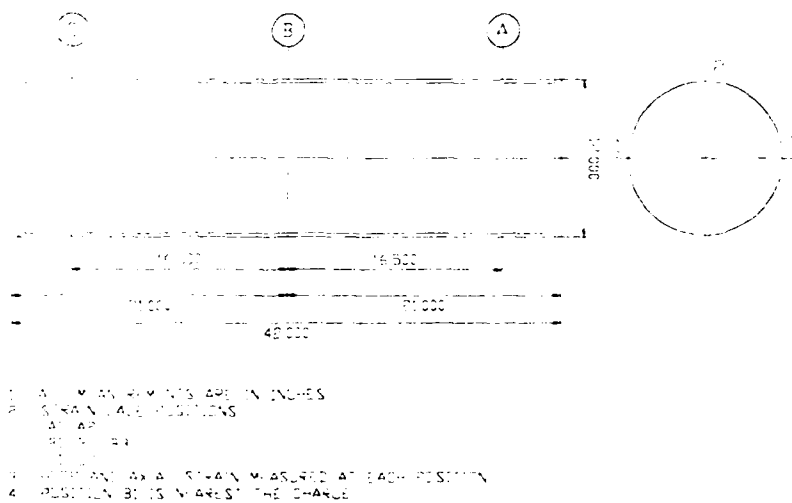
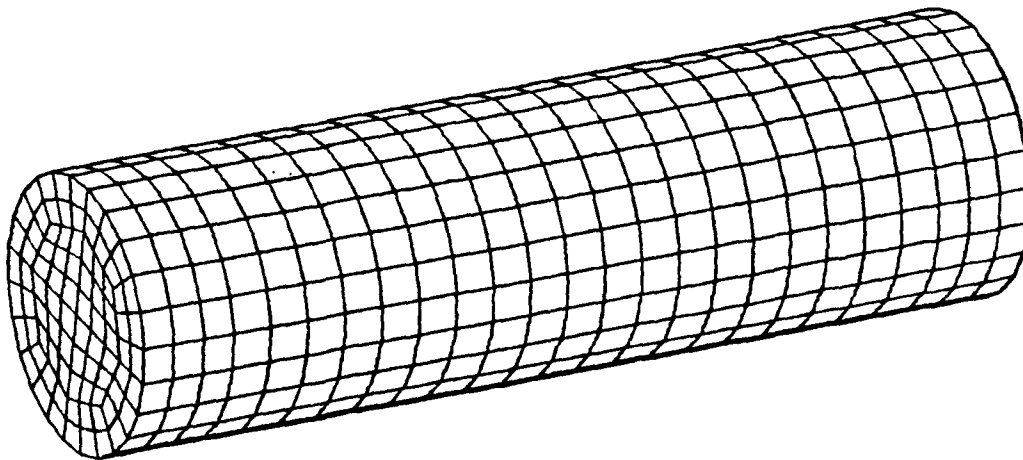


Figure III.3. Undex test instrumentation diagram.

the instrumentation diagram. However, some water intrusion was noted under the protective coating of several of the strain gages. This intrusion may also have played a part in the strain gage failures. The results of the test were forwarded to the Naval Postgraduate School. A copy of the report is enclosed as Appendix C.

### **C. NUMERICAL MODEL**

This study was performed using two primary mesh densities. The low density, full model mesh (figure III.4) was used for rotation, shell type and quadrature sensitivity analyses. The high density quarter model was used to perform direct comparison to experimental results and examine end effects.



**Figure III.4. Low density, full model**

The computational efficiency of the quarter model allowed a more refined mesh without a subsequent increase in



computational time or random access memory storage capability. A sample quarter model was run and results checked against a full model with the same mesh configuration to certify that the symmetry boundary conditions used to form the quarter model were valid. The refined mesh quarter model is shown in figure III.5.

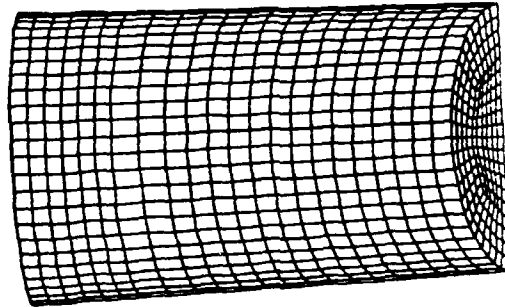


**Figure III.5. Refined mesh model.**

In addition to the two models noted above, several additional quarter models with varying mesh density were run to verify mesh size independence of the quarter model results. It was found that the most critical locations for the mesh sensitivity check were the locations with the highest strain. The areas with the highest strain were located near each end on the side of the cylinder located nearest the explosive charge. Figure III.6 shows the strain pattern on the surface

of cylinder side nearest the charge. The high strain locations are symmetrically located 16.5 inches (0.42 m) from the axial midpoint of the cylinder. The other region of significant plastic strain was located on the surface of the reverse side of the cylinder at the axial midpoint. Figure III.7 shows the effective plastic strain pattern for this location. Effective plastic strain is defined by the relation:

$$\bar{\epsilon}_p = \frac{\sqrt{2}}{3} [(\epsilon_{1p} - \epsilon_{2p})^2 + (\epsilon_{2p} - \epsilon_{3p})^2 + (\epsilon_{3p} - \epsilon_{1p})^2]^{\frac{1}{2}}$$

where  $\epsilon_{1p}$ ,  $\epsilon_{2p}$  and  $\epsilon_{3p}$  represent the principal plastic strain components [Ref. 10]. The near side high strain regions cover a much smaller area than the reverse side region. That is, much higher strain gradients occurred on the near side compared to other locations on the cylinder. This condition plays a significant roll in mesh design and integration time increment selection.

Figures III.8 through III.10 show the results of the mesh sensitivity test. It was found that strains in the axial direction were more sensitive to mesh density than hoop strain results. Figure III.8 shows the strain at the surface of the cylinder at the point nearest the charge (location B1). This

time = .59796E-02  
fringes of eff. plastic strain  
min= 0.000E+00 in element 768  
max= 6.431E-03 in element 442

fringe levels  
9.000E-04  
1.800E-03  
2.700E-03  
3.600E-03  
4.500E-03

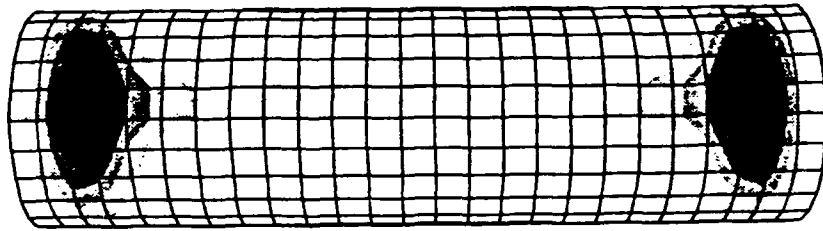


Figure III.6. Effective plastic strain pattern on cylinder side nearest the explosive charge.

time = .59796E-02  
fringes of eff. plastic strain  
min= 0.000E+00 in element 768  
max= 6.431E-03 in element 442

fringe levels  
9.000E-04  
1.800E-03  
2.700E-03  
3.600E-03  
4.500E-03

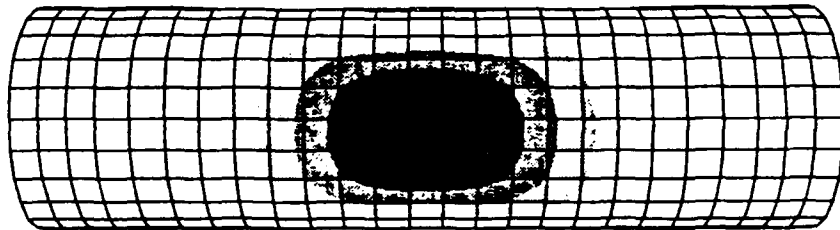
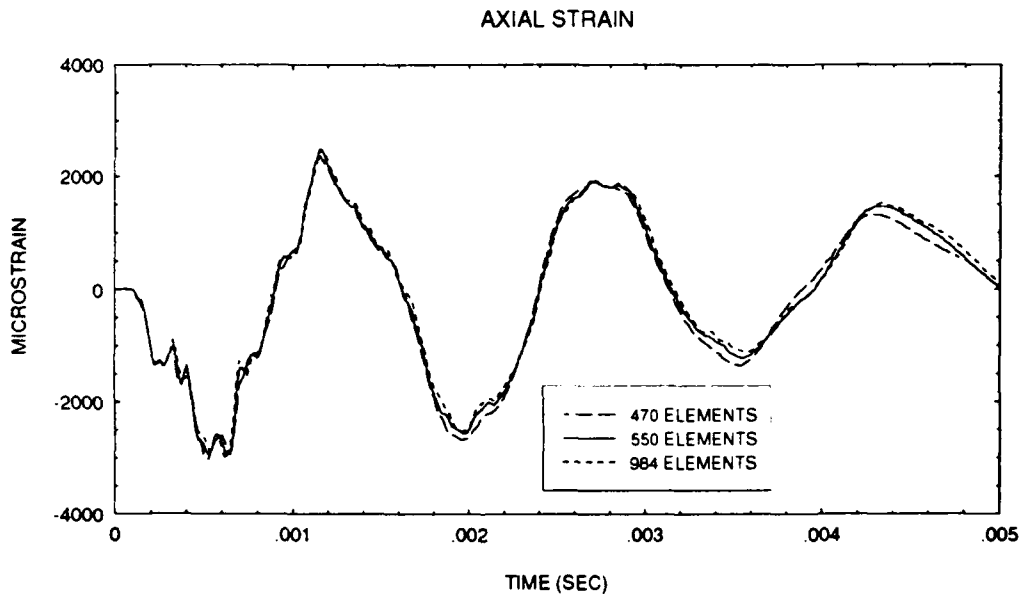
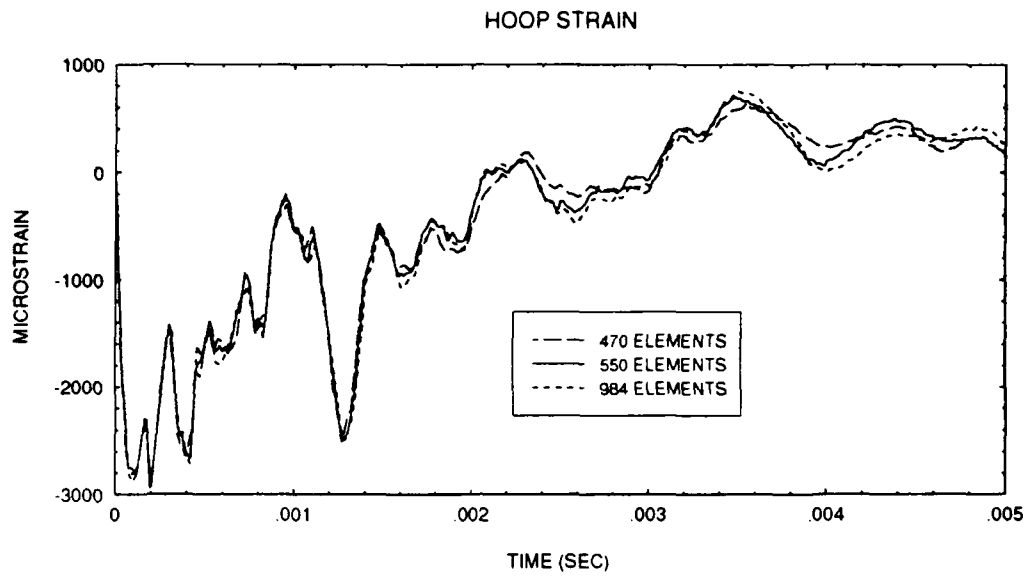


Figure III.7. Effective plastic strain pattern on cylinder side most remote from the charge.

location has no permanent plastic strain. It can be seen that there is no significant difference between the results for the three mesh densities checked. Figure III.10 shows strain results for the surface of the shell at the point most remote from the charge in the circumferential direction at the axial midplane (location B3). This location had the second highest strain of the positions checked. Although there is a slight difference between the three different mesh results, it is apparent that these differences are insignificant when compared to the overall plastic strain. Figure III.9 shows the strain results for the locations that experienced the highest plastic strains (locations A1 and C1). The difference in the hoop direction is noticeable but small enough to be neglected. However, the results in the axial direction are significant with a 30 percent variance between the average plastic strains for the high density mesh and medium density mesh. Additional refinement was not possible due to random access memory limitations on the system used to perform the analysis. On the basis of the above results it was determined that the medium mesh model was adequate for comparison of numerical to experimental results for all hoop strains and all axial strains except at the locations near the end on the side nearest the charge. The high density mesh was used for the axial strain comparison at the remaining locations. Care was taken to ensure that the mesh was as uniform as possible for both the full and the quarter mesh models to avoid problems



**Figure III.8. Mesh sensitivity comparison for surface of shell located nearest the explosive charge (location B1).**

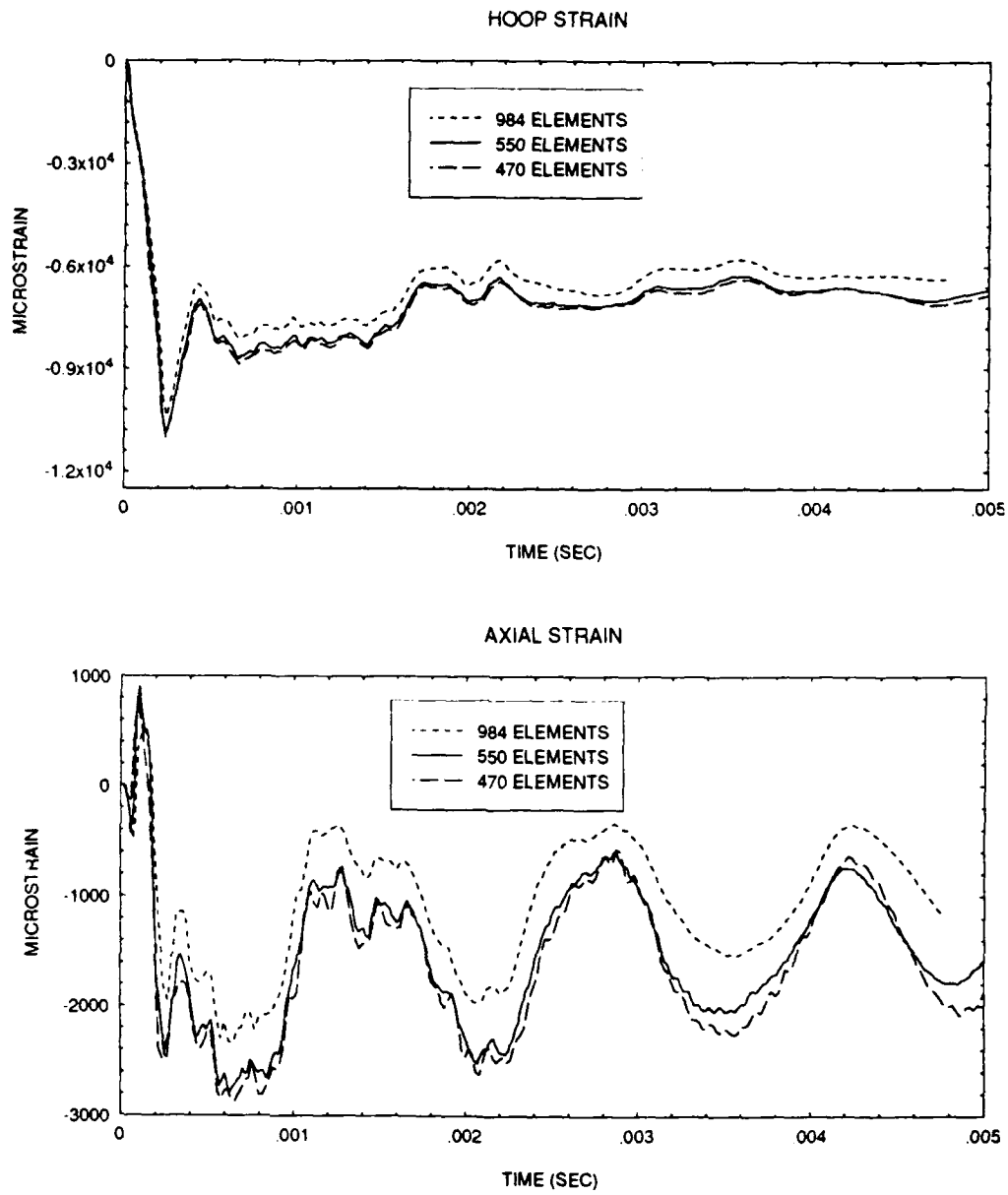
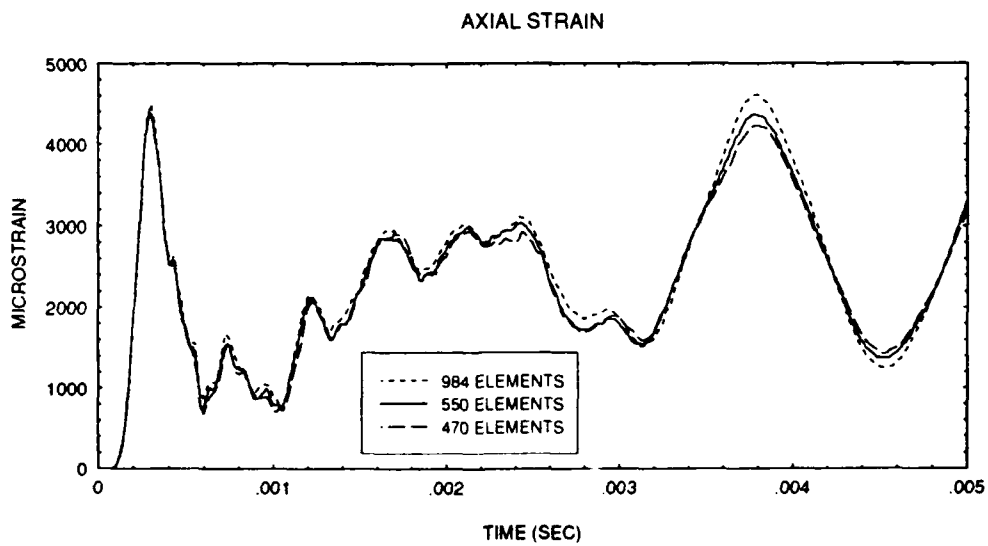
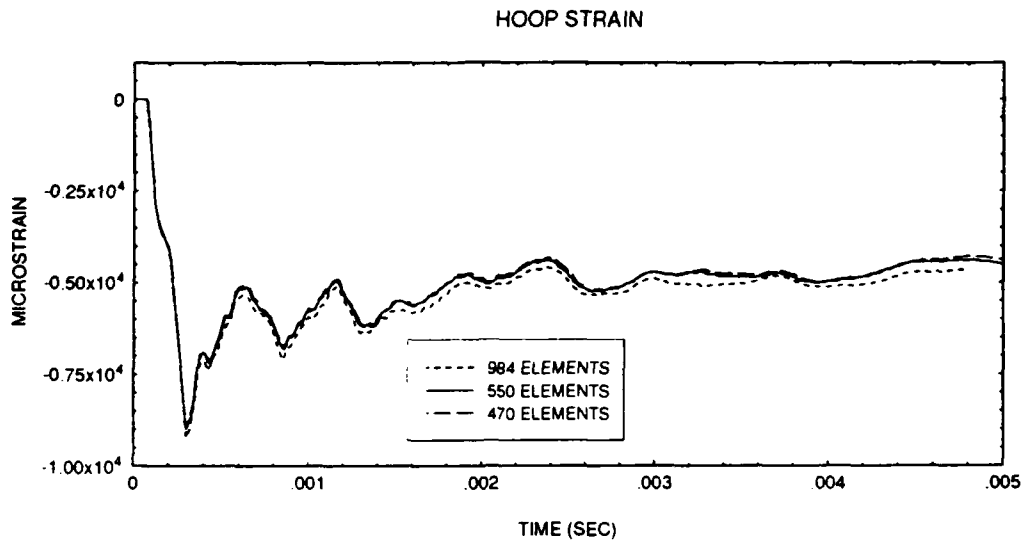


Figure III.9. Mesh sensitivity comparison for position with largest plastic strain (locations A1 and C1).



**Figure III.10. Mesh sensitivity comparison for point on cylinder most circumferentially remote from the charge (location B3).**

with mesh reflection as noted earlier in this report.

Thin shell elements were used for both the shell and end plates. Since relatively small out of plane displacements were encountered in the test model, it was determined that the four node Belytschko/Lin/Tsay shell formulation [Ref 11], which is the default formulation for VEC/DYNA3D, was adequate for the analysis. A Hughes/Liu [Ref. 12] shell model and a eight node brick shell model were also run for comparison.

The Belytschko/Lin/Tsay shell was selected over the Hughes/Liu shell and 8 node brick shell formulation because of its higher relative computational efficiency.

The aluminum was treated as a kinematic/isotropic elastic/plastic material with no strain rate sensitivity. Research has shown that shock velocities much higher than the velocities encountered in the test are required to induce strain rate sensitivity in 6061-T6 aluminum.

The pressure input for the model was obtained from the free field pressure transducer time record of the underwater explosion test. The 17000 point trace was numerically condensed to 100 points and entered into the TIMINT pre-processor of USA using the VARLIN (variable linear) option. Figure III.11 shows the pressure profile used for the analysis. Free surface effects were neglected and the speed of sound in water used for the test was 4800 ft/sec (1463 m/s) since the test was performed in fresh water at approximately 40 degrees Fahrenheit (4.5 degrees centigrade).



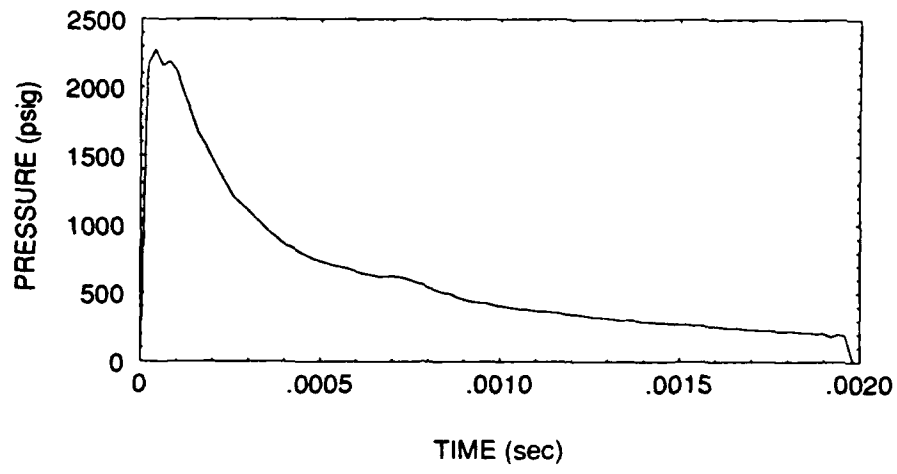


Figure III.11. Undex pressure profile.

#### IV. FAR FIELD STUDY RESULTS

##### A. EXPERIMENTAL TO NUMERICAL COMPARISON

As described earlier in the report, an underwater explosion test was conducted at the Dynamic Testing, Incorporated facility in Rustburg, Virginia. The test included a side-on attack of a cylinder with a stand off distance of 25 feet (7.62 m) using a 60 pound (27.3 Kg) HBX-1 charge. Fourteen strain gages were attached to the cylinder, of which eleven provided useable data. Four statements can be made about the results. First, the numerical results compared well with the experimental results qualitatively. That is, the numerical response had the same general shape as the experimental results and it predicted compression and tension correctly. There was one exception to the above statement at position B3 (Figure IV.9). The numerical model indicated a tensile axial strain at position B3 while the experimental data indicated a compressive strain. Physically, it can be observed that the shock wave is spherical and initially strikes the cylinder center. This places the cylinder in bending. Therefore, tensile strain is expected in the axial direction on the reverse side of the cylinder. It is believed that the poles on the axial strain gage at position B3 were reversed resulting in an error in sign of the data returned by

the strain gage. As a result, the negative of the experimental strain is plotted versus the numerical results in Figure IV.9 with satisfactory results.

Second, there were variations in magnitude between the numerical results and the experimental data. Further, magnitudes matched the experimental results more closely at the position nearest the charge and error increased as distance from the point nearest the charge increased in both the axial and circumferential directions. In addition, numerical and experimental results match more closely in areas with lower values of total strain. Finally, axial strains were affected more than hoop strains. Charge size factors were eliminated as a possible cause of the magnitude differential since the measured pressure profile was used to perform the post underwater explosion test numerical calculations. In addition, the possibility of the charge being located closer to the shell than the specified standoff distance was eliminated by comparing the actual shock wave travel time measured from the strain gage traces to the expected shock wave travel time calculated for the speed of sound in water for fresh water at 40 degrees Fahrenheit (4.4 degree centigrade). The results indicated less than two inches difference between the calculated and measured values for stand off distance.

Third, the frequency of oscillation of the numerical data was lower than the experimental data. The higher frequency

oscillation in the physical model compared to the numerical model indicates that the experimental model is "stiffer" than the numerical model. This is an unexpected result, since numerical finite element solutions are normally expected to be stiffer than the physical model. In addition, the numerical results for axial strain tended to "ring" at all locations. The "ringing" is not a significant factor for hoop strains. It should also be noted that the "ringing" is heaviest at the front and back of the cylinder at the center. The causes of the "ringing" and the high stiffness of the physical model have not been determined and are a topic of additional study.

Finally, there is an unexpected asymmetry in the experimental results. The axial strain gage at position C1 (figure IV.10) measured 50% lower than the axial strain gage at A1 (figure IV.1) and the hoop strain gage at position C2 (figure IV.11) measured nearly 50 percent higher than the hoop strain gage at position A2 (figure IV.2). Failure of strain gages at positions A1, C1, and C2 prevented additional comparisons. The asymmetric results can result from two factors. The shell may have been rotated from the expected orientation by underwater currents or by forces placed on the cylinder and rigging by the instrumentation cables or there could have been a failure in the bonding between the strain gage and the cylinder surface on one or more strain gages.

Figures IV.1 through IV.11 provide the results of the numerical to experimental data comparison.

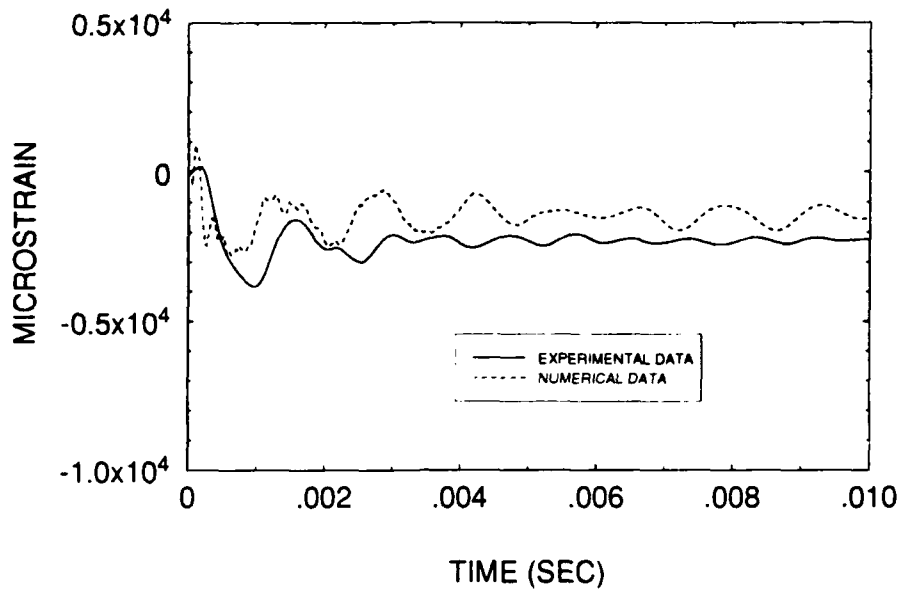


Figure IV.1. Experimental/numerical comparison for position A1 axial strain.

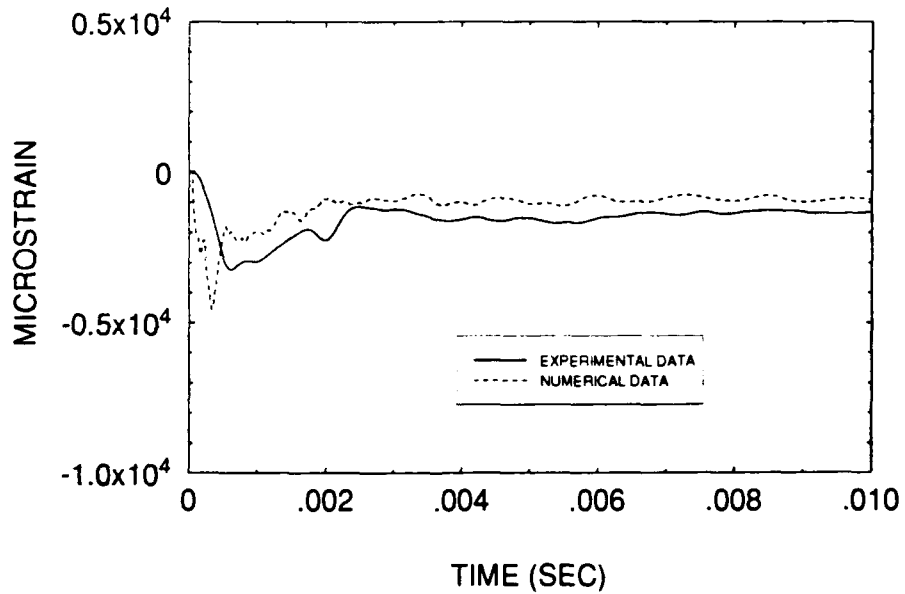
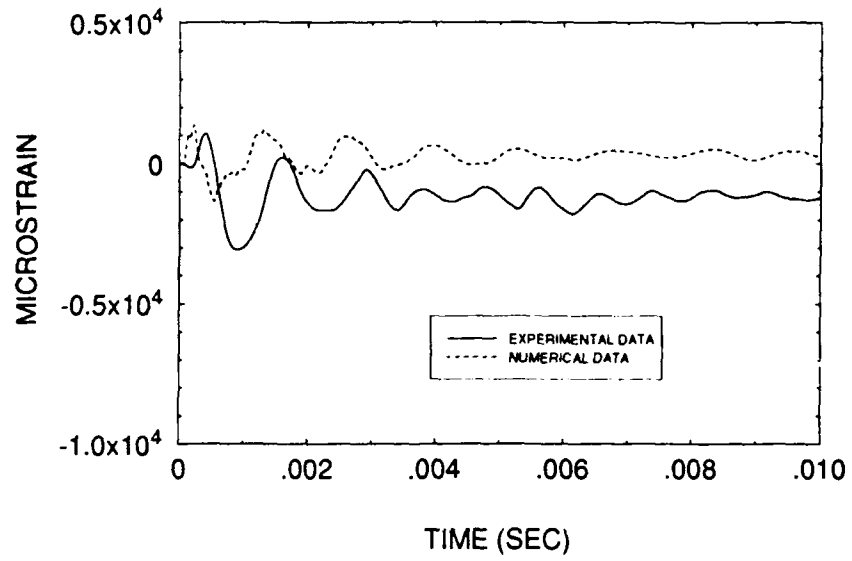
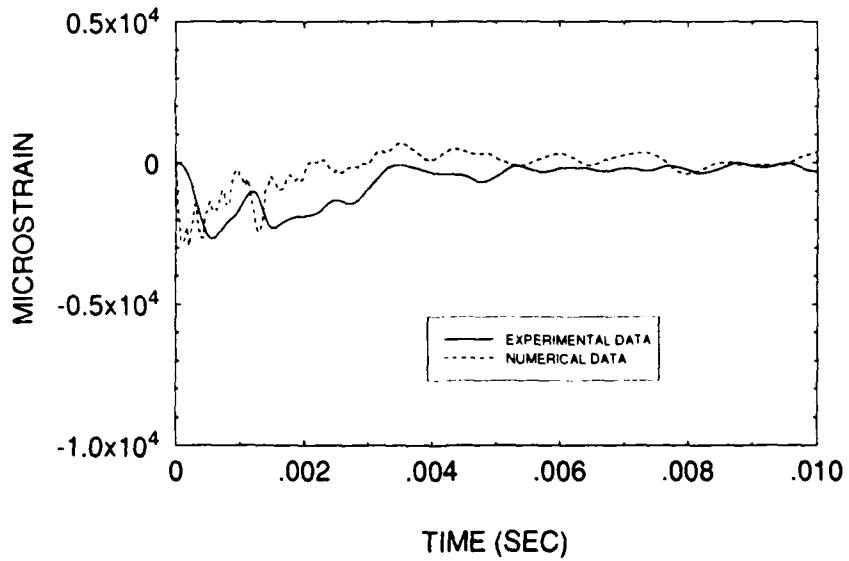


Figure IV.2. Experimental/numerical comparison for position A2 hoop strain.



**Figure IV.3. Experimental/numerical comparison for position A2 axial strain.**



**Figure IV.4. Experimental/numerical comparison for position B1 hoop strain.**

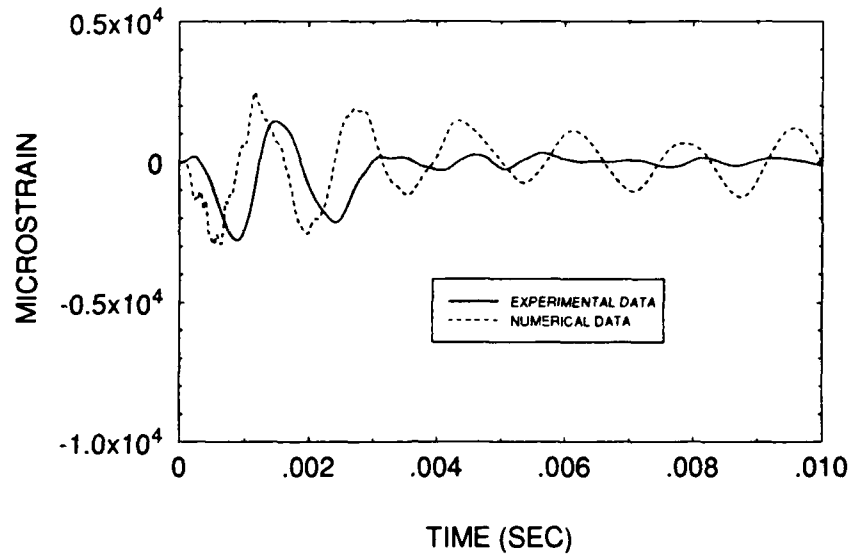


**Figure IV.5. Experimental/numerical comparison for position B1 axial strain.**

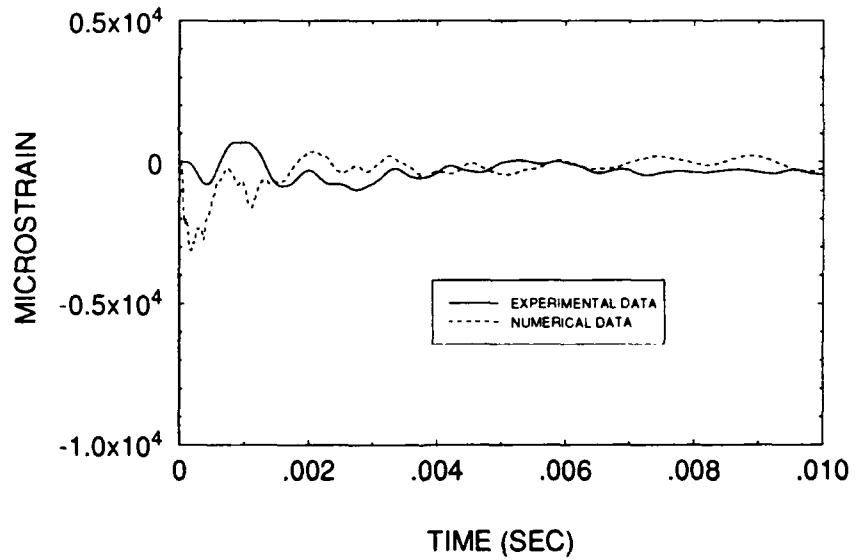


**Figure IV.6. Experimental/numerical comparison for position B2 hoop strain.**

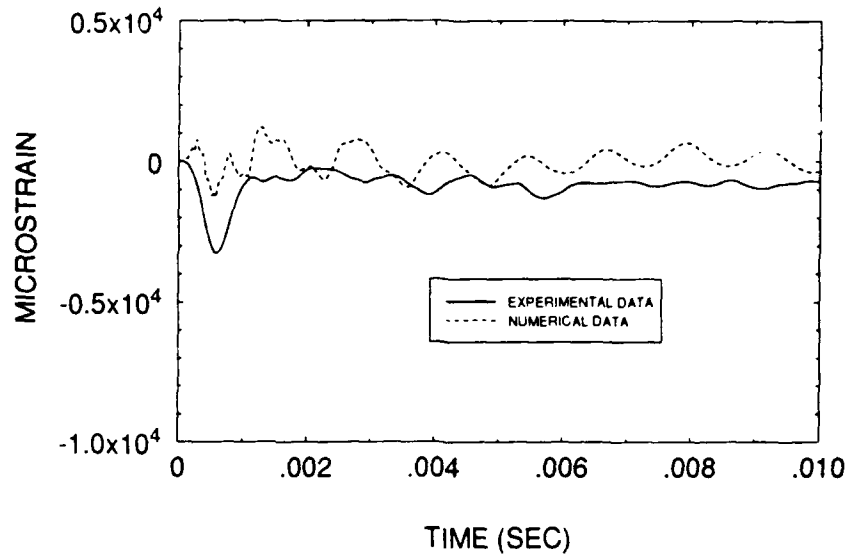


Figure IV.7. Experimental/numerical comparison for position B2 axial strain.

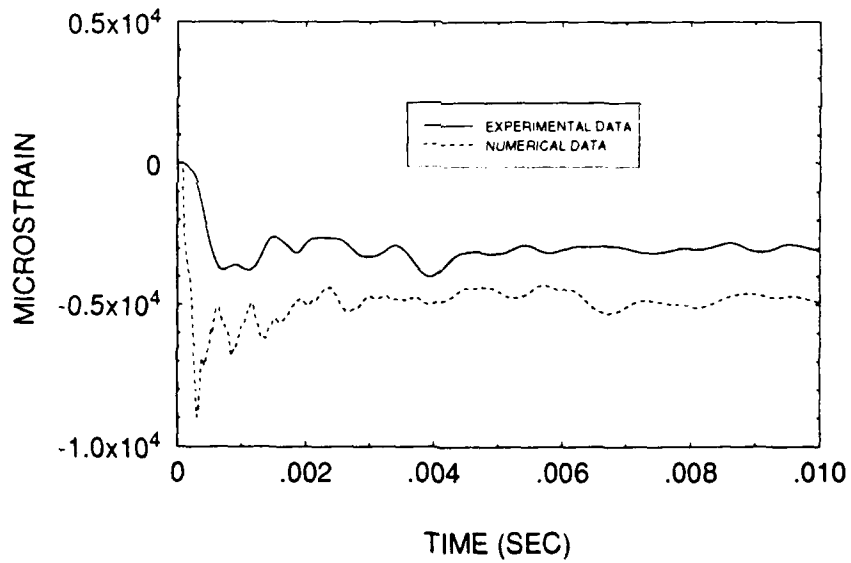
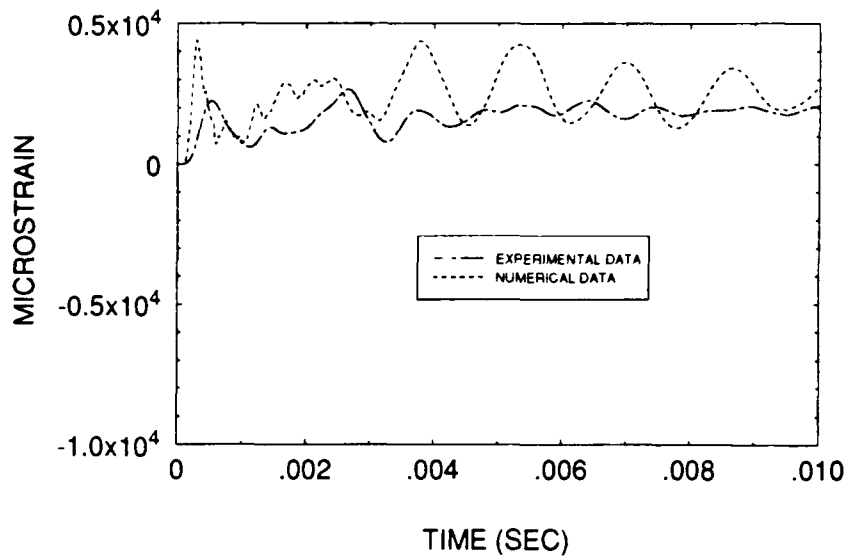
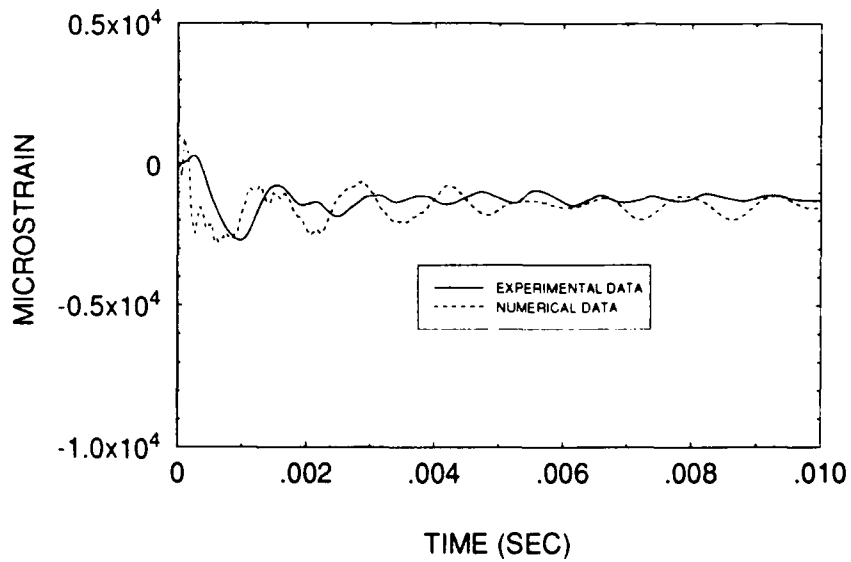


Figure IV.8. Experimental/numerical comparison for position B3 hoop strain.





**Figure IV.9. Experimental/numerical comparison for position B3 axial strain.**



**Figure IV.10. Experimental/numerical comparison for position C1 axial strain.**

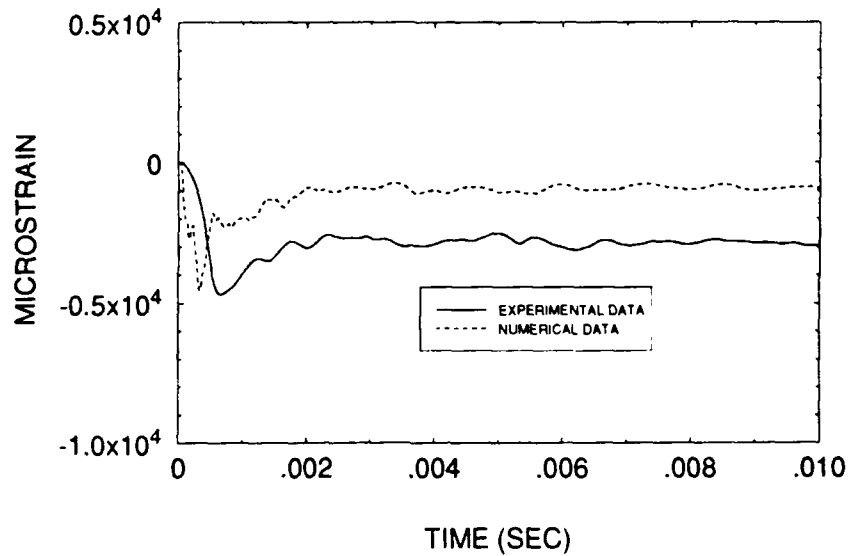


**Figure IV.11. Experimental/numerical comparison for position C2 hoop strain.**

#### **B. SENSITIVITY ANALYSES**

A series of sensitivity analyses were performed in an effort to explain the differences between the numerical and experimental results noted in the previous section. In addition, these analyses provided additional insight into the relative importance of various factors in the performance of underwater explosion tests and the associated calculations. Seven sensitivity analyses were performed. The first was the mesh sensitivity test. The results of this analysis have already been discussed. The other six analyses were, end effect, shell element formulation, integration time increment length, quadrature, rotational position and  $\eta$  value

sensitivity checks. The results of these analyses are provided in the following subsections.

#### **1. END EFFECT SENSITIVITY ANALYSIS**

As previously noted, the most severe deformation occurred at locations near the end of the cylinder (positions A1 and C1). Two processes cause this phenomena. First, the relatively large mass of the end plates apply large inertial forces to the cylinder shell near the end plates. Second, the one inch thick end plates are very stiff and their lack of flexibility causes the weaker material of the shell near the end plates to deform in response to applied forces. A examination of the numerical and experimental data reveals that these effects are concentrated near the end plates and result in large strain gradients. This means that elements on either side of a selected element near the end of the cylinder can have significantly different strain values. Accurate placement of strain gages within this region and careful mesh design along with adequately short time integration increments are critical in obtaining satisfactory results in a numerical to experimental data comparison. In addition, as stated earlier, the end plates are attached to the shell using a Tungsten Inert Gas process. This welding process results in high temperatures near the end of the cylinder. Since the aluminum for this model is at a peak hardened condition, this process could result in a change of the material properties

near the end of the cylinder that can only be restored by performing the age hardening process again after the welding is complete. These factors can result in an uncertainty in the expected strain compared to what might occur under ideal circumstances.

The mesh sensitivity results clearly display the importance of mesh design within this region. However, even with proper design, the large gradients can result in significant differences between the predicted and actual strains since the strain computed for the element is an average of the strain over the entire element vice a strain at a specific point. The best possible results would be obtained in these regions with large gradients if the mesh could be refined such that the size of the elements is the same size as the gage length of the strain gage. However, this would result in a prohibitively large number of elements and a subsequent increase in problem solution times. These problems can be overcome by placing strain gages in areas that are expected to have consistently increasing or decreasing strains and then ensuring that the mesh is designed so that the strain gage location is at the center of the element. If possible, large gradient regions should be avoided. If strain gages must be placed in a high gradient region, then the strain gages should be placed to one side or the other of the minimum or maximum strain location. Placement at the minimum or maximum point will result in an error since the average for

the element will lie above a minimum or below a maximum if the element is not the same size as the gage length of the strain gage.

In this study, the strain gages located at A1 and C1 were located at the point of highest compressive strain. Therefore, a study was performed to determine the relative importance of the noted location factors. Figures IV.12 through IV.16 show the results of this study. Strains of two additional elements nearer the end were compared to the measured strain and the actual strain gage location. Elements nearer the end plate were selected since the welding effects

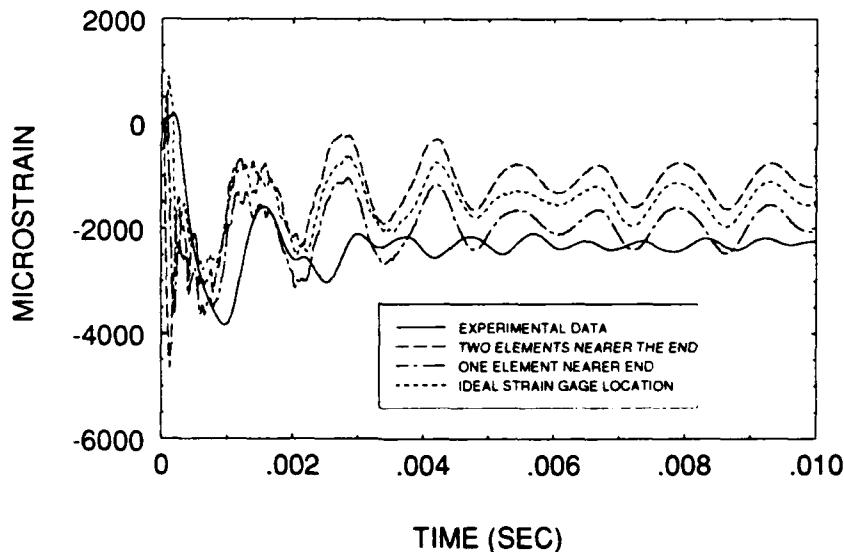
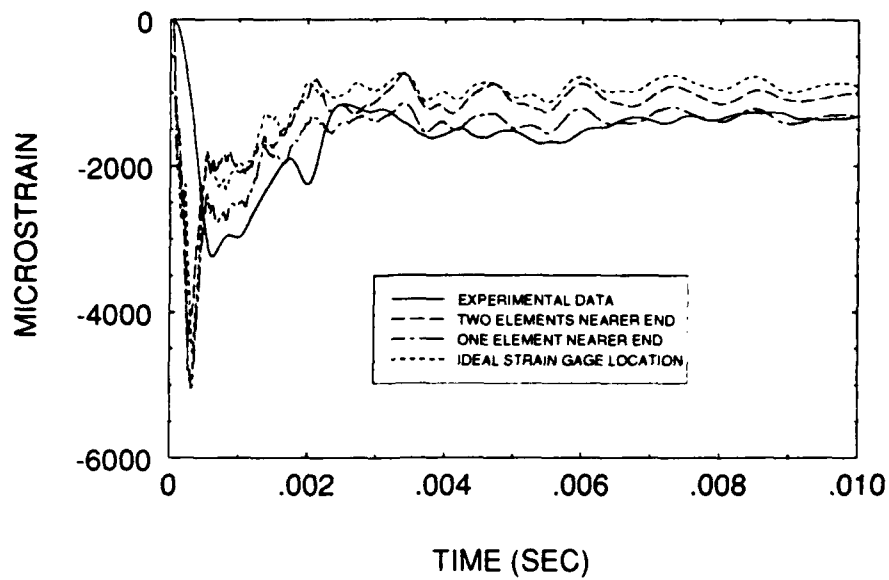
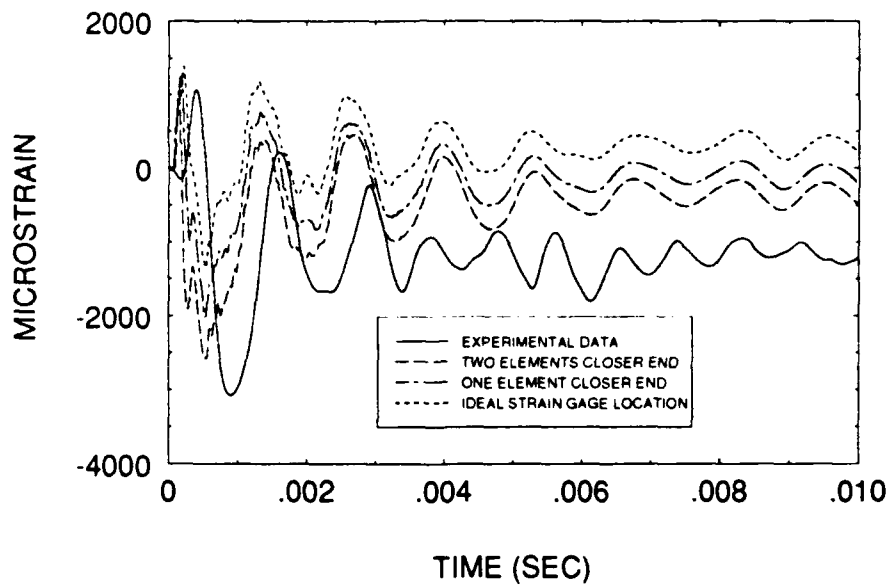


Figure IV.12. End effect sensitivity results. (A1 axial)



**Figure IV.13. End effect sensitivity results.  
(A2 Hoop)**



**Figure IV.14. End effect sensitivity results.  
(A2 Axial)**

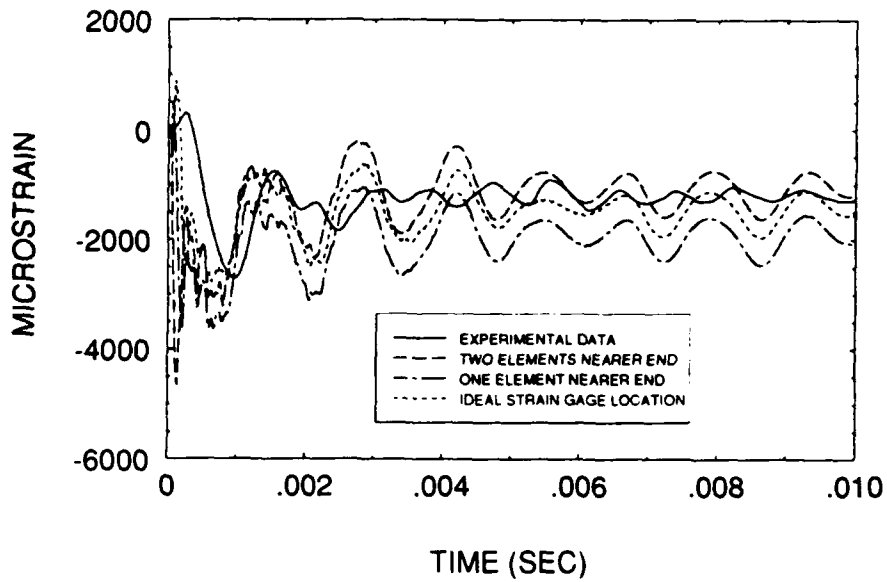


Figure IV.15. End effect sensitivity results.  
(C1 Axial)

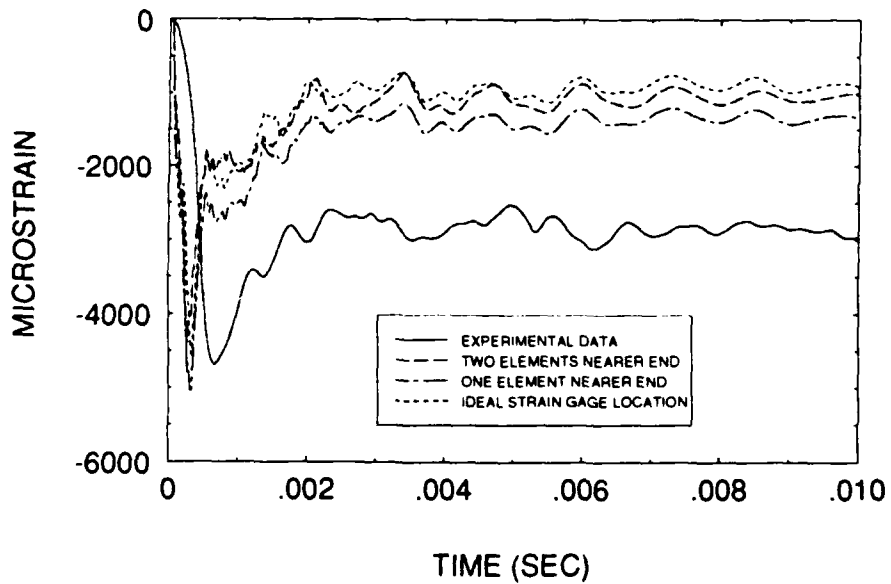


Figure IV.16. End effect sensitivity results.  
(C2 Hoop)

described in the previous paragraph would tend to move the high strain location nearer to the end plate by weakening the material near the end plate. Only the positions with useable experimental results are shown. In four of the five cases (positions A1 axial, A2 hoop, C1 axial and C2 hoop), if asymmetry effects are taken into account, the element one nearer to the end from the actual strain location provides a better estimate of the actual strain measured during the underwater explosion test. At the fifth location (A2 axial), the second element closer to the end provides the best results. These results require additional study to separate and quantify the effect of the phenomena.

## **2. SHELL FORMULATION, QUADRATURE RULE AND INTEGRATION TIME INCREMENT SENSITIVITY ANALYSES**

In addition to the above end effects, there was some concern that the mid plane reference for the thin shell element would result in a greater flexible length than the actual physical model. This concern was based on the fact that the mass and stiffness of the end plates is concentrated into a planar surface co-located with the mid plane of the end plate in the thin shell analysis. This resulted in the shell portion of the structure being one inch longer in the numerical model than the physical model. This problem could have been avoided by using the Hughes/Liu formulation and shifting the reference plane to the inner surface of the



shell. To resolve this issue a study was conducted to compare the performance of different types of thin and thick shell element formulations.

Results from the Belytschko/Tsay/Lin shell formulation were compared to results from the same model using the Hughes/Liu shell formulation. As stated earlier, the Belytschko/Lin/Tsay shell has the advantages of increased computational efficiency and a high degree of stability with large deformations at the expense of reduced accuracy at high levels of plastic strain. The major difference between the two formulation stems from the fact that the element normal direction is updated periodically in the Hughes/Liu formulation. The Belytschko/Lin/Tsay formulation assumes negligible out of plane deformations, and therefore, does not update the shell normal. As a result, the inaccuracy of the Belytschko/Lin/Tsay formulation will increase as shell deformation becomes significant.

The models used to compare the two formulations were identical in all aspects with the exception of the shell formulation. The center line plane was used for the reference on both models. The results confirmed that the strain levels encountered in this underwater explosion test were small enough to support use of the Belytschko/Lin/Tsay formulation. However, it was apparent that differences did occur for positions with significant plastic strain in the axial direction (Positions A1, A2, B3, C1, and C2). Although the

differences in these cases were not significant enough to require use of the Hughes/Liu formulation, it is also noted that higher strain may result in larger differences. Therefore the Belytschko/Lin/Tsay formulation should not be used in cases where significant denting occurs unless stability problems occur while using the Hughes/Liu formulation.

As stated earlier, the presence of high strain gradients near the end plates causes small changes in end condition or distance to be significant. When it became apparent that end effects would be important in the results an investigation was performed to determine if an eight node brick shell formulation would provide more accurate results near the end of the cylinder. The thin shell formulation results as well as the experimental results were compared to results from a model computed using eight node brick shell elements. All three formulations are compared to experimental results in figures IV.17 through IV.27. The following information can be gleaned from the plotted results. First, it is apparent that the greatest differences occur near the positions with the highest strains. At the same time, it can be noted that there is virtually no difference at the locations with no permanent strain. Second, as shown in figures IV.17, IV.18, IV.24, IV.25 and IV.27, it is clear that there is a significant difference between the eight node brick shell results and the Belytschko/Lin/Tsay results at the

locations with high levels of permanent plastic strain. However, contrary to the expected results, the eight node brick shell results move further from the expected values than the other formulations. It is also noted that the Hughes/Liu formulation lies between the eight node brick shell and the Belytschko/Lin/Tsay formulation.

Additional research was performed to determine the cause of the disparities. The study revealed that the eight node brick shell is sensitive to integration time increment and will move marginally closer to the thin shell results if time integration is cut in half. However, the overall shift is only about 10 percent of the total difference. Quadrature rule (number of points used in the Gauss quadrature numerical

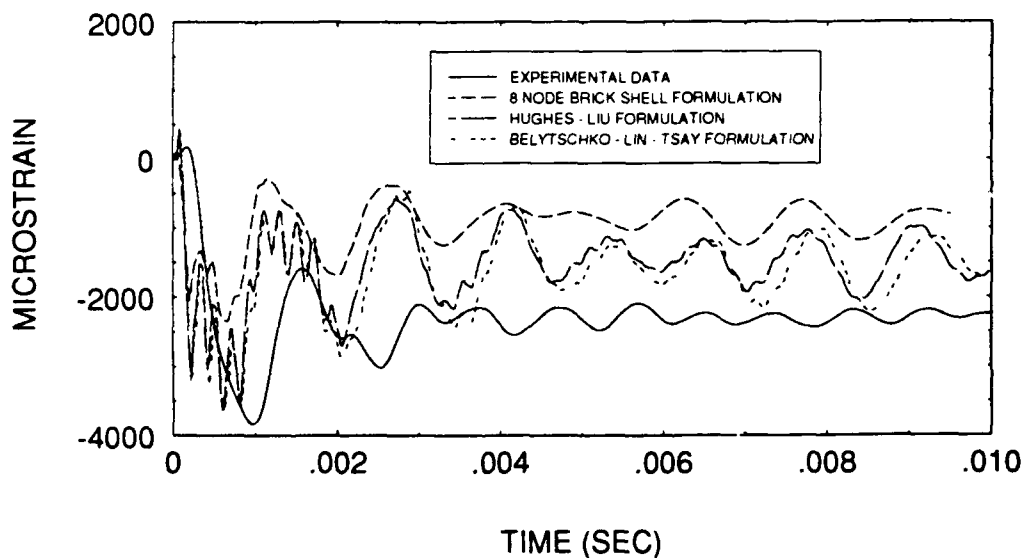


**Figure IV.17. Shell formulation sensitivity results. (A1 Axial)**

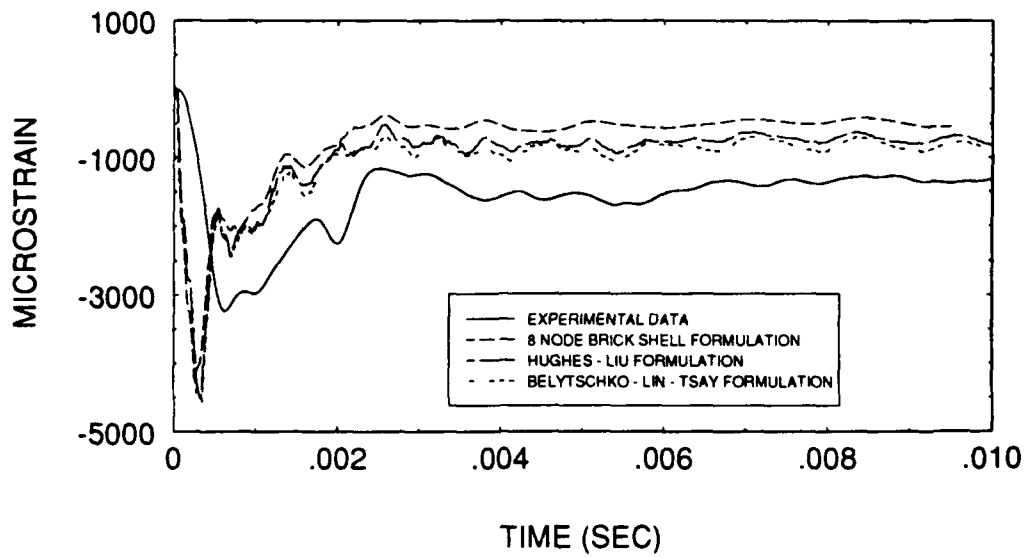


**Figure IV.18. Shell formulation sensitivity results.  
(A2 Hoop)**

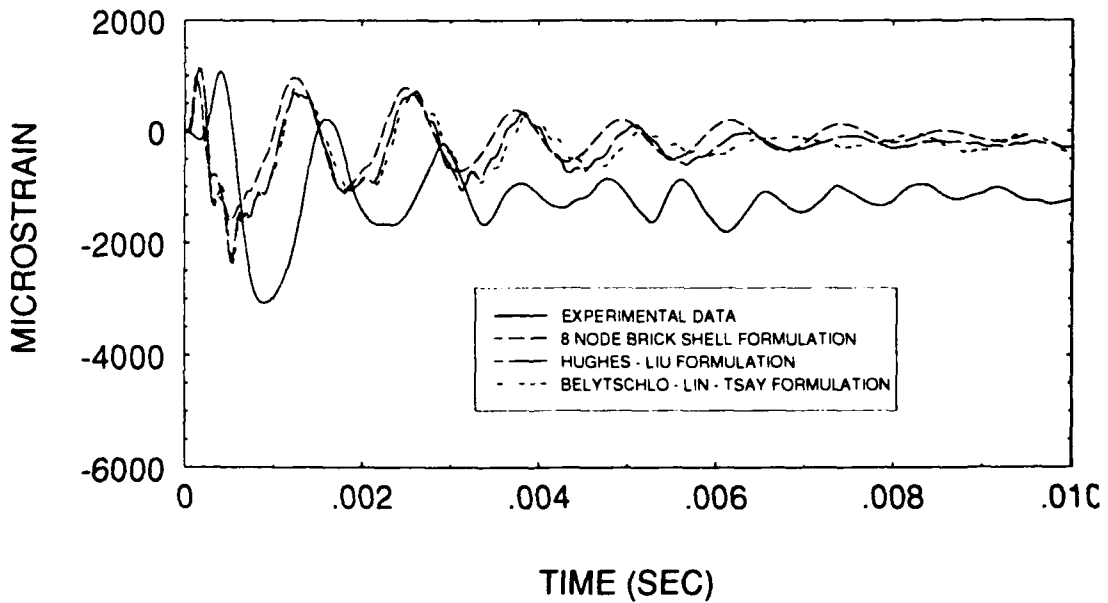


**Figure IV.19. Shell formulation sensitivity results  
(A2 Axial)**

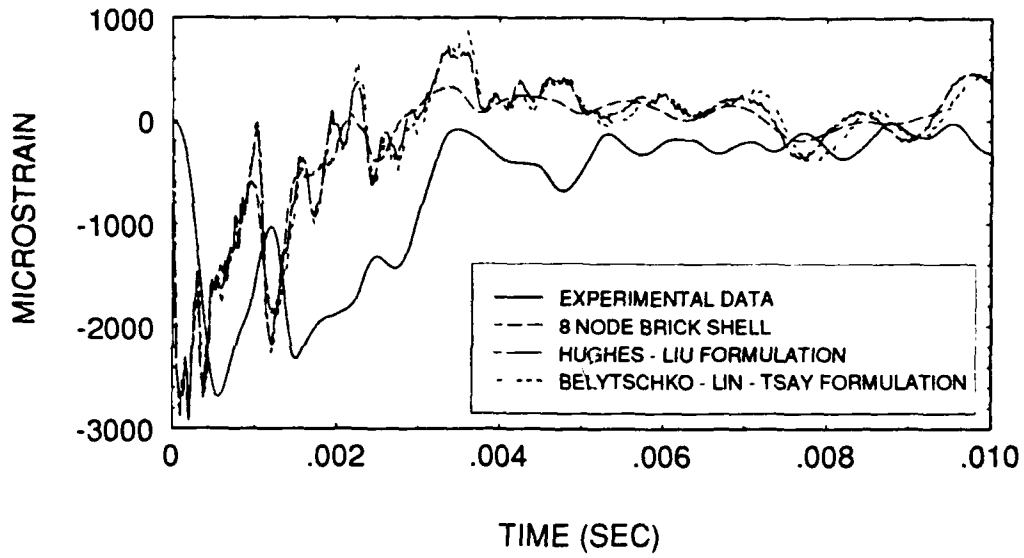


**Figure IV.20. Shell formulation sensitivity results.  
(B1 Hoop)**

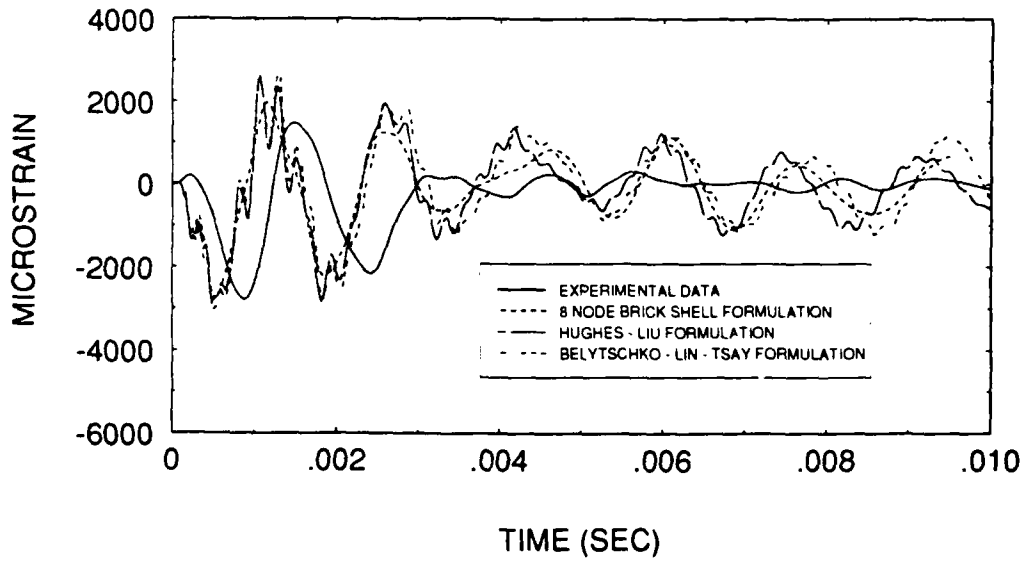


**Figure IV.21. Shell formulation sensitivity results.  
(B1 Axial)**

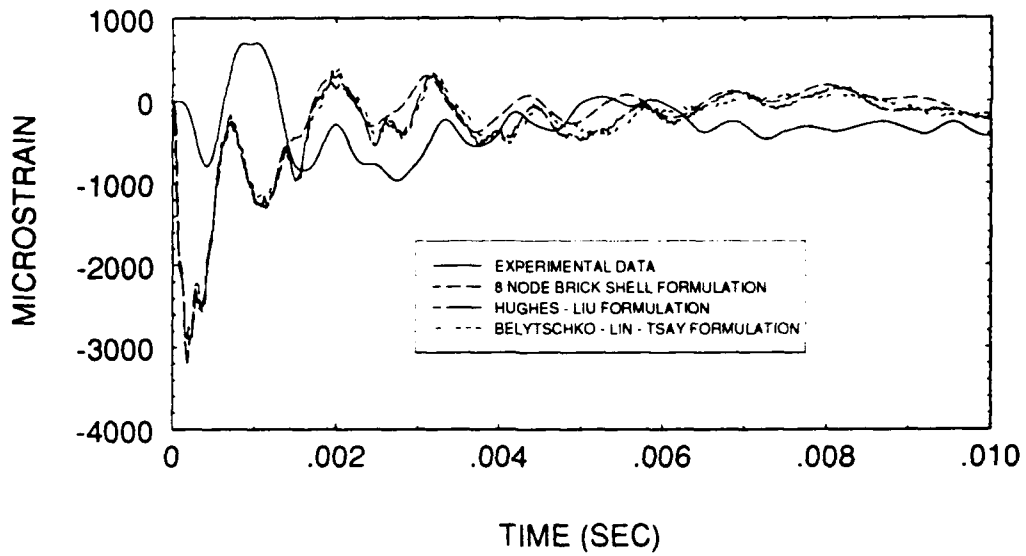


**Figure IV.22. Shell formulation sensitivity results. (B2 Hoop)**

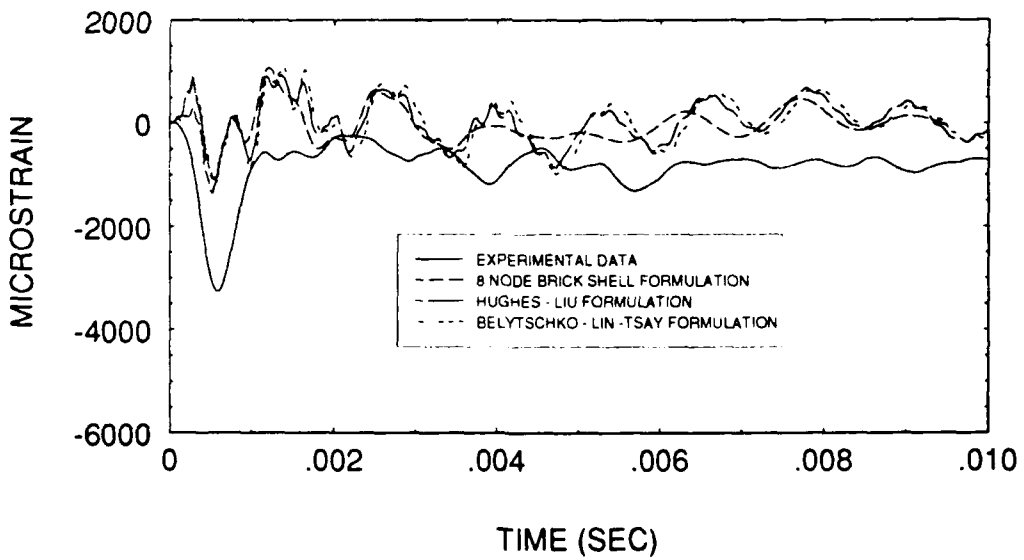


**Figure IV.23. Shell formulation sensitivity results. (B2 Axial)**

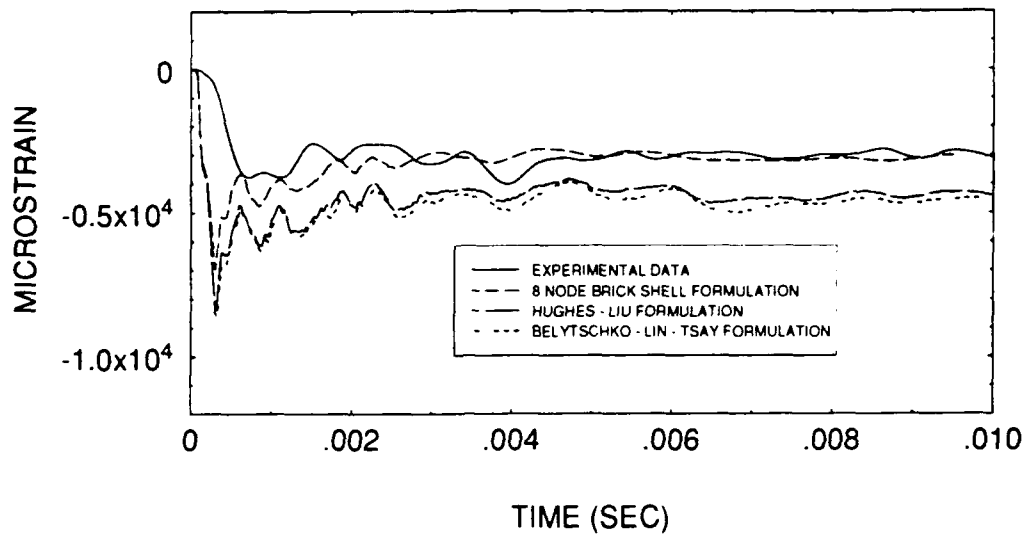


Figure IV.24. Shell formulation sensitivity results.  
(B3 Hoop)

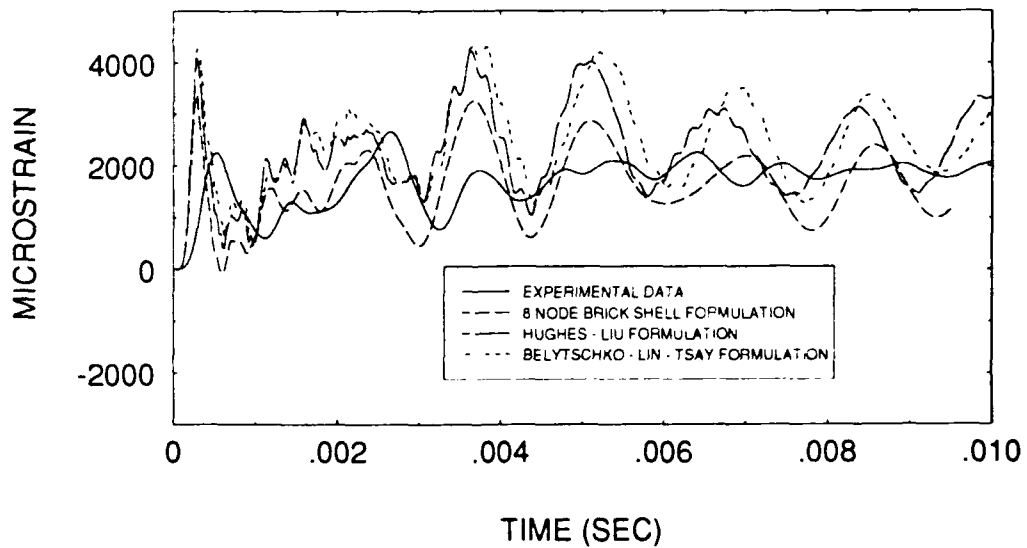


Figure IV.25. Shell formulation sensitivity results.  
(B3 Axial)

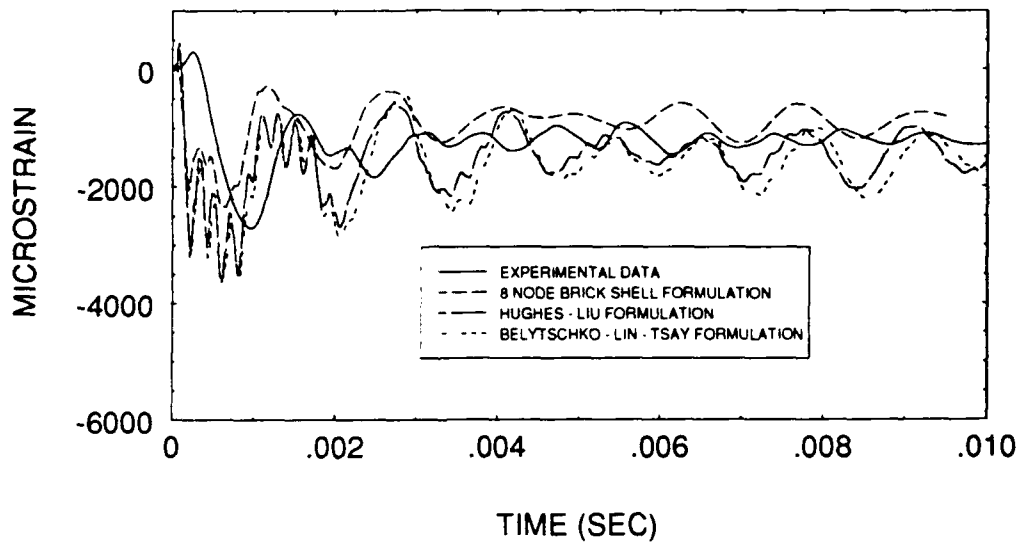


Figure IV.26. Shell formulation sensitivity results.  
(C1 Axial)

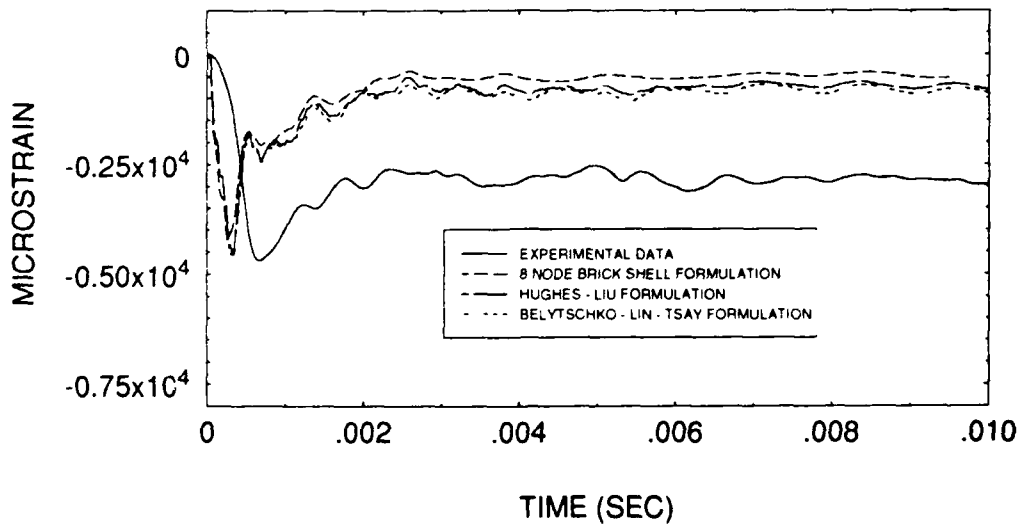
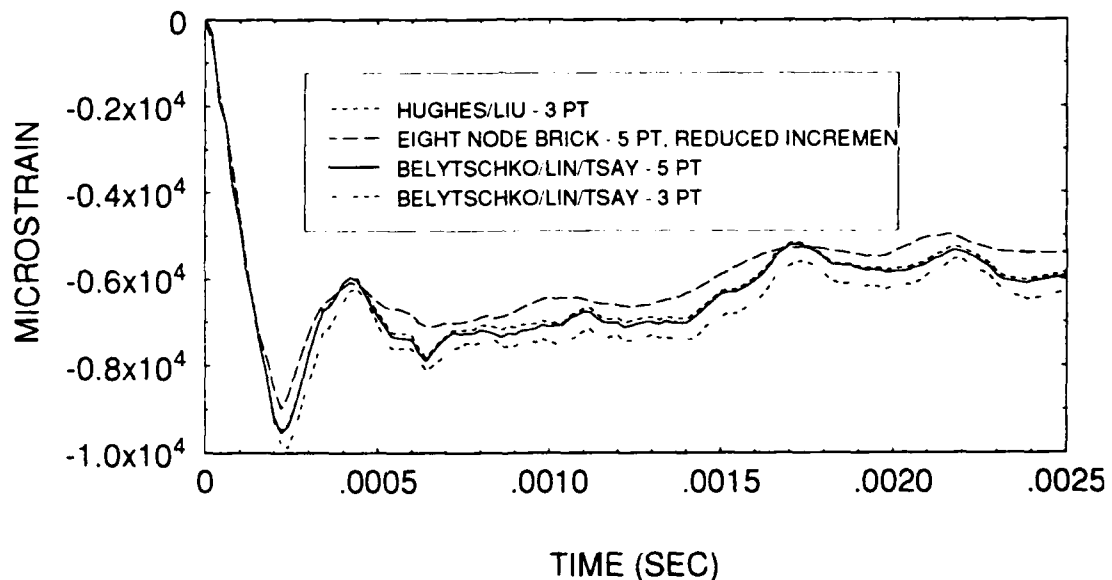


Figure IV.27. Shell formulation sensitivity results.  
(C2 Hoop)



integration scheme) proved to be a more significant effect. Use of five point quadrature moved the three results closer together while having the most profound effect on the Belytschko/Lin/Tsay formulation. Again, the affect of quadrature rule affected the thick shell results only marginally. Figure IV.28 shows the combined results for the location with greatest plastic deformation.



**Figure IV.28. Effect of changing quadrature rule and time integration increment at location of highest strain (A1 and C1 hoop).**

In summary, all three formulations appear to be satisfactory as long as care is used in designing the mesh and selecting the integration time and quadrature integration

rule parameters. Specifically, when using Belytschko/Lin/Tsay formulations in areas with relatively high strain, the number of quadrature points should be increased until stable results are achieved. When using eight node brick shell elements, integration time increment must be selected with care but number of quadrature points seems to be less critical. The Hughes/Liu formulation appeared to be relatively insensitive to both quadrature rule and integration time increment.

Reference 13 provides some useful thumbrules for selection of time increments. The following criteria are recommended.

$$\Delta t \approx 0.9 \frac{V}{(A_b c)} \text{ for brick shells}$$

$$\Delta t \approx 0.9 \frac{A_s}{Dc} \text{ for thin shells}$$

*V* - element volume

$\Delta t$  - time increment

$A_s$  - maximum surface area

*D* - maximum diagonal

*c* - speed of sound in the material

$A_b$  - maximum area of any surface

The above criteria were found to be adequate except for the highest strain areas where the thick shell element rule did

not provide stable solutions. In areas such as A1 and C1, a value of the integration time increment half of the above recommendation proved to be satisfactory for the eight node brick shell.

### **3. ROTATION SENSITIVITY ANALYSIS**

A sensitivity analysis was performed to determine the effect of an in plane rotation away from the expected symmetric orientation in an effort to explain the cause of the asymmetric results of the underwater explosion test. It was hypothesized that an unplanned rotation greater than ten degrees would have been detected by the personnel performing the test. Four different models were run within this range representing rotations of 0.0, 2.5, 5.0 and 10.0 degrees. The results are shown along with experimental results where available in figures IV.29 through IV.42. The following observations are made concerning the results. First, the most dramatic affects are on the reverse side of the cylinder at position B3 (Figures IV.37 and IV.38). The results show that the differential between the numerical and experimental results at position B3 can be explained by a six to eight degree rotation from the symmetric configuration. Rotational effects at locations B1 and B2 on the centerline (Figures IV.33 through IV.36) are insignificant. Hoop strain at position C2 (Figure IV.41) is approximately 60 percent

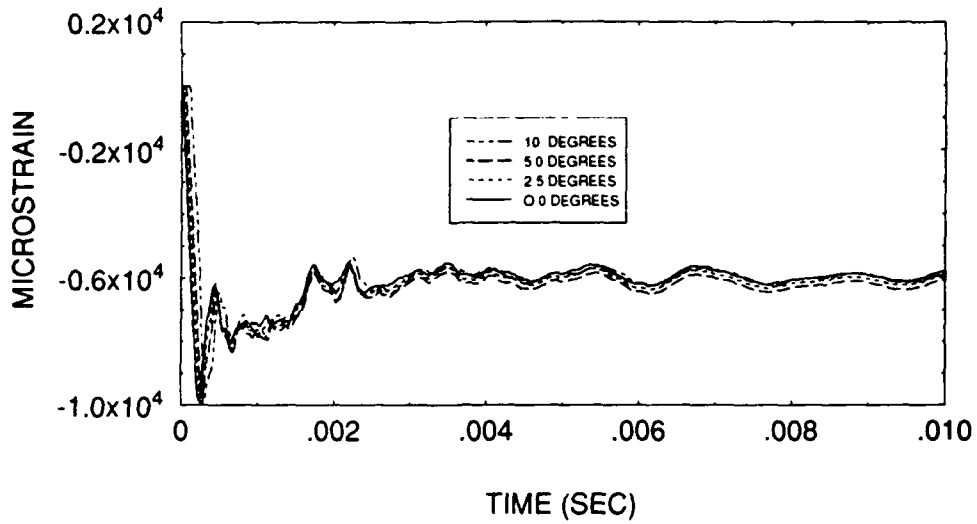


Figure IV.29. Rotation sensitivity results.  
(Al Hoop)

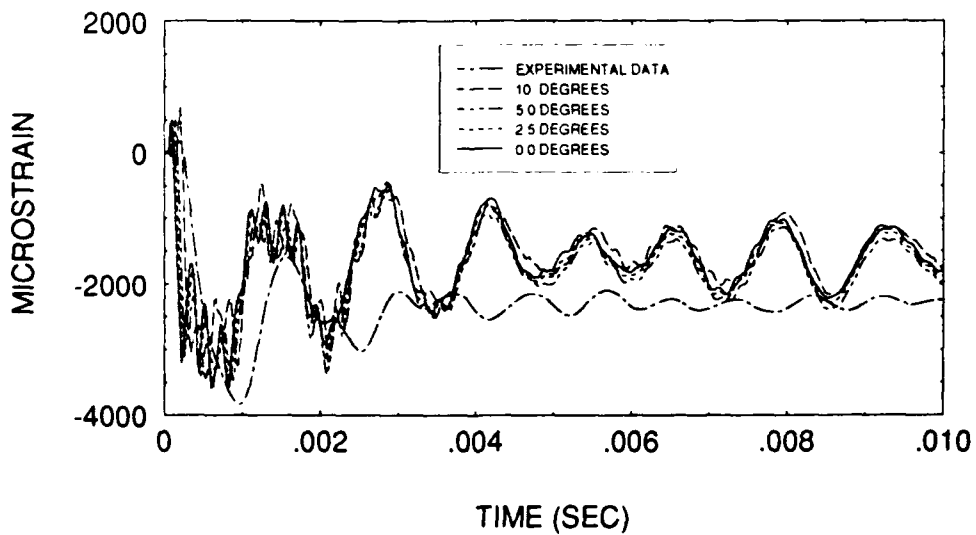


Figure IV.30. Rotation sensitivity results.  
(Al Axial)

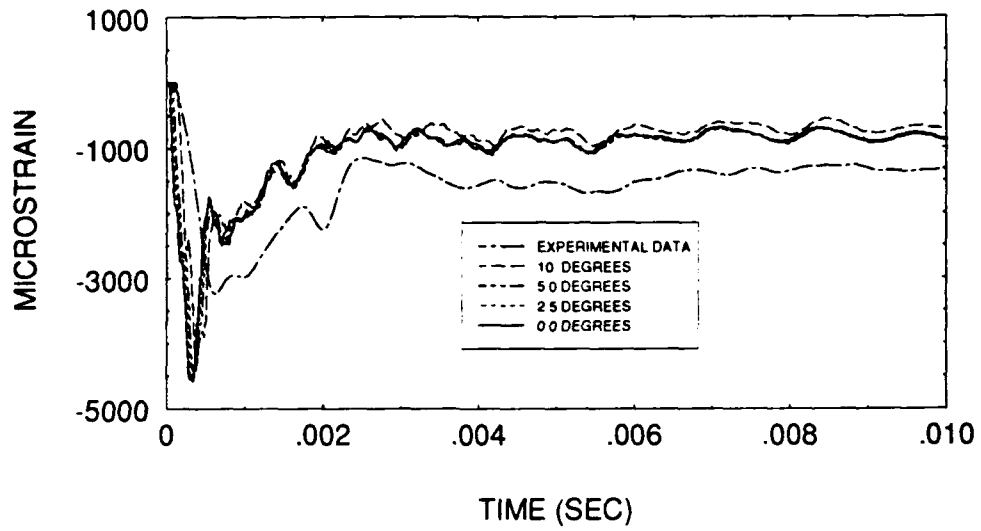


Figure IV.31. Rotation sensitivity results.  
(A2 Hoop)

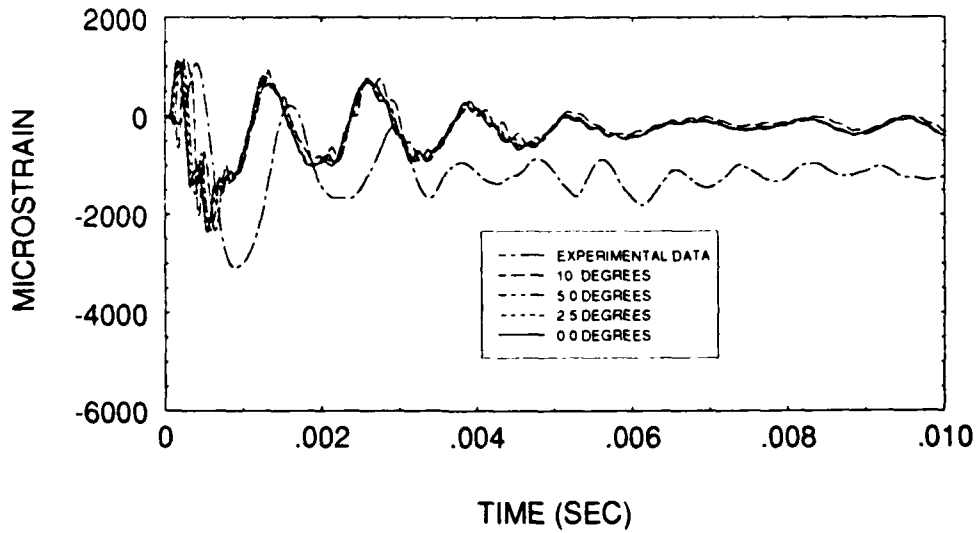


Figure IV.32. Rotation sensitivity results.  
(A2 Axial)

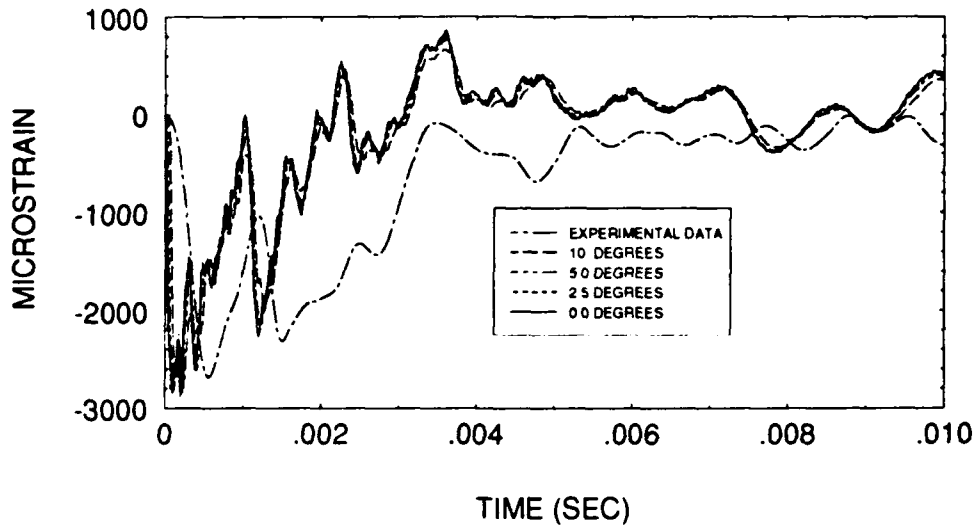


Figure IV.33. Rotation sensitivity results.  
(B1 Hoop)

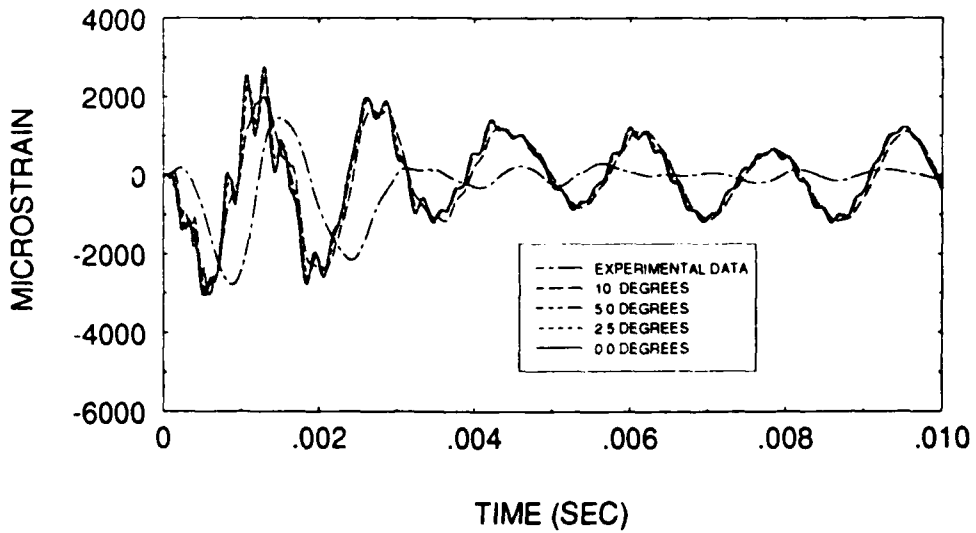
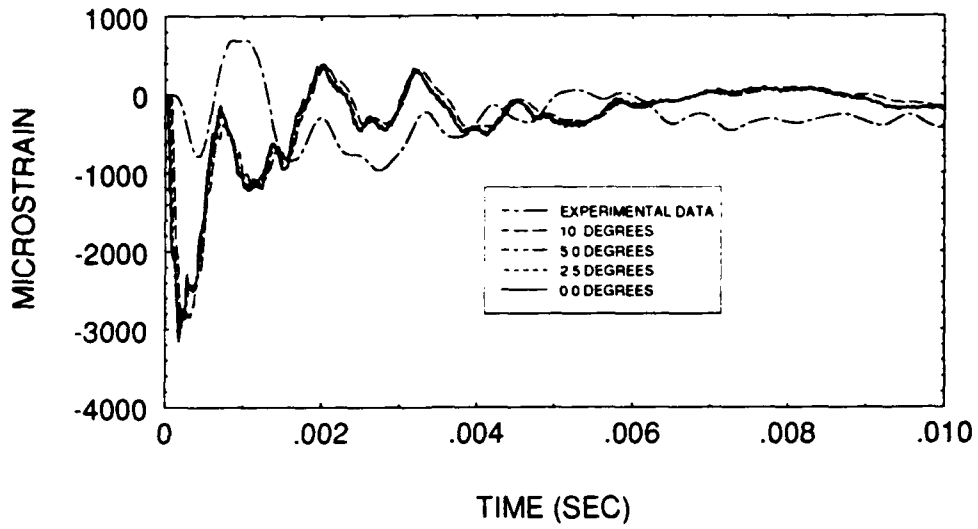
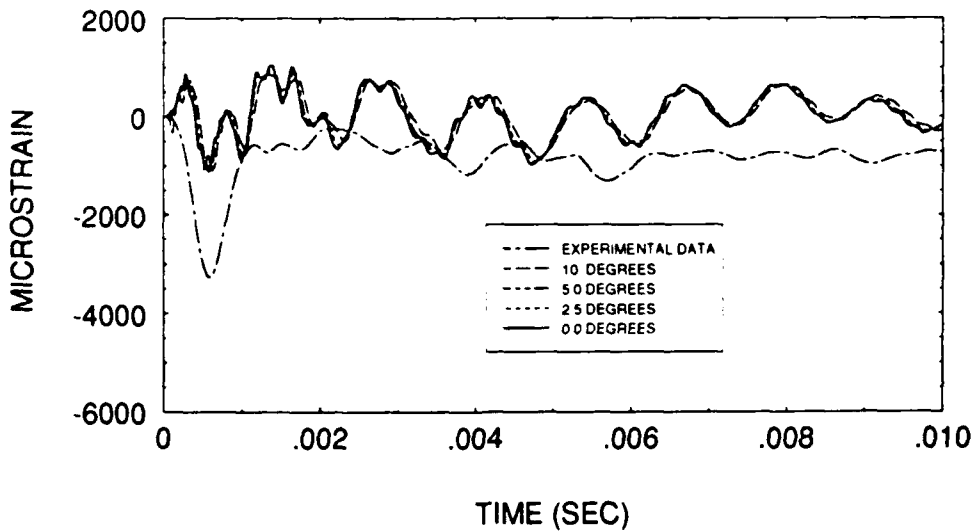


Figure IV.34. Rotation sensitivity results.  
(B1 Axial)



**Figure IV.35. Rotation sensitivity results.  
(B2 Hoop)**



**Figure IV.36. Rotation sensitivity results.  
(B2 Axial)**

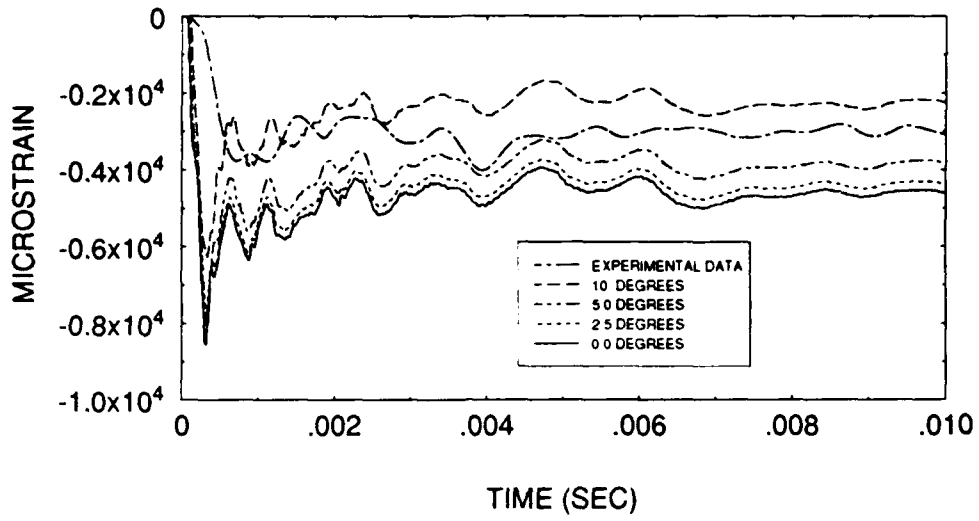


Figure IV.37. Rotation sensitivity results.  
(B3 Hoop)

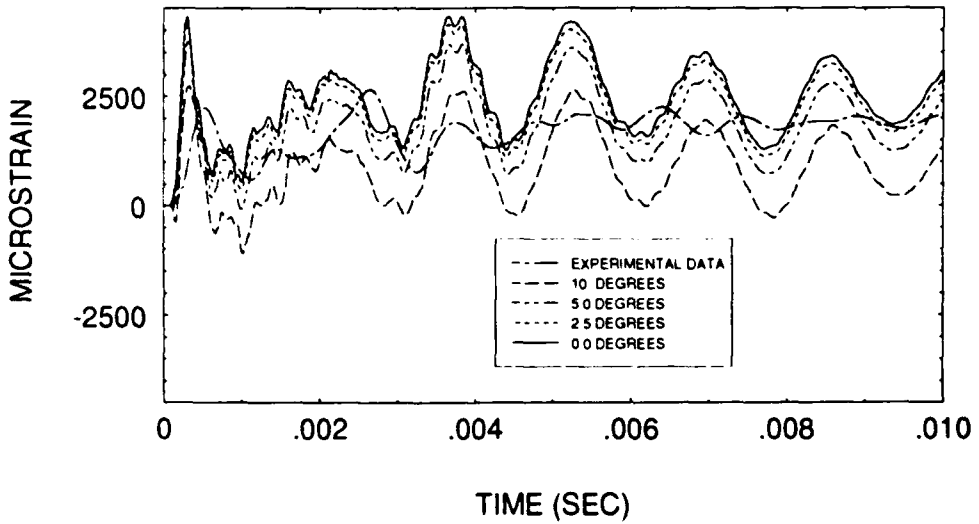


Figure IV.38. Rotation sensitivity results.  
(B3 Axial)



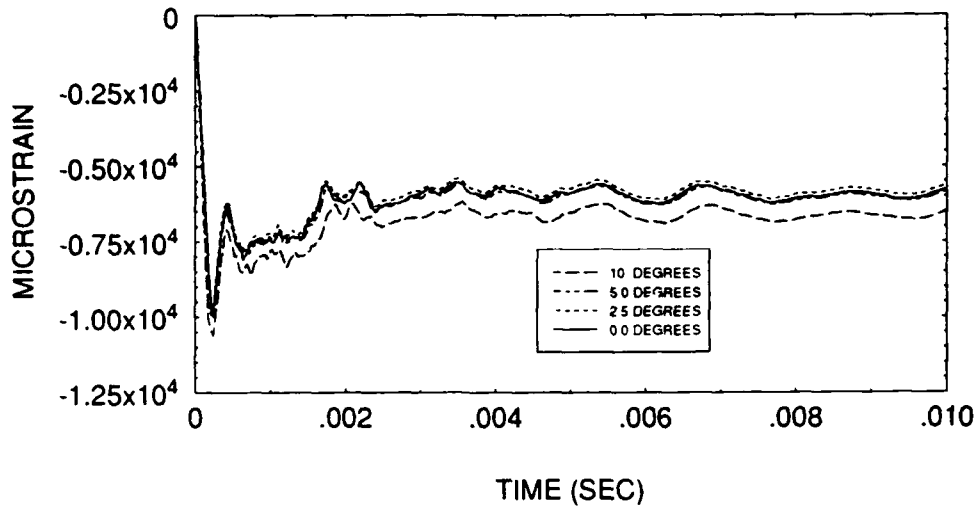


Figure IV.39. Rotation sensitivity results.  
(C1 Hoop)

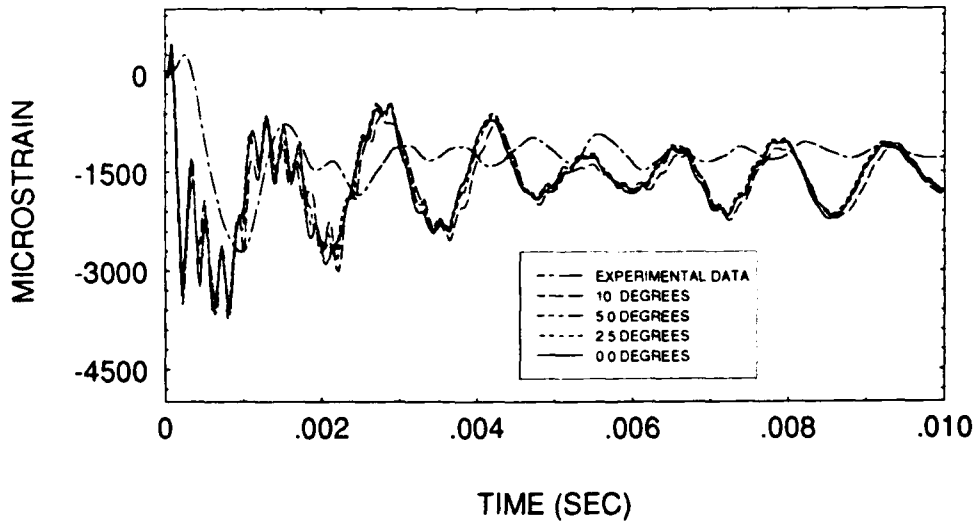


Figure IV.40. Rotation sensitivity results.  
(C1 Axial)

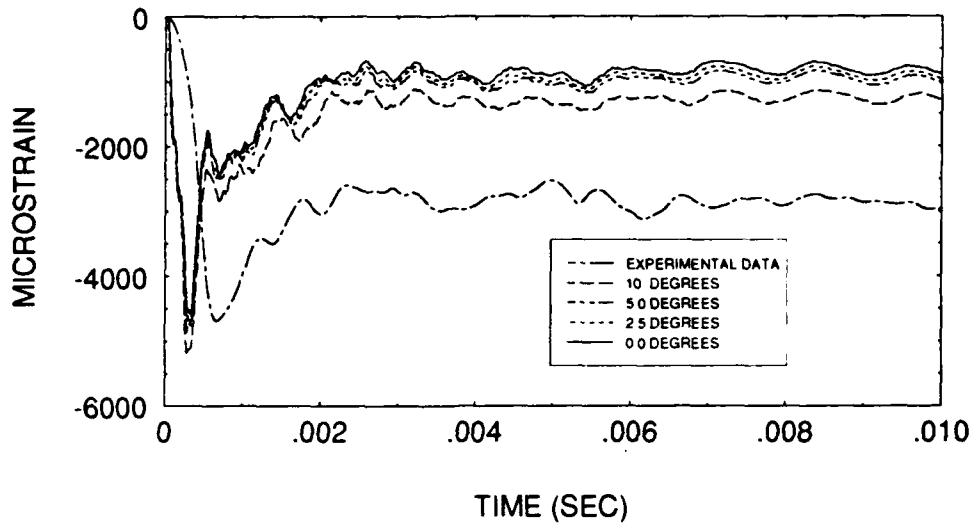


Figure IV.41. Rotation sensitivity results.  
(C2 Hoop)

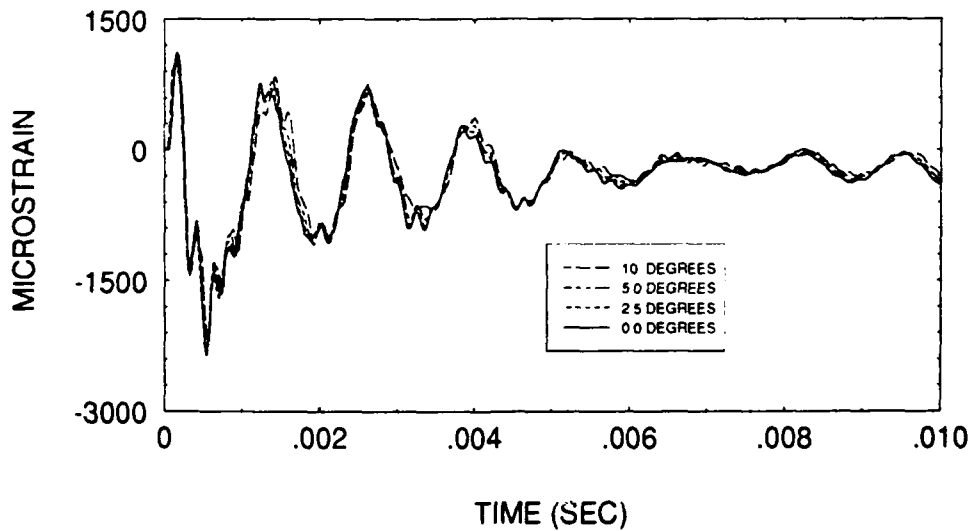


Figure IV.42. Rotation sensitivity results.  
(C2 Axial)

higher than the hoop strain at position A2 (Figure IV.32) with a rotation of ten degrees. This is also consistent with the experimental data. Similar positive results were obtained for positions A1 and C1 axial strains. It was further discovered that rotating the cylinder about its axis could further improve the results. However, even though these rotations did improve the results, significant differences still exist between the experimental and numerical strains at the ends of the cylinders. Although it is clear that the model can account for rotational effects, it is also clear that other factors are causing the large differences. Once again, welding affects are suspected to be the probable cause.

The important point to note out of these results is that even small rotations from expected orientation can result in significant errors on in expected results. Therefore extreme care must be taken to ensure that instrumentation cable tension and other unanticipated factors do not cause undetected rotations.

#### **4. PHYSICAL FINDINGS**

##### **a. RESPONSE MODES**

It was determined that a cylinder subject to a side on explosion will have three primary response modes. The first mode is an accordion motion. The accordion motion results from the compression and subsequent release of the

cylinder in the axial direction. Figure IV.43 shows a plot of points located at the center of each end plate. It is clear

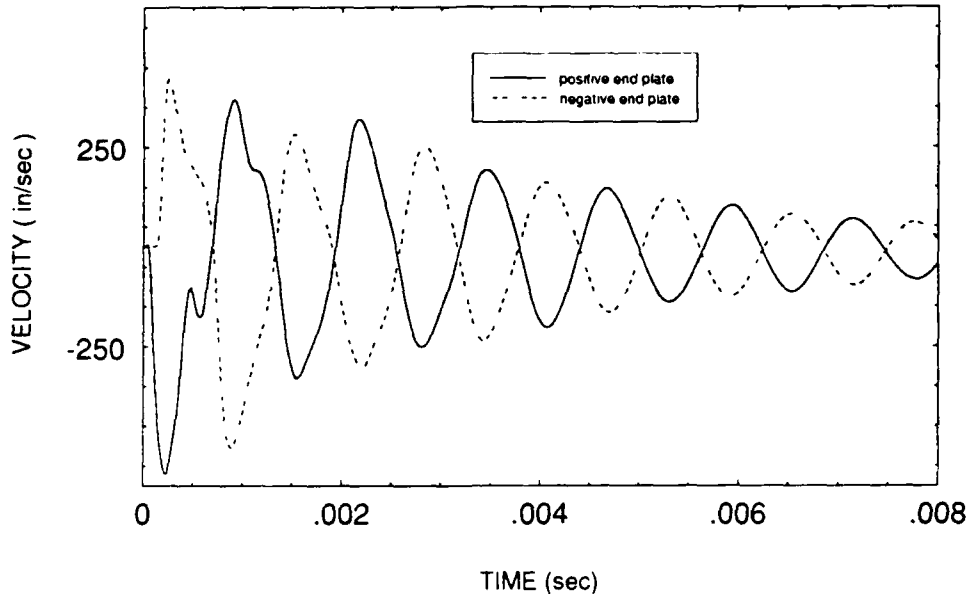


**Figure IV.43. Cylinder accordion motion.**

that the two end plates are travelling in opposite directions at the same time generating the accordion motion.

The cylinder is also subject to a whipping mode parallel to the direction of shock wave travel. The whipping mode is the most significant motion experienced by the cylinder and is caused as a result of the curvature of the shock wave. In the symmetric situation, the shock wave will come in contact with the center of the cylinder first. This will cause the center to move first, followed by the ends. The cylinder will then move in an oscillatory motion that is a function of the stiffness and mass distribution of the cylinder and the water surrounding the cylinder. Figure IV.44

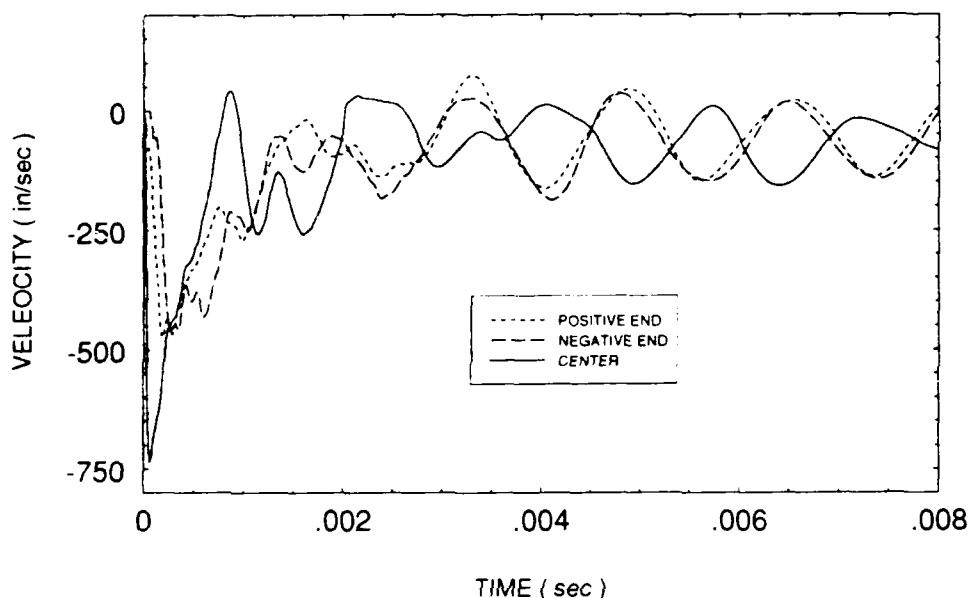


**Figure IV.44. Cylinder whipping motion in plane parallel to shock wave direction.**

shows a plot of a points located at the center and ends of a line located parallel to the axis on the near side of the cylinder. The plot shows that the end plates are moving in the opposite direction of the cylinder throughout the transient response of the cylinder. Figure IV.45 shows a scale factor 20 drawing of the cylinder at two different times. The cylinder's opposite direction of curvature at the two different times is a result of the whipping motion.

The final response mode noted was a breathing motion in the plane perpendicular to the shock wave direction of travel. Although breathing motion also occurred in the direction parallel to the shock wave travel, it was not as obvious since the much larger whipping motion turned out to be

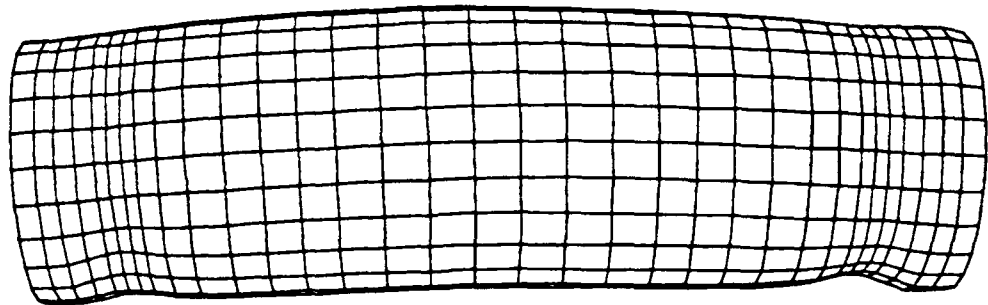
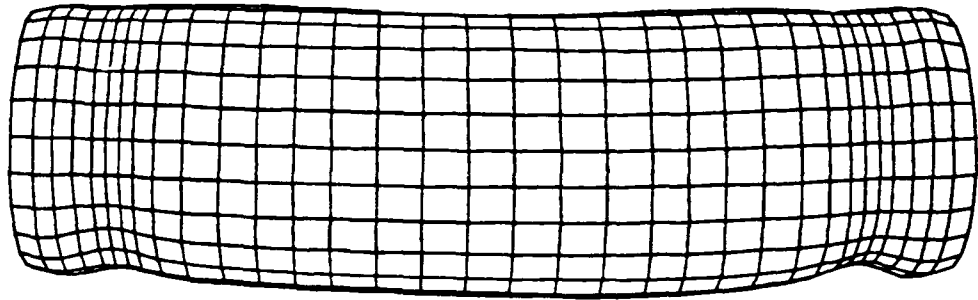


**Figure IV.45. Cylinder curvature as a result of whipping motion (scale factor 20).**

the predominant mode in that direction. Figure IV.46 shows a plot of two points located at the top and bottom of the cylinder in a plane perpendicular to the axis at the axial mid point of the cylinder. It can be observed that the upper

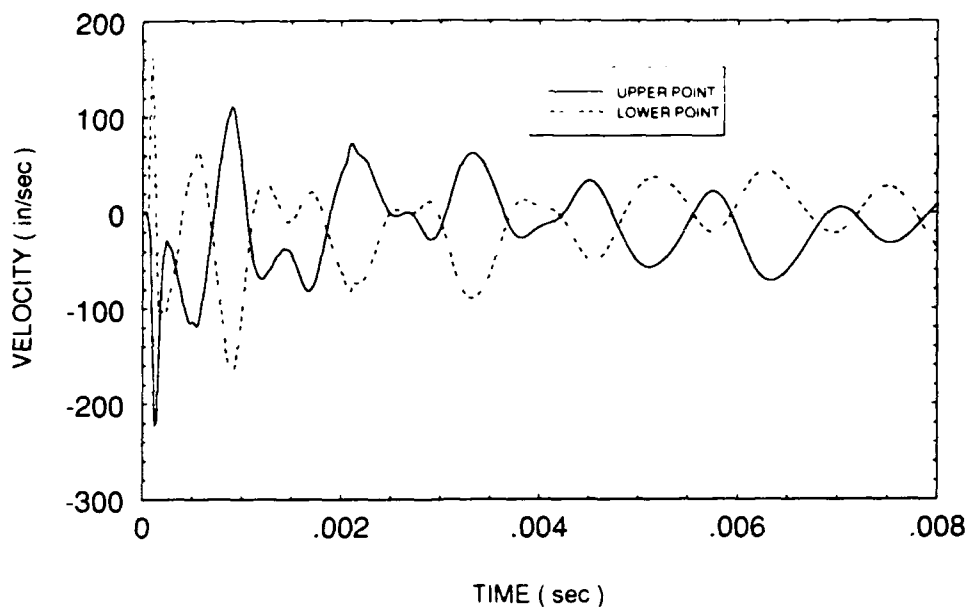


**Figure IV.46. Cylinder breathing motion perpendicular to the shock wave direction of travel.**

point is moving in a direction opposite to the lower point throughout the transient response of the cylinder. The breathing motion is also caused by the compression and subsequent release of the cylinder. Figure IV.47 provides an illustration of the breathing motion. The two scale factor 40 drawings are for two separate times and show the shell first bowed inward toward the axis and then outward away from the axis.

#### **b. ROTATIONAL EFFECTS**

Plastic strain fringe plots generated as a result of the rotation sensitivity analysis revealed some interesting information on the causes of the strain distribution

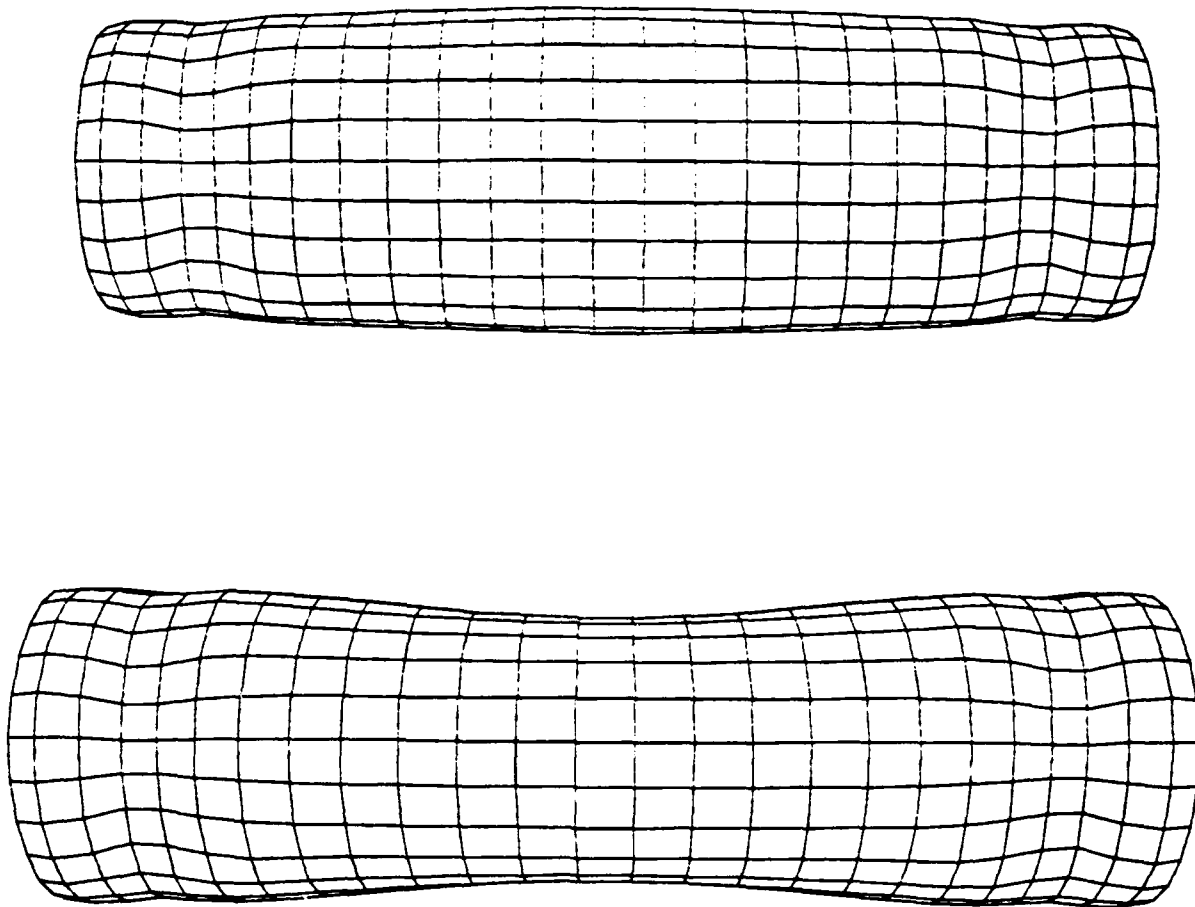


**Figure IV.47. Illustration of cylinder breathing mode at two different times (scale factor 40).**

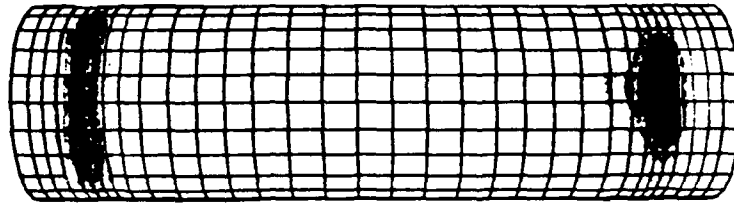
experienced by the cylinder. The experimental results included a reduction in the strain at the rear of the cylinder at position B3, a decrease at A2 relative to C2 and an increase at A1 relative to C1. The fringe plots show why this



strain distribution occurs. Figure IV.48 shows the effective plastic strain distribution for a 7.5 degree rotation. The left side of the cylinder is nearest the charge. The results show that the rotation tends to diffuse the strain around the cylinder on the near end while concentrating it at the far end. This causes the distribution noted for positions A1, C1, A2 and C2. At the same time, the high stress region on the reverse side of the cylinder tends to move away from the charge. This placed location B3 in a lower strain region which led to the experimental and numerical results noted at position B3.

THICK SHELL MODEL  
time = .59798E-02  
fringes of eff. plastic strain  
min= 0.000E+00 in element 960  
max= 7.104E-03 in element 433

fringe levels  
1.009E-03  
2.321E-03  
3.552E-03  
4.783E-03  
6.015E-03



THICK SHELL MODEL  
time = .59798E-02  
fringes of eff. plastic strain  
min= 0.000E+00 in element 960  
max= 7.104E-03 in element 433

fringe levels  
1.009E-03  
2.321E-03  
3.552E-03  
4.783E-03  
6.015E-03

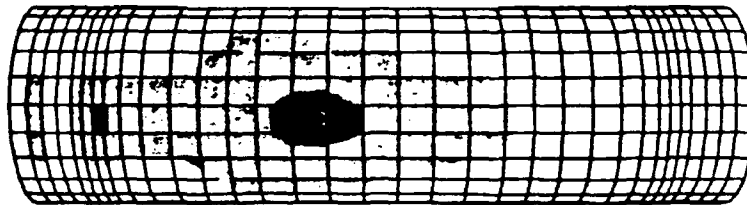


Figure IV.48. Effective plastic strain distribution for near and remote side of cylinder with 7.5 degrees of rotation.

## V. CONCLUSIONS AND RECOMMENDATIONS

### A. CONCLUSIONS.

#### 1. NUMERICAL MODELLING

Two general conclusions can be reached from the material contained in this report. First, the USA/DYNA3d connection is successful and can replicate the response of simple analytical models.

Second, numerical modeling can predict the response of a simple cylinder to an underwater explosion. Far field numerical predictions generally match experimental results if rotation and end effects resulting from fabrication caused material property changes are correctly modelled. It was found that results in high strain areas are extremely sensitive to shell formulation, mesh design, quadrature rule and integration time increment. The best results were achieved with brick shell elements. However, the eight node brick shell required substantially longer computation times to achieve the desired results because of the need to reduce the integration time increment. In addition, it was found that thin shell formulations can also provide correct results. However, results for the Belytschko/Lin/Tsay formulation appear to be very sensitive to the number of quadrature points

used for the numerical integration scheme in high strain areas.

## **2. PHYSICAL ASPECTS**

Primary damage areas are near the ends of the cylinder on the side nearest the charge where the stiff, heavy, flat end plates caused a concentration of the effective plastic strain. Damage also occurred on the reverse side as a result of a bending effect similar to that described in the near field results. The cylinder experienced breathing, whipping and accordion response modes.

In addition, it was discovered that rotation tends to diffuse strain on the end nearest the charge while concentrating the strain at the far end on the side nearest the charge. The high strain area located at the center of the cylinder on the reverse side tends to migrate toward the end most remote from the charge.

## **B. RECOMMENDATIONS.**

### **1. TOPICS FOR ADDITIONAL STUDY.**

#### **a. WELDING FABRICATION EFFECTS.**

An analysis should be performed to quantify the relative effect that the change in material properties generated by the welding fabrication process has on the numerical results. This analysis could include the measurement of material properties near a weldment. These

properties could then be added as a separate material in the numerical model.

**b. EIGHT NODE BRICK SHELL SENSITIVITY ANALYSES.**

Although it was fairly clear that the eight node brick shell formulation comes closest to predicting the overall response of the shell, it was also noted that the formulation is very sensitive to integration time increment in areas with high strain. Commonly used thumbrules did not appear to be adequate in this case. In addition, additional analyses need to be performed to determine the mesh sensitivity of the eight node brick shell in this model.

**c. FAILURE CRITERIA.**

This study was performed on a model with relatively low total plastic strain (less than one percent) . In order to deal with larger strains, a failure model must be introduced into the material modelling of the cylinder. The model should include structural instability as well as material rupture criteria.

**d. NEAR FIELD EXPERIMENTATION**

Although the numerical predictions appear to be physically correct, the physical results obtained using them cannot be assumed completely correct until they are confirmed with experimental results. A study should be conducted to compare near field experimental results with numerical predictions.

## 2. RECOMMENDATIONS TO IMPROVE TEST CONTROL.

Several factors made the comparison of the numerical to experimental results difficult. If properly controlled, the analysis process could be simplified. First, rotation of the cylinder must be carefully controlled. Second, unless specifically required, high strain gradient areas should be avoided. Placement of the strain gages becomes critical in these locations as does mesh design and integration time increment. If these areas cannot be avoided, additional sensitivity analyses may be required to determine the adequacy of the mesh and integration time increment. Finally, analysis near welded seams should be avoided unless the effects can be quantified. If near weld analysis cannot be avoided, consideration should be given to restoring the heat treatment after the weld process.

## LIST OF REFERENCES

1. Boticario, L. A., *Dynamic Response of Cylindrical Shells to Underwater End-On Explosion*, Master's Thesis, Naval Postgraduate School, Monterey, California, 1991.
2. Kwon, Y. W., Fox, P. K. and Shin, Y. S., "Response of a Cylindrical Shell Subject to a Near Field Side-On Explosion," *Proceedings of the 62nd Shock and Vibration Symposium, Volume II*, pp 163 - 178, Pasadena, California, October 1990.
3. Livermore Software Technology Corporation Report 1018, *VEC/DYNA3D User's Manual (Nonlinear Dynamic Analysis of Structures in Three Dimensions)*, by D. W. Stillman and J. O. Hallquist, June 1990.
4. Livermore Software Technology Corporation Report 1019, *LS-INGRID: A Pre-processor and Three-Dimensional Mesh Generator for the Programs LS-DYNA3D, LS-NIKE3D and TOPAZ-3D, version 3.0*, by D. W. Stillman and J. O. Hallquist, June 1991.
5. Livermore Software Technology Corporation Report 1009, *LS-TAURUS, An Interactive Post-Processor for the Programs LS-DYNA3D, LS-NIKE3D and TOPAZ-3D*, by J. O. Hallquist, April 1990.
6. Deruntz, J. A. Jr. and Rankin, C. C., "Applications of the USA-Stags Codes to Underwater Shock Problems, Palo Alto, California, 1990.
7. Geers, T. L., "Residual Potential and Approximate Methods for Three Dimensional Fluid-Structure Interaction Problem," *Journal of the Acoustic Society of America*, v. 49, pp 1505-1510, 1971.
8. Huang, H., Everstine, C. C. and Wang, Y. F., "Retarded Potential for Analysis of Submerged Structures Impinged by Weak Shock Waves," *Computational Methods for Fluid-Structure Interaction Problems*, AMD-Vol 26, American Society of Mechanical Engineers, December 1977.
9. Huang, H., "Transient Interaction of Plane Waves With a Spherical Elastic Shell," *Journal of the Acoustic Society of America*, v. 45, pp 661-670, 1969.

10. Ugural, A. C. and Fenster, S. K., *Advanced Strength and Applied Elasticity, Second S. I. Edition*, Elsevier Science Publishing Co. Inc., New York, New York, p 398, 1987.
11. Belytschko, T. and Tsay, C. S., "Explicit Algorithms for Non-Linear Dynamics of Shells," AMD-Vol 48, American Society of Mechanical Engineers, pp 209-231, 1981.
12. Hughes, T. J. R., *The Finite Element Method. Linear Static and Dynamic Finite Element Analysis*, Prentice Hall, Englewood Cliffs, New Jersey, 1987.
13. Livermore Software Technology Corporation Report 1009, *LS-DYNA3D Course Notes*, by Hallquist, J. O. and Stillman, D. W., October 1990.



APPENDIX A - SPHERICAL VALIDATION MODEL

**A. INGRID PRE-PROCESSOR INPUT DATA**

```
dn3d vec term 5.0 plti 0.01 prti 1000.

mat 1 type 1 e 9.7e+1 pr 0.3 ro 7.79
    shell endmat

lcd 1 2 0.0 0.0 10.0 0.0
lcd 2 2 0.0 0.00025 10.0 0.00025

plan 2

0 0 0      0 -1 0  0.00001  symm
0 0 0      -1 0 0  0.00001  symm

start
-1 6 -11 ;
-1 6 -11 ;
-1 6 -11 ;
-1. 0. 1.
-1. 0. 1.
-1. 0. 1.
sfi -1 -3 ; -1 -3 ; -1 -3 ; sp 0 0 0 1.
d 0 1 0 0 2 0
d 1 0 0 2 0 0
pri -1 -3 ; -1 -3 ; -1 -3 ; 1 -1.0 0. 0. 0.
thick 0.02
mate 1
end

end
```



46	0.	.457638891244E+00	.1431921869516E+00	.281162222446E+00	0.
47	0.	.5834555357794E+00	.1340278238058E+00	.8008636832237E+00	0.
48	0.	.7017562985420E+00	.1227853149176E+00	.7017562985420E+00	0.
49	1.	-.1772349115154E-17	.3090168535709E+00	.9510565996170E+00	5.
50	0.	.1570491213486E+00	.3061736524105E+00	.9400742285093E+00	0.
51	0.	.127012271444E+00	.2980021728443E+00	.9009568348885E+00	0.
52	0.	.412234539330E+00	.2846010625362E+00	.8520765906612E+00	0.
53	0.	.569706252747E+00	.2663204967976E+00	.7775039076805E+00	0.
54	0.	.6357857704163E+00	.2437124401331E+00	.6857857704163E+00	0.
55	1.	-.6743750086005E-16	.4539906680584E+00	.8910064697266E+00	5.
56	0.	.1431921869516E+00	.4506085813046E+00	.881162222446E+00	0.
57	0.	.2846010625362E+00	.4392809569836E+00	.8520765906612E+00	0.
58	0.	.4201654195786E+00	.4201654195786E+00	.8043146729469E+00	0.
59	0.	.5461454391479E+00	.3937847912312E+00	.7393637299538E+00	0.
60	0.	.6594369411469E+00	.3609513640404E+00	.6594369411469E+00	0.
61	1.	-.0419267267305E-17	.5877855420113E+00	.8090168237686E+00	5.
62	0.	.1340278238058E+00	.5836555957794E+00	.8008636832237E+00	0.
63	0.	.2846010625362E+00	.569706252747E+00	.7775039076805E+00	0.
64	0.	.4201654195786E+00	.5461454391479E+00	.7393637299538E+00	0.
65	0.	.5461454391479E+00	.5135421156883E+00	.6874219775200E+00	0.
66	0.	.6594369411469E+00	.4727278351784E+00	.6231029062027E+00	0.
67	1.	.0000000000000E+00	.7071068286896E+00	.7071068286896E+00	5.
68	1.	.1227853149176E+00	.7017562985420E+00	.7017562985420E+00	0.
69	1.	.1431921869516E+00	.6857857704163E+00	.6857857704163E+00	0.
70	1.	.1570491213486E+00	.6594369411469E+00	.6594369411469E+00	0.
71	1.	.1772349115154E-17	.6231355062027E+00	.6231355062027E+00	0.
72	0.	.1980168237686E+00	.5773503184319E+00	.5773503184319E+00	0.
73	1.	.4201654195786E-17	.8090168237686E+00	-.5877854824066E+00	5.
74	1.	.1340278238058E+00	.8008636832237E+00	-.5836555957794E+00	0.
75	0.	.2846010625362E+00	.7775039076805E+00	-.569706252747E+00	0.
76	0.	.4201654195786E+00	.7393637299538E+00	-.5461454391479E+00	0.
77	0.	.5461454391479E+00	.6874219775200E+00	-.5135421156883E+00	0.
78	0.	.6594369411469E+00	.6231029062027E+00	-.4727278351784E+00	0.
79	1.	.0000000000000E-16	.8910064697266E+00	-.4539906680584E+00	5.
80	0.	.1431921869516E+00	.881162222446E+00	-.4506085813046E+00	0.
81	0.	.2846010625362E+00	.8520765906612E+00	-.4392809569836E+00	0.
82	1.	.4201654195786E+00	.8043146729469E+00	-.4201654195786E+00	0.
83	1.	.5461454391479E+00	.7393637299538E+00	-.3937848212031E+00	0.
84	1.	.6594369411469E+00	.6594369411469E+00	-.3609514236450E+00	0.
85	1.	-.0419267267305E-16	.5877855420113E+00	-.3090168237686E+00	5.
86	1.	.1340278238058E+00	.5836555957794E+00	-.3061736524105E+00	0.
87	1.	.1570491213486E+00	.4727278351784E+00	-.2980021728443E+00	0.
88	0.	.1772349115154E-17	.3937847912312E+00	-.2906956834888E+00	0.
89	0.	.1980168237686E+00	.3609513640404E+00	-.2846010625362E+00	0.
90	0.	.4201654195786E+00	.3437124401331E+00	-.2663204967976E+00	0.
91	0.	.5461454391479E+00	.327012271444E+00	-.2437124401331E+00	0.
92	1.	-.0419267267305E-16	.5877855420113E+00	-.2437124401331E+00	0.
93	1.	.1340278238058E+00	.5836555957794E+00	-.2284601062536E+00	5.
94	1.	.1570491213486E+00	.4727278351784E+00	-.2154490262270E+00	0.
95	1.	.1772349115154E-17	.3937847912312E+00	-.1980168237686E+00	0.
96	0.	.1980168237686E+00	.377012271444E+00	-.188116222446E+00	0.
97	0.	.4201654195786E+00	.3609513640404E+00	-.1728696165154E+00	0.
98	0.	.5461454391479E+00	.3437124401331E+00	-.1674375008600E-16	0.
99	0.	.6594369411469E+00	.327012271444E+00	-.1570491213486E+00	0.
100	0.	-.0419267267305E-17	.5877855420113E+00	-.1431921869516E+00	0.
101	0.	.1340278238058E+00	.5836555957794E+00	-.1340278238058E+00	0.
102	0.	.1570491213486E+00	.4727278351784E+00	-.1227853149176E+00	0.
103	1.	.1772349115154E-17	.3937847912312E+00	-.116222446E+00	5.
104	0.	.1980168237686E+00	.377012271444E+00	-.1069516E+00	0.
105	0.	.4201654195786E+00	.3609513640404E+00	-.969565709E+00	0.
106	0.	.5461454391479E+00	.3437124401331E+00	-.88116222446E+00	0.
107	0.	.6594369411469E+00	.327012271444E+00	-.8008636832237E+00	0.
108	0.	-.0419267267305E-16	.5877855420113E+00	-.7017562985420E+00	0.
109	1.	.1340278238058E+00	.5836555957794E+00	-.6090168237686E+00	5.
110	0.	.1570491213486E+00	.4727278351784E+00	-.5090168237686E+00	0.
111	0.	.1772349115154E-17	.3937847912312E+00	-.4090168237686E+00	0.
112	0.	.1980168237686E+00	.377012271444E+00	-.3090168237686E+00	0.
113	0.	.4201654195786E+00	.3609513640404E+00	-.2090168237686E+00	0.
114	0.	.5461454391479E+00	.3437124401331E+00	-.1090168237686E+00	0.

114	0.	.6857857704163E+00	.6857857704163E+00	.2437124401331E+00	0.
115	1.	.8912064697266E+00	.8912064697266E+00	.45392006090854E+00	5.
116	0.	.8811628222466E+00	.8811628222466E+00	.4506085813046E+00	0.
117	0.	.8520765900612E+00	.8520765900612E+00	.4392809569836E+00	0.
118	0.	.8043146729469E+00	.8043146729469E+00	.4201654195786E+00	0.
119	0.	.7393637299538E+00	.7393637299538E+00	.3937847912312E+00	0.
120	0.	.6594369411469E+00	.6594369411469E+00	.3609513640404E+00	0.
121	1.	-.3545041002901E-16	.8090168237686E+00	.5877855420113E+00	5.
122	0.	.1340278238058E+00	.8008636832237E+00	.5836555957794E+00	0.
123	0.	.2863204967976E+00	.7775039076805E+00	.5697026252747E+00	0.
124	0.	.3257847912312E+00	.7393637299538E+00	.5461454391479E+00	0.
125	0.	.5135421156883E+00	.6874219775200E+00	.5135421156883E+00	0.
126	0.	.6231085062027E+00	.6231085062027E+00	.4727278351784E+00	0.
127	2.	.8290168237686E+00	.4211630207073E-17	-.5877854824066E+00	6.
128	0.	.6008636832237E+00	.1340278238058E+00	-.5836555957794E+00	0.
129	0.	.7775039076805E+00	.2663204967976E+00	-.5697026252747E+00	0.
130	0.	.7393637299538E+00	.3937847912312E+00	-.5461454391479E+00	0.
131	0.	.6594369411469E+00	.5135421156883E+00	-.5135421752930E+00	0.
132	2.	.8047658708374E-16	.8047658708374E-16	-.4539906382561E+00	6.
133	0.	.8811628222466E+00	.1431921720505E+00	-.4506085515022E+00	0.
134	0.	.8520765900612E+00	.2846010625382E+00	-.4392809569836E+00	0.
135	0.	.8043146729469E+00	.4201653897762E+00	-.4201653897762E+00	0.
136	0.	.7393637299538E+00	.5461454391479E+00	-.3937848210335E+00	0.
137	1.	.6857857704163E+00	-.8047658708374E-16	-.3090169237686E+00	6.
138	0.	.8912064697266E+00	.1500601023436E+00	-.3061736882410E+00	0.
139	0.	.8811628222466E+00	.2980022438420E+00	-.2980022132397E+00	0.
140	0.	.8520765900612E+00	.4392809569836E+00	-.2846010322733E+00	0.
141	0.	.8043146729469E+00	.5697026252747E+00	-.2663204667976E+00	0.
142	0.	.7393637299538E+00	-.4211630207073E-16	-.1564417889524E+00	6.
143	0.	.6594369411469E+00	.1544903069735E+00	-.1544902622700E+00	0.
144	0.	.5135421156883E+00	.3061736882410E+00	-.1500600876471E+00	0.
145	0.	.4201653897762E+00	.4506085813046E+00	-.1431921401480E+00	0.
146	0.	.3937847912312E+00	.5836555957794E+00	-.1340277792380E+00	0.
147	1.	.6857857704163E+00	.1000000000000E+00	.0000000000000E+00	5.
148	0.	.8912064697266E+00	.1564841131547E+00	-.4317278460884E+00	0.
149	0.	.8811628222466E+00	.3091199538713E+00	-.17036206168854E+00	0.
150	0.	.8520765900612E+00	.4339916630584E+00	-.6748750082108E+00	0.
151	0.	.8043146729469E+00	.5697026252747E+00	-.3439267126736E+00	0.
152	1.	.6857857704163E+00	.14387470889930E-17	.1564841131547E+00	6.
153	0.	.8043146729469E+00	.1544903069735E+00	.1544903069735E+00	0.
154	0.	.7393637299538E+00	.3061736882410E+00	.1500601023436E+00	0.
155	0.	.6594369411469E+00	.4506085813046E+00	.1431921669515E+00	0.
156	0.	.5135421156883E+00	.5836555957794E+00	.1340276238058E+00	0.
157	2.	.8090168237686E+00	.6570891117555E-16	.3090169535709E+00	6.
158	0.	.8043146729469E+00	.1500601023436E+00	.3061736882410E+00	0.
159	0.	.7393637299538E+00	.2980022728441E+00	.2980022728441E+00	0.
160	0.	.6594369411469E+00	.4392809569836E+00	.2846010625382E+00	0.
161	0.	.5135421156883E+00	.5697026252747E+00	.2663204967976E+00	0.
162	1.	.6857857704163E+00	-.6570891117555E-16	.4539906680561E+00	6.
163	0.	.8912064697266E+00	.1431921669515E+00	.4506085813046E+00	0.
164	0.	.8811628222466E+00	.2846010625382E+00	.4392809569836E+00	0.
165	0.	.8520765900612E+00	.4201654195786E+00	.4201654195786E+00	0.
166	0.	.8043146729469E+00	.5461454391479E+00	.3937847912312E+00	0.
167	2.	.8090168237686E+00	-.3545041002901E-16	.5877855420113E+00	6.
168	0.	.8043146729469E+00	.1340278238058E+00	.5836555957794E+00	0.
169	0.	.7775039076805E+00	.2663204967976E+00	.5697026252747E+00	0.
170	0.	.7393637299538E+00	.3937847912312E+00	.5461454391479E+00	0.
171	0.	.6874219775200E+00	.5135421156883E+00	.5135421156883E+00	0.

1	1	1	7	8	2
2.000E-02	2.000E-02	2.000E-02	2.000E-02		
2	1	2	6	9	3
2.000E-02	2.000E-02	2.000E-02	2.000E-02		
3	1	3	9	10	4
2.000E-02	2.000E-02	2.000E-02	2.000E-02		
4	1	4	10	11	5
2.000E-02	2.000E-02	2.000E-02	2.000E-02		
5	1	5	11	12	6
2.000E-02	2.000E-02	2.000E-02	2.000E-02		



40	1	53	59	60	54
2.000E-02	2.000E-02	2.000E-02	2.000E-02	2.000E-02	
41	1	55	61	62	56
2.000E-02	2.000E-02	2.000E-02	2.000E-02	2.000E-02	
42	1	56	62	63	57
2.000E-02	2.000E-02	2.000E-02	2.000E-02	2.000E-02	
43	1	57	63	64	58
2.000E-02	2.000E-02	2.000E-02	2.000E-02	2.000E-02	
44	1	58	64	65	59
2.000E-02	2.000E-02	2.000E-02	2.000E-02	2.000E-02	
45	1	59	65	66	60
2.000E-02	2.000E-02	2.000E-02	2.000E-02	2.000E-02	
46	1	61	67	68	62
2.000E-02	2.000E-02	2.000E-02	2.000E-02	2.000E-02	
47	1	62	68	69	63
2.000E-02	2.000E-02	2.000E-02	2.000E-02	2.000E-02	
48	1	63	69	70	64
2.000E-02	2.000E-02	2.000E-02	2.000E-02	2.000E-02	
49	1	64	70	71	65
2.000E-02	2.000E-02	2.000E-02	2.000E-02	2.000E-02	
50	1	65	71	72	66
2.000E-02	2.000E-02	2.000E-02	2.000E-02	2.000E-02	
51	1	73	73	74	32
2.000E-02	2.000E-02	2.000E-02	2.000E-02	2.000E-02	
52	1	74	74	75	33
2.000E-02	2.000E-02	2.000E-02	2.000E-02	2.000E-02	
53	1	75	75	76	34
2.000E-02	2.000E-02	2.000E-02	2.000E-02	2.000E-02	
54	1	76	76	77	35
2.000E-02	2.000E-02	2.000E-02	2.000E-02	2.000E-02	
55	1	77	77	78	36
2.000E-02	2.000E-02	2.000E-02	2.000E-02	2.000E-02	
56	1	78	78	79	74
2.000E-02	2.000E-02	2.000E-02	2.000E-02	2.000E-02	
57	1	79	79	80	75
2.000E-02	2.000E-02	2.000E-02	2.000E-02	2.000E-02	
58	1	80	80	81	76
2.000E-02	2.000E-02	2.000E-02	2.000E-02	2.000E-02	
59	1	81	81	82	77
2.000E-02	2.000E-02	2.000E-02	2.000E-02	2.000E-02	
60	1	82	82	83	78
2.000E-02	2.000E-02	2.000E-02	2.000E-02	2.000E-02	
61	1	83	83	84	80
2.000E-02	2.000E-02	2.000E-02	2.000E-02	2.000E-02	
62	1	84	84	85	81
2.000E-02	2.000E-02	2.000E-02	2.000E-02	2.000E-02	
63	1	85	85	86	82
2.000E-02	2.000E-02	2.000E-02	2.000E-02	2.000E-02	
64	1	86	86	87	83
2.000E-02	2.000E-02	2.000E-02	2.000E-02	2.000E-02	
65	1	87	87	88	84
2.000E-02	2.000E-02	2.000E-02	2.000E-02	2.000E-02	
66	1	88	88	89	85
2.000E-02	2.000E-02	2.000E-02	2.000E-02	2.000E-02	
67	1	89	89	90	86
2.000E-02	2.000E-02	2.000E-02	2.000E-02	2.000E-02	
68	1	90	90	91	87
2.000E-02	2.000E-02	2.000E-02	2.000E-02	2.000E-02	
69	1	91	91	92	88
2.000E-02	2.000E-02	2.000E-02	2.000E-02	2.000E-02	
70	1	92	92	93	89
2.000E-02	2.000E-02	2.000E-02	2.000E-02	2.000E-02	
71	1	93	93	94	90
2.000E-02	2.000E-02	2.000E-02	2.000E-02	2.000E-02	
72	1	94	94	95	91
2.000E-02	2.000E-02	2.000E-02	2.000E-02	2.000E-02	
73	1	95	95	96	92
2.000E-02	2.000E-02	2.000E-02	2.000E-02	2.000E-02	
74	1	96	96	97	93
2.000E-02	2.000E-02	2.000E-02	2.000E-02	2.000E-02	
75	1	97	97	98	94
2.000E-02	2.000E-02	2.000E-02	2.000E-02	2.000E-02	
76	1	98	98	99	
2.000E-02	2.000E-02	2.000E-02	2.000E-02	2.000E-02	
77	1	99	99	100	
2.000E-02	2.000E-02	2.000E-02	2.000E-02	2.000E-02	

74	1	94	100	101	95
2.000E-02	2.000E-02	2.000E-02	2.000E-02	2.000E-02	
75	1	95	101	102	96
2.000E-02	2.000E-02	2.000E-02	2.000E-02	2.000E-02	
76	1	97	103	104	98
2.000E-02	2.000E-02	2.000E-02	2.000E-02	2.000E-02	
77	1	98	104	105	99
2.000E-02	2.000E-02	2.000E-02	2.000E-02	2.000E-02	
78	1	99	105	106	100
2.000E-02	2.000E-02	2.000E-02	2.000E-02	2.000E-02	
79	1	100	106	107	101
2.000E-02	2.000E-02	2.000E-02	2.000E-02	2.000E-02	
80	1	101	107	108	102
2.000E-02	2.000E-02	2.000E-02	2.000E-02	2.000E-02	
81	1	103	109	110	104
2.000E-02	2.000E-02	2.000E-02	2.000E-02	2.000E-02	
82	1	104	110	111	105
2.000E-02	2.000E-02	2.000E-02	2.000E-02	2.000E-02	
83	1	105	111	112	106
2.000E-02	2.000E-02	2.000E-02	2.000E-02	2.000E-02	
84	1	106	112	113	107
2.000E-02	2.000E-02	2.000E-02	2.000E-02	2.000E-02	
85	1	107	113	114	108
2.000E-02	2.000E-02	2.000E-02	2.000E-02	2.000E-02	
86	1	108	115	116	109
2.000E-02	2.000E-02	2.000E-02	2.000E-02	2.000E-02	
87	1	110	116	117	111
2.000E-02	2.000E-02	2.000E-02	2.000E-02	2.000E-02	
88	1	111	117	118	112
2.000E-02	2.000E-02	2.000E-02	2.000E-02	2.000E-02	
89	1	112	118	119	113
2.000E-02	2.000E-02	2.000E-02	2.000E-02	2.000E-02	
90	1	113	119	120	114
2.000E-02	2.000E-02	2.000E-02	2.000E-02	2.000E-02	
91	1	115	121	122	116
2.000E-02	2.000E-02	2.000E-02	2.000E-02	2.000E-02	
92	1	116	122	123	117
2.000E-02	2.000E-02	2.000E-02	2.000E-02	2.000E-02	
93	1	117	123	124	118
2.000E-02	2.000E-02	2.000E-02	2.000E-02	2.000E-02	
94	1	118	124	125	119
2.000E-02	2.000E-02	2.000E-02	2.000E-02	2.000E-02	
95	1	119	125	126	120
2.000E-02	2.000E-02	2.000E-02	2.000E-02	2.000E-02	
96	1	121	127	128	122
2.000E-02	2.000E-02	2.000E-02	2.000E-02	2.000E-02	
97	1	122	128	129	123
2.000E-02	2.000E-02	2.000E-02	2.000E-02	2.000E-02	
98	1	123	129	130	124
2.000E-02	2.000E-02	2.000E-02	2.000E-02	2.000E-02	
99	1	124	130	131	125
2.000E-02	2.000E-02	2.000E-02	2.000E-02	2.000E-02	
100	1	125	131	132	126
2.000E-02	2.000E-02	2.000E-02	2.000E-02	2.000E-02	
101	1	127	133	134	128
2.000E-02	2.000E-02	2.000E-02	2.000E-02	2.000E-02	
102	1	128	134	135	129
2.000E-02	2.000E-02	2.000E-02	2.000E-02	2.000E-02	
103	1	129	135	136	130
2.000E-02	2.000E-02	2.000E-02	2.000E-02	2.000E-02	
104	1	130	136	137	131
2.000E-02	2.000E-02	2.000E-02	2.000E-02	2.000E-02	
105	1	131	137	138	132
2.000E-02	2.000E-02	2.000E-02	2.000E-02	2.000E-02	
106	1	132	138	139	133
2.000E-02	2.000E-02	2.000E-02	2.000E-02	2.000E-02	
107	1	133	139	140	134
2.000E-02	2.000E-02	2.000E-02	2.000E-02	2.000E-02	
108	1	134	140	141	135
2.000E-02	2.000E-02	2.000E-02	2.000E-02	2.000E-02	



108	1	129	134	135	130
2.000E-02	2.000E-02	2.000E-02	2.000E-02	2.000E-02	
109	1	130	135	136	131
2.000E-02	2.000E-02	2.000E-02	2.000E-02	2.000E-02	
110	1	131	136	84	79
2.000E-02	2.000E-02	2.000E-02	2.000E-02	2.000E-02	
111	1	132	137	138	133
2.000E-02	2.000E-02	2.000E-02	2.000E-02	2.000E-02	
112	1	133	138	139	134
2.000E-02	2.000E-02	2.000E-02	2.000E-02	2.000E-02	
113	1	134	139	140	135
2.000E-02	2.000E-02	2.000E-02	2.000E-02	2.000E-02	
114	1	135	140	141	136
2.000E-02	2.000E-02	2.000E-02	2.000E-02	2.000E-02	
115	1	136	141	90	84
2.000E-02	2.000E-02	2.000E-02	2.000E-02	2.000E-02	
116	1	137	142	143	138
2.000E-02	2.000E-02	2.000E-02	2.000E-02	2.000E-02	
117	1	138	143	144	139
2.000E-02	2.000E-02	2.000E-02	2.000E-02	2.000E-02	
118	1	139	144	145	140
2.000E-02	2.000E-02	2.000E-02	2.000E-02	2.000E-02	
119	1	140	145	146	141
2.000E-02	2.000E-02	2.000E-02	2.000E-02	2.000E-02	
120	1	141	146	96	90
2.000E-02	2.000E-02	2.000E-02	2.000E-02	2.000E-02	
121	1	142	147	148	143
2.000E-02	2.000E-02	2.000E-02	2.000E-02	2.000E-02	
122	1	143	148	149	144
2.000E-02	2.000E-02	2.000E-02	2.000E-02	2.000E-02	
123	1	144	149	150	145
2.000E-02	2.000E-02	2.000E-02	2.000E-02	2.000E-02	
124	1	145	150	151	146
2.000E-02	2.000E-02	2.000E-02	2.000E-02	2.000E-02	
125	1	146	151	102	96
2.000E-02	2.000E-02	2.000E-02	2.000E-02	2.000E-02	
126	1	147	152	153	148
2.000E-02	2.000E-02	2.000E-02	2.000E-02	2.000E-02	
127	1	148	153	154	149
2.000E-02	2.000E-02	2.000E-02	2.000E-02	2.000E-02	
128	1	149	154	155	150
2.000E-02	2.000E-02	2.000E-02	2.000E-02	2.000E-02	
129	1	150	155	156	151
2.000E-02	2.000E-02	2.000E-02	2.000E-02	2.000E-02	
130	1	151	156	103	102
2.000E-02	2.000E-02	2.000E-02	2.000E-02	2.000E-02	
131	1	152	157	158	153
2.000E-02	2.000E-02	2.000E-02	2.000E-02	2.000E-02	
132	1	153	158	159	154
2.000E-02	2.000E-02	2.000E-02	2.000E-02	2.000E-02	
133	1	154	159	160	155
2.000E-02	2.000E-02	2.000E-02	2.000E-02	2.000E-02	
134	1	155	160	161	156
2.000E-02	2.000E-02	2.000E-02	2.000E-02	2.000E-02	
135	1	156	161	114	108
2.000E-02	2.000E-02	2.000E-02	2.000E-02	2.000E-02	
136	1	157	162	163	158
2.000E-02	2.000E-02	2.000E-02	2.000E-02	2.000E-02	
137	1	158	163	164	159
2.000E-02	2.000E-02	2.000E-02	2.000E-02	2.000E-02	
138	1	159	164	165	160
2.000E-02	2.000E-02	2.000E-02	2.000E-02	2.000E-02	
139	1	160	165	166	161
2.000E-02	2.000E-02	2.000E-02	2.000E-02	2.000E-02	
140	1	161	166	120	114
2.000E-02	2.000E-02	2.000E-02	2.000E-02	2.000E-02	
141	1	162	167	168	162
2.000E-02	2.000E-02	2.000E-02	2.000E-02	2.000E-02	



1	63	57	54	64-1.000E+00-1.000E+00-1.000E+00-1.000E+00
1	68	63	64	70-1.000E+00-1.000E+00-1.000E+00-1.000E+00
1	46	40	41	47-1.000E+00-1.000E+00-1.000E+00-1.000E+00
1	52	46	47	53-1.000E+00-1.000E+00-1.000E+00-1.000E+00
1	53	50	53	59-1.000E+00-1.000E+00-1.000E+00-1.000E+00
1	64	58	59	65-1.000E+00-1.000E+00-1.000E+00-1.000E+00
1	70	64	65	71-1.000E+00-1.000E+00-1.000E+00-1.000E+00
1	47	41	41	48-1.000E+00-1.000E+00-1.000E+00-1.000E+00
1	55	47	48	54-1.000E+00-1.000E+00-1.000E+00-1.000E+00
1	59	55	54	60-1.000E+00-1.000E+00-1.000E+00-1.000E+00
1	65	59	60	66-1.000E+00-1.000E+00-1.000E+00-1.000E+00
1	71	65	66	72-1.000E+00-1.000E+00-1.000E+00-1.000E+00
1	31	23	24	32-1.000E+00-1.000E+00-1.000E+00-1.000E+00
1	73	79	80	74-1.000E+00-1.000E+00-1.000E+00-1.000E+00
1	79	85	86	80-1.000E+00-1.000E+00-1.000E+00-1.000E+00
1	85	91	92	86-1.000E+00-1.000E+00-1.000E+00-1.000E+00
1	91	97	98	92-1.000E+00-1.000E+00-1.000E+00-1.000E+00
1	97	103	104	98-1.000E+00-1.000E+00-1.000E+00-1.000E+00
1	103	109	110	104-1.000E+00-1.000E+00-1.000E+00-1.000E+00
1	109	115	115	110-1.000E+00-1.000E+00-1.000E+00-1.000E+00
1	115	121	122	116-1.000E+00-1.000E+00-1.000E+00-1.000E+00
1	121	127	128	122-1.000E+00-1.000E+00-1.000E+00-1.000E+00
1	127	133	134	128-1.000E+00-1.000E+00-1.000E+00-1.000E+00
1	133	139	140	134-1.000E+00-1.000E+00-1.000E+00-1.000E+00
1	139	145	146	140-1.000E+00-1.000E+00-1.000E+00-1.000E+00
1	145	151	152	146-1.000E+00-1.000E+00-1.000E+00-1.000E+00
1	151	157	158	152-1.000E+00-1.000E+00-1.000E+00-1.000E+00
1	157	163	164	158-1.000E+00-1.000E+00-1.000E+00-1.000E+00
1	163	169	170	164-1.000E+00-1.000E+00-1.000E+00-1.000E+00
1	169	175	176	170-1.000E+00-1.000E+00-1.000E+00-1.000E+00
1	175	181	182	176-1.000E+00-1.000E+00-1.000E+00-1.000E+00
1	181	187	188	182-1.000E+00-1.000E+00-1.000E+00-1.000E+00
1	187	193	194	188-1.000E+00-1.000E+00-1.000E+00-1.000E+00
1	193	199	200	194-1.000E+00-1.000E+00-1.000E+00-1.000E+00
1	199	205	206	200-1.000E+00-1.000E+00-1.000E+00-1.000E+00
1	205	211	212	206-1.000E+00-1.000E+00-1.000E+00-1.000E+00
1	211	217	218	212-1.000E+00-1.000E+00-1.000E+00-1.000E+00
1	217	223	224	218-1.000E+00-1.000E+00-1.000E+00-1.000E+00
1	223	229	230	224-1.000E+00-1.000E+00-1.000E+00-1.000E+00
1	229	235	236	230-1.000E+00-1.000E+00-1.000E+00-1.000E+00
1	235	241	242	236-1.000E+00-1.000E+00-1.000E+00-1.000E+00
1	241	247	248	242-1.000E+00-1.000E+00-1.000E+00-1.000E+00
1	247	253	254	248-1.000E+00-1.000E+00-1.000E+00-1.000E+00
1	253	259	260	254-1.000E+00-1.000E+00-1.000E+00-1.000E+00
1	259	265	266	260-1.000E+00-1.000E+00-1.000E+00-1.000E+00
1	265	271	272	266-1.000E+00-1.000E+00-1.000E+00-1.000E+00
1	271	277	278	272-1.000E+00-1.000E+00-1.000E+00-1.000E+00
1	277	283	284	278-1.000E+00-1.000E+00-1.000E+00-1.000E+00
1	283	289	290	284-1.000E+00-1.000E+00-1.000E+00-1.000E+00
1	289	295	296	290-1.000E+00-1.000E+00-1.000E+00-1.000E+00
1	295	301	302	296-1.000E+00-1.000E+00-1.000E+00-1.000E+00
1	301	307	308	302-1.000E+00-1.000E+00-1.000E+00-1.000E+00
1	307	313	314	308-1.000E+00-1.000E+00-1.000E+00-1.000E+00
1	313	319	320	314-1.000E+00-1.000E+00-1.000E+00-1.000E+00
1	319	325	326	320-1.000E+00-1.000E+00-1.000E+00-1.000E+00
1	325	331	332	326-1.000E+00-1.000E+00-1.000E+00-1.000E+00
1	331	337	338	332-1.000E+00-1.000E+00-1.000E+00-1.000E+00
1	337	343	344	338-1.000E+00-1.000E+00-1.000E+00-1.000E+00
1	343	349	350	344-1.000E+00-1.000E+00-1.000E+00-1.000E+00
1	349	355	356	350-1.000E+00-1.000E+00-1.000E+00-1.000E+00
1	355	361	362	356-1.000E+00-1.000E+00-1.000E+00-1.000E+00
1	361	367	368	362-1.000E+00-1.000E+00-1.000E+00-1.000E+00
1	367	373	374	368-1.000E+00-1.000E+00-1.000E+00-1.000E+00
1	373	379	380	374-1.000E+00-1.000E+00-1.000E+00-1.000E+00
1	379	385	386	380-1.000E+00-1.000E+00-1.000E+00-1.000E+00
1	385	391	392	386-1.000E+00-1.000E+00-1.000E+00-1.000E+00
1	391	397	398	392-1.000E+00-1.000E+00-1.000E+00-1.000E+00
1	397	403	404	398-1.000E+00-1.000E+00-1.000E+00-1.000E+00
1	403	409	410	404-1.000E+00-1.000E+00-1.000E+00-1.000E+00
1	409	415	416	410-1.000E+00-1.000E+00-1.000E+00-1.000E+00
1	415	421	422	416-1.000E+00-1.000E+00-1.000E+00-1.000E+00
1	421	427	428	422-1.000E+00-1.000E+00-1.000E+00-1.000E+00
1	427	433	434	428-1.000E+00-1.000E+00-1.000E+00-1.000E+00
1	433	439	440	434-1.000E+00-1.000E+00-1.000E+00-1.000E+00
1	439	445	446	440-1.000E+00-1.000E+00-1.000E+00-1.000E+00
1	445	451	452	446-1.000E+00-1.000E+00-1.000E+00-1.000E+00
1	451	457	458	452-1.000E+00-1.000E+00-1.000E+00-1.000E+00







**C. FLUMAS PRE-PROCESSOR DATA**

```

FLUMAS DATA FOR SPHERICAL SHELL QUARTER MODEL
sph.flu sph.geo sph.nom sph.daa $ FLUNAM GEONAM GRDNAM DAANAM
T T F T $ PRTGMT PRTRN PRTAMF CALCAM
T F F T $ EIGMAF TWODIM HAFMOD QUAMOD
F F T T $ PCHCDS NASTAM STOMAS STOINV
F F F F $ FRWTF L FRWTGE FRWTGR FRESUR
F T F F $ RENUMB STOGMT ROTGEO ROTQUA
F F T F $ PRTCOE STRMAS SPHERE ROTSYM
F F F F $ OCTMOD CAVFLU FRWTFV EFUDGE
DYNA $ MAINKY
0 171 0 150 $ NSTRC NSTRF NGEN NGENF
0 0 0 $ NBRA NCYL NCAV
1. 1. $ RHO CEE
10 $ NVEC
1. 1. 1. 1. $ CQ(1) CQ(2) CQ(3) CQ(4)
1 $ NSRADI
1. 1. 1 150 1 $ RAD1 RAD2 JBEG JEND JINC
0 $ NSORDR
1. $ SPHRAD

```

**D. AUGMAT PRE-PROCESSOR DATA**

AUGMAT DATA FOR SPHERICAL SHELL				QUARTER MODEL
sph.nom	sph.flu	sph.geo	sph.pre	\$ STRNAM FLUNAM GEONAM PRENAM
F F F F				\$ FRWTGE FRWTST FRWTF L PLNWAV
F F T T				\$ FLUSKY DAAFRM SYMCON DOFTAB
F F F T				\$ PRTGMT PRTRN PRTSTF PRTAUG
F F F				\$ MODTRN STRLCL INTWAT
DYNA				\$ MAINKY
1.				\$ DAA2
171	513	3	3	\$ NSTR NSFR NFRE NFTR
1				\$ NSETLC
0	1	150	1	\$ NDICOS JSTART JSTOP JINC
4				\$ NUMCON
1	1	121	6	\$ ICON NSTART NSTOP NINC
2	1	6	1	\$ ICON NSTART NSTOP NINC
2	37	42	1	\$ ICON NSTART NSTOP NINC
2	127	167	5	\$ ICON NSTART NSTOP NINC



**E. TIMINT PRE-PROCESSOR INPUT DATA**

```
TIMINT DATA FOR SPHERICAL SHELL QUARTER MODEL
sph.pre sph.pos $ PRENAM POSNAM
sph.rst         $ RESNAM
0. 0. 10000.   $ XC      YC      ZC
  0. 0. 1.     $ SX      SY      SZ
F F F F       $ EXPWAV SPLINE VARLIN PACKET
F F F F       $ HYPERB BUBPUL REFSEC EXPLOS
2             $ JPHIST
1. 0.        $ PNORM
50.          $ DTHIST
1.E-6 1.E-6  $ PHIST
1 0          $ NTINT  NCHGAL
0. .00025    $ STRTIM DELTIM
1000 1000    $ NSAVER NRESET NSODFL
0 0 0 0     $ LOCBEG LOCRES LOCWRT NSTART
F           $ DISPLA
```

**APPENDIX B - INFINITE CYLINDER VALIDATION INPUT DATA**

**A. INGRID PRE-PROCESSOR INPUT DATA**

INFINITE CYLINDER MODEL

dn3d vec term 5.0 plti 0.01 prti 1000.

mat 1 type 1 e 9.813e+1 pr 0.3 ro 7.85  
shell quad 0 thick 0.010 endmat

lcd 1 2 0.0 0.0 10.0 0.0

lcd 2 2 0.0 0.000025 10.0 0.000025

plan 3

0 0 0 0 -1 0 0.00001 symm  
0 0 -.0005 0 0 -1 0.001 symm  
0 0 .0005 0 0 1 0.001 symm

start

-1 6 -11 ;

-1 6 -11 ;

1 2 ;

-1. 0. 1.

-1. 0. 1.

-.0005 .0005

a 1 1 0 3 3 0 3 1.0

d 0 1 0 0 2 0

pri -1 -3 ; -1 -3 ; ; 1 -1.0 0. 0. 0.

mate 1

end

end



1.000E-02	1.000E-02	1.000E-02	1.000E-02	
3	1	9	10	4
1.000E-02	1.000E-02	1.000E-02	1.000E-02	
4	1	10	11	5
1.000E-02	1.000E-02	1.000E-02	1.000E-02	
5	1	11	12	6
1.000E-02	1.000E-02	1.000E-02	1.000E-02	
6	1	12	13	13
1.000E-02	1.000E-02	1.000E-02	1.000E-02	
7	1	13	14	14
1.000E-02	1.000E-02	1.000E-02	1.000E-02	
8	1	14	15	15
1.000E-02	1.000E-02	1.000E-02	1.000E-02	
9	1	15	16	16
1.000E-02	1.000E-02	1.000E-02	1.000E-02	
10	1	16	17	17
1.000E-02	1.000E-02	1.000E-02	1.000E-02	
11	1	17	18	23
1.000E-02	1.000E-02	1.000E-02	1.000E-02	
12	1	18	19	24
1.000E-02	1.000E-02	1.000E-02	1.000E-02	
13	1	19	20	25
1.000E-02	1.000E-02	1.000E-02	1.000E-02	
14	1	20	21	26
1.000E-02	1.000E-02	1.000E-02	1.000E-02	
15	1	21	22	27
1.000E-02	1.000E-02	1.000E-02	1.000E-02	
16	1	22	23	34
1.000E-02	1.000E-02	1.000E-02	1.000E-02	
17	1	23	24	35
1.000E-02	1.000E-02	1.000E-02	1.000E-02	
18	1	24	25	36
1.000E-02	1.000E-02	1.000E-02	1.000E-02	
19	1	25	26	37
1.000E-02	1.000E-02	1.000E-02	1.000E-02	
20	1	26	27	37
1.000E-02	1.000E-02	1.000E-02	1.000E-02	
21	1	27	28	37

\*----- LEAD CURVE DEFINITIONS -----\*

1	2
0.000E+00	0.000E+00
1.000E+01	0.000E+00
2	3
0.000E+01	0.000E+00
1.000E+01	0.000E+00

\*----- FEATURE BOUNDARY CONDITION CARDS -----\*

1	1	7	8	2-1.000E+00-1.000E+00-1.000E+00-1.000E+00
1	2	8	9	3-1.000E+00-1.000E+00-1.000E+00-1.000E+00
1	3	9	10	4-1.000E+00-1.000E+00-1.000E+00-1.000E+00
1	4	10	11	5-1.000E+00-1.000E+00-1.000E+00-1.000E+00
1	5	11	12	6-1.000E+00-1.000E+00-1.000E+00-1.000E+00
1	6	12	18	13-1.000E+00-1.000E+00-1.000E+00-1.000E+00
1	13	18	19	14-1.000E+00-1.000E+00-1.000E+00-1.000E+00
1	14	19	20	15-1.000E+00-1.000E+00-1.000E+00-1.000E+00
1	15	20	21	16-1.000E+00-1.000E+00-1.000E+00-1.000E+00
1	16	21	22	17-1.000E+00-1.000E+00-1.000E+00-1.000E+00
1	17	22	28	23-1.000E+00-1.000E+00-1.000E+00-1.000E+00
1	23	28	29	24-1.000E+00-1.000E+00-1.000E+00-1.000E+00
1	24	29	30	25-1.000E+00-1.000E+00-1.000E+00-1.000E+00
1	25	30	31	26-1.000E+00-1.000E+00-1.000E+00-1.000E+00
1	26	31	32	27-1.000E+00-1.000E+00-1.000E+00-1.000E+00
1	32	32	34	39-1.000E+00-1.000E+00-1.000E+00-1.000E+00
1	33	34	35	40-1.000E+00-1.000E+00-1.000E+00-1.000E+00
1	34	35	36	41-1.000E+00-1.000E+00-1.000E+00-1.000E+00
1	35	36	37	42-1.000E+00-1.000E+00-1.000E+00-1.000E+00

1	41	37	27	52	-1.000E+00-1.000E+00-1.000E+00-1.000E+00
1					
1					
1					
1					
1					
1					
1	14	14	14	14	
1	14	14	14	14	
1	16	16	16	16	
1	17	17	17	17	
1	23	23	23	23	
1	24	24	24	24	
1	25	25	25	25	
1	38	38	38	38	
1	40	40	40	40	
1	41	41	41	41	
1	42	42	42	42	
1	43	43	43	43	

**C. FLUMAS PRE-PROCESSOR INPUT DATA**

FLUMAS DATA FOR INFINITE CYLINDER MODEL

cyl.flu	cyl.geo	cyl.nom	cyl.daa	\$	FLUNAM	GEONAM	GRDNAM	DAANAM	
T	T	T	T	\$	PRTGMT	PRTRN	PRTAMF	CALCAM	
T	T	T	F	\$	EIGMAF	TWODIM	HAFMOD	QUAMOD	
F	F	T	T	\$	PCHCDS	NASTAM	STOMAS	STOINV	
F	F	F	F	\$	FRWTFL	FRWTGE	FRWTGR	FRESUR	
F	T	F	F	\$	RENUMB	STOGMT	ROTGEO	ROTQUA	
F	F	F	F	\$	PRTCOC	STRMAS	SPHERE	ROTSYM	
F	F	F	F	\$	OCTMOD	CAVFLU	FRWTFV	EFUDGE	
DYNA				\$	MAINKY				
0	42	0	20	\$	NSTRC	NSTRF	NGEN	NGENF	
0	0	0		\$	NBRA	NCYL	NCAV		
1.	1.			\$	RHO	CEE			
10				\$	NVEC				
1.	1.			\$	CQ(1)	CQ(2)			
0.	0.	-1.	0.	\$	DHALF	CXHF	CYHF	CZHF	
1				\$	NSRADI				
0.	1.	1	20	\$	RAD1	RAD2	JBEG	JEND	JINC
1				\$	NSORDR				
1	1	20	1	\$	NORD	JBEG	JEND	JINC	

**D. AUGMAT PRE-PROCESSOR DATA**

```
AUGMAT DATA FOR INFINITE CYLINDER MODEL
cyl.nom cyl.flu cyl.geo cyl.pre $ STRNAM FLUNAM GEONAM PRENAM
F F F F $ FRWTGE FRWTST FRWTF L PLNWAV
F F T T $ FLUSKY DAAFRM SYMCON DOFTAB
T T F T $ PRTGMT PRTRRN PRTSTF PRTAUG
F F F $ MOCTRN STRLCL INTWAT
DYNA $ MAINKY
0.75 $ DAA2
42 126 3 3 $ NSTR NSFR NFRE NFTR
1 $ NSETLC
0 1 20 1 $ NDICOS JSTART JSTOP JINC
2 $ NUMCON
2 1 7 6 $ ICON NSTART NSTOP NINC
2 33 38 5 $ ICON NSTART NSTOP NINC
```



**E. TIMINT PRE-PROCESSOR DATA**

```
TIME INTEGRATION DATA FOR INFINITE CYLINDER MODEL
cyl.pre cyl.pos      $ PRENAM POSNAM
cyl.rst              $ RESNAM
10000.    0.0000    0.0000000 $ XC      YC      ZC
1.0000    0.0000    0.0000000 $ SX      SY      SZ
F F F F          $ EXPWAV SPLINE VARLIN PACKET
F F F F          $ HYPERB BUBPUL REFSEC EXPLOS
2              $ JPHIST
1. 0.          $ PNORM HYDPRE
50.           $ DTHIST
1.e-6 1.e-6    $ PHIST(1) PHIST(2)
1 0           $ NTINT NCHGAL
0. 0.00025    $ STRTIM DELTIM
10000 10000    $ NSAVER NRESET NSODFL
0 0 0 0       $ LOCBEG LOCRES LOCWRT NSTART
F              $ DISPLA
```

**APPENDIX C - UNDEX TEST REPORT**



## DYNAMIC TESTING, INC.

P.O. Box 494 • Rustburg, Virginia 24588-0494 • (804) 846-0244 • Fax (804) 846-2197

DTI-R-TSG  
DTI91-183  
4 September 1991

United States Naval Postgraduate School  
Department of Mechanical Engineering  
Monterey, California 93943-5100

**Attention:** Dr. Young Shin

**Subject:** Cylinder Test Results, DTI Job No. 131

**Enclosure:** (1) Instrumentation Time-Histories, Test No. 1  
(2) Instrumentation Time-Histories, Test No. 2  
(3) Test Photographs  
(4) Data Provided in ASCII Format

Gentlemen:

Dynamic Testing, Inc. (DTI), is pleased to provide the following results for the cylinder tests conducted at our facility on 20 and 22 August 1991.

The first test, conducted on Tuesday, 20 August 1991, using a 60-pound HBX cylindrical charge, consisted of one cylinder oriented for an end-on shot with a 28-foot standoff at a depth of 12 feet. There were a total of 7 strain gauges per axis for a total of 14 strain gauges. One free-field pressure gauge was located 28 feet from the charge, but was positioned in such a way that no reflection from the cylinder occurred. There were three pair of strain gauges located in the center of the cylinder, one at B1, B2, and B3. Two pair of strain gauges were located 4.5 inches from each end oriented at A1, A3, C1, and C3. Before the test it was noted that gauge A1C was not working properly, so we oriented the cylinder so that the end, designated C, was toward the blast (see Figure 1).

The strain gauges were oriented to monitor longitudinal and circumferential strains. Predicted analysis indicated a .2 percent strain at 30 feet. No visual damage was observed.

The second test, conducted Thursday, 22 August 1991, using a 60-pound HBX cylindrical charge, consisted of one cylinder oriented for a side shot with a 25-foot standoff at a depth of 12 feet. There were a total of 7 strain gauges per axis for a total of 14 strain gauges. One free-field pressure gauge was located 25 feet from the charge, and positioned so no reflection from the cylinder occurred. There were three pair of strain gauges located in the center of the cylinder, one at B1, B2, and B3. Two pair of strain gauges were located 4.5 inches from each end oriented at A1, A2, C1, and C2 (see above).

The strain gauges were oriented to monitor longitudinal and circumferential strains. Predicted analysis indicated a .48 percent strain at 25 feet. No visual damage was observed.

Dr. Young Shin  
United States Naval Postgraduate School  
DTI91-183  
4 September 1991  
Page 2

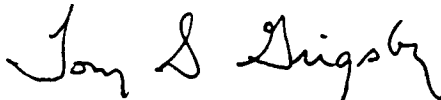
The test configuration consisted of one cylinder being suspended by the crane and one charge suspended from a float (see Figures 2a and 2b for test configurations).

We trust you will find the enclosed satisfactory. It was a pleasure working with you on this project.

If you have any questions or comments, please do not hesitate to contact Mr. Randy Fairfield or the undersigned.

Sincerely,

*DYNAMIC TESTING, INC.*



Tony S. Grigsby  
Instrumentation Technician

TSG:mal

cc: G.G. Amir  
G.D. Snyder  
R.D. Fairfield  
W.G. Lyon

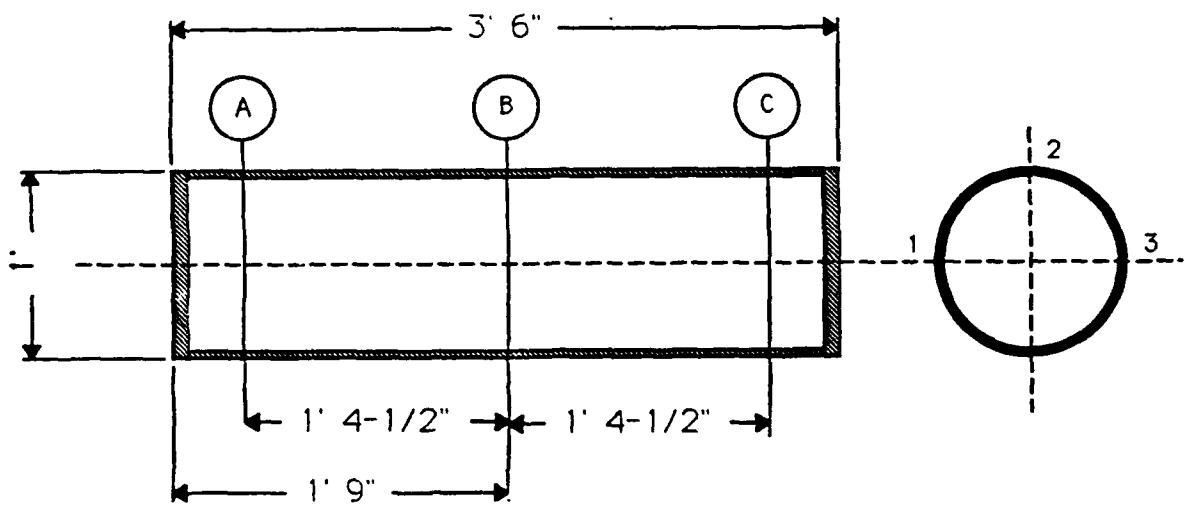


*Figure 1. Cylinder Orientation Prior to Test No. 1*

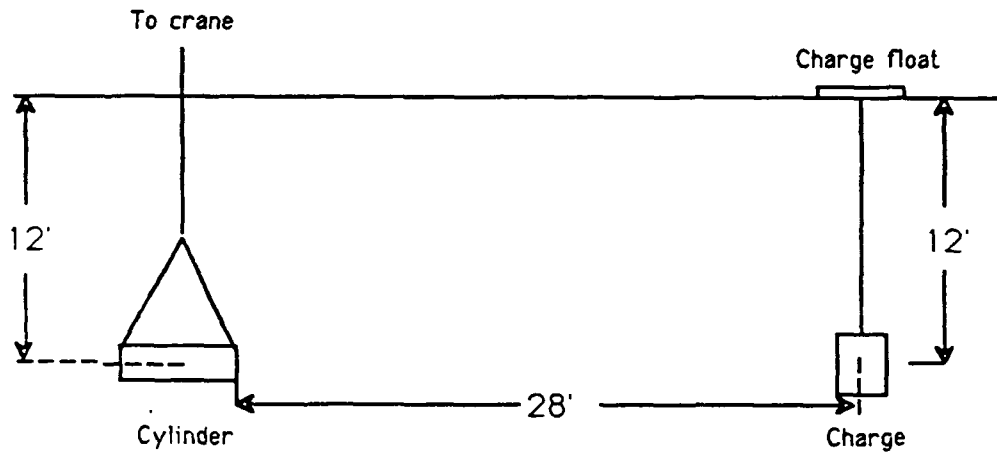


**Figure 2a. Test Configuration for Test No. 1**

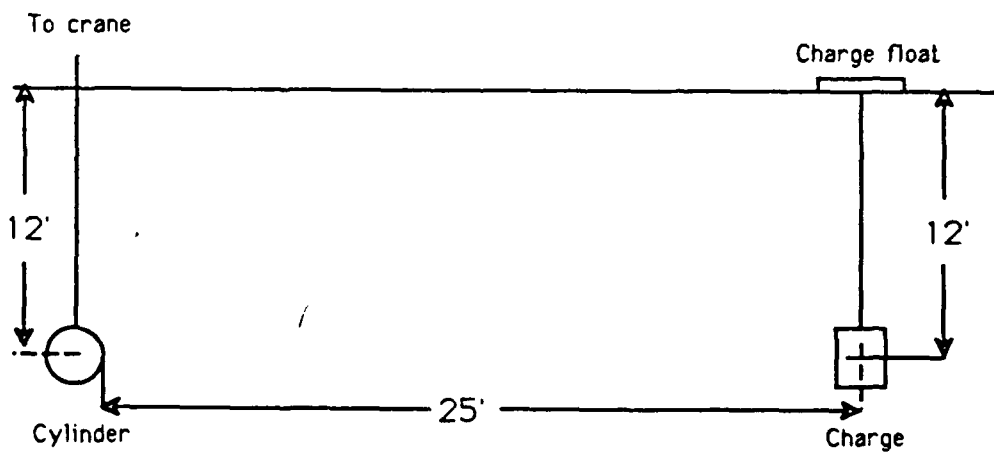


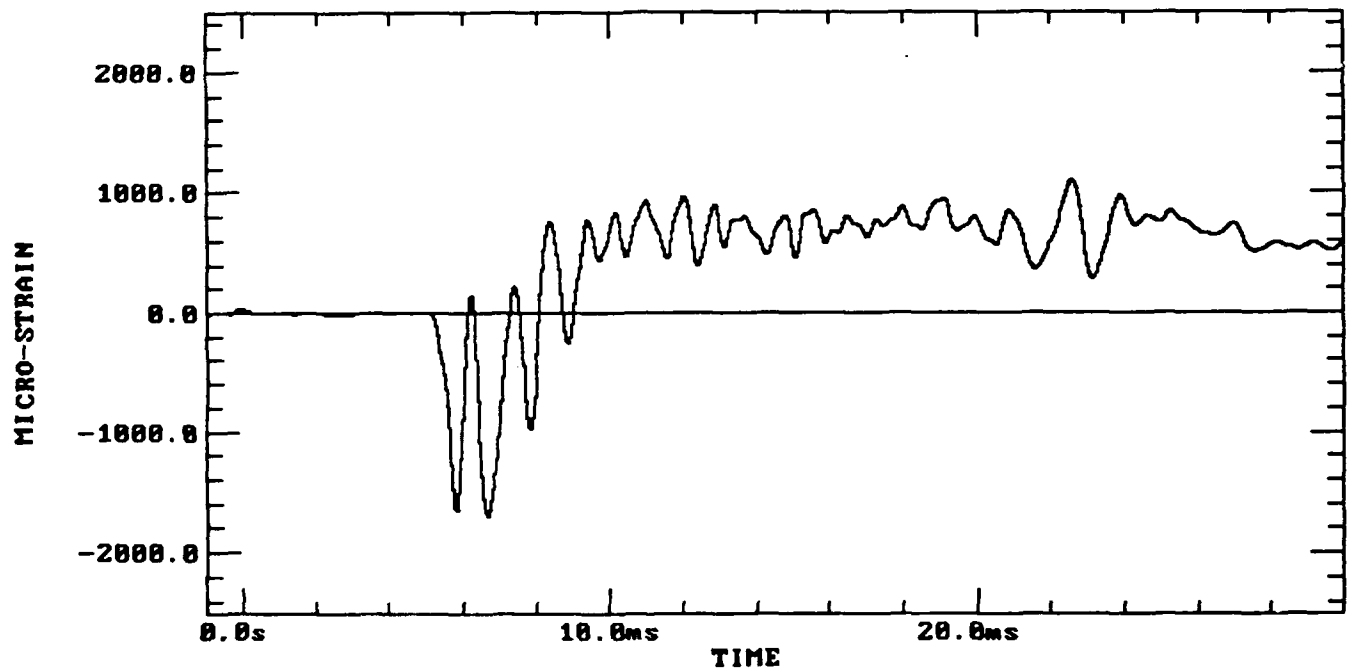
**Figure 2b. Test Configuration for Test No. 2**

*Test No. 1*

# NPS PRECISION UNDEX TESTING

TEST 1

ZERO REPRESENTS DETONATION TIME



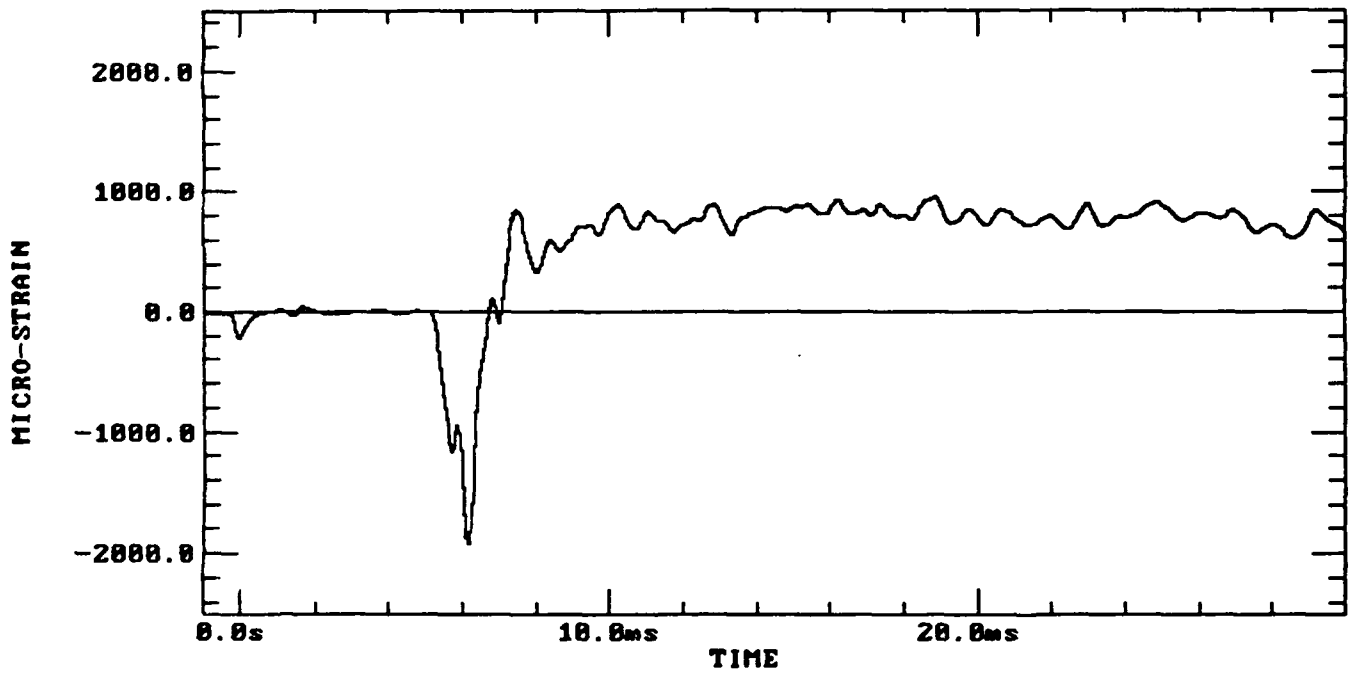
TIME HISTORY OF GAUGE A11  
FILTERED AT 2000 HZ LOW PASS



# NPS PRECISION UNDEX TESTING

TEST 1

ZERO REPRESENTS DETONATION TIME

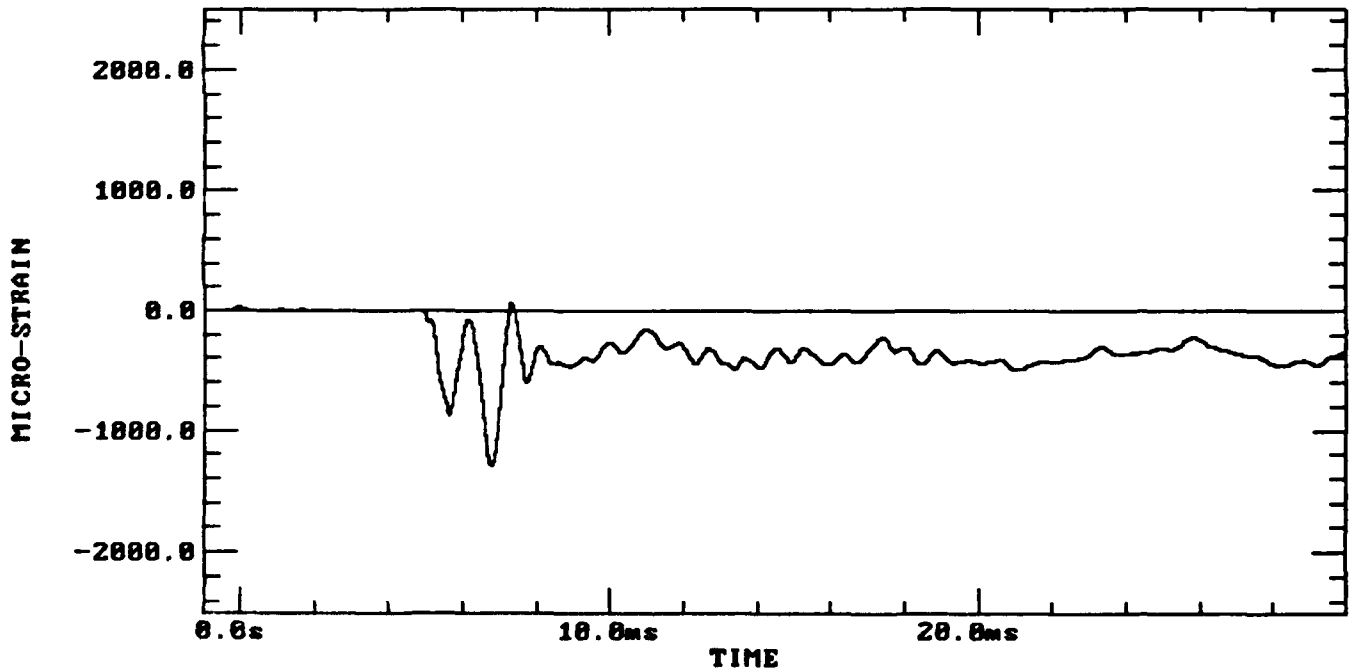


TIME HISTORY OF GAUGE A3L  
FILTERED AT 2000 HZ LOW PASS

# NPS PRECISION UNDEX TESTING

TEST 1

ZERO REPRESENTS DETONATION TIME

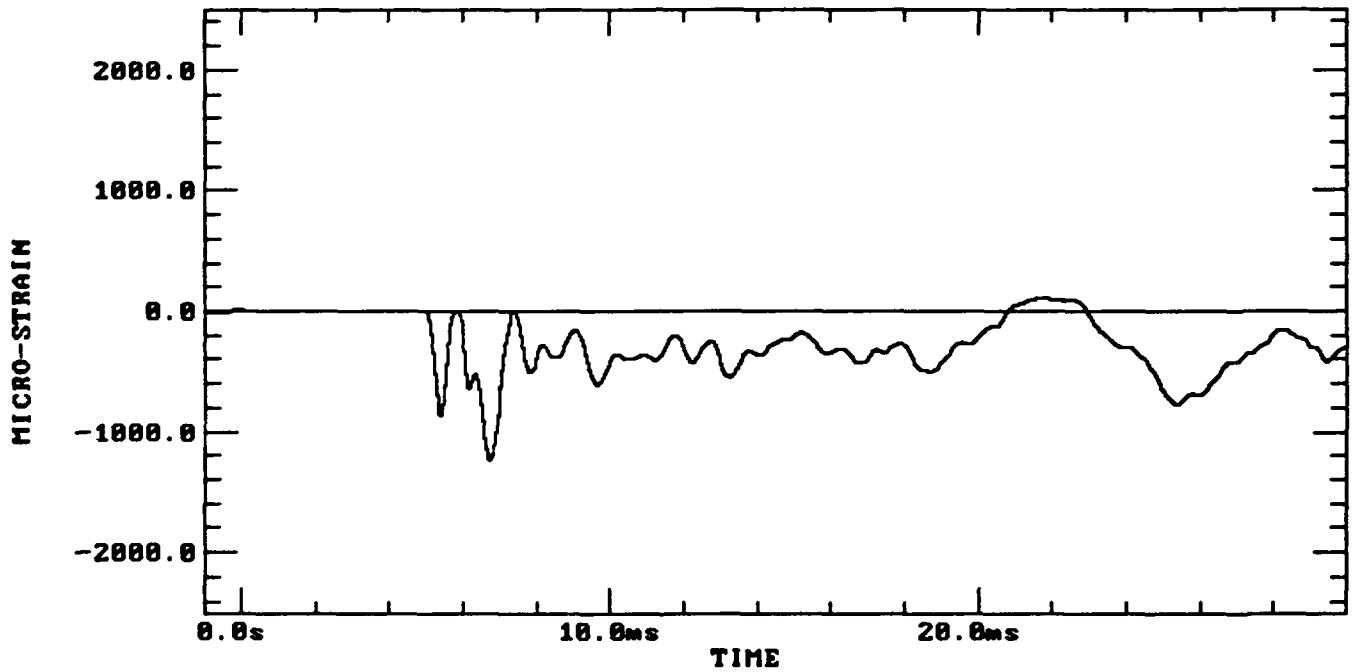


TIME HISTORY OF GAUGE C1L  
FILTERED AT 2000 HZ LOW PASS

# NPS PRECISION UNDEX TESTING

TEST 1

ZERO REPRESENTS DETONATION TIME

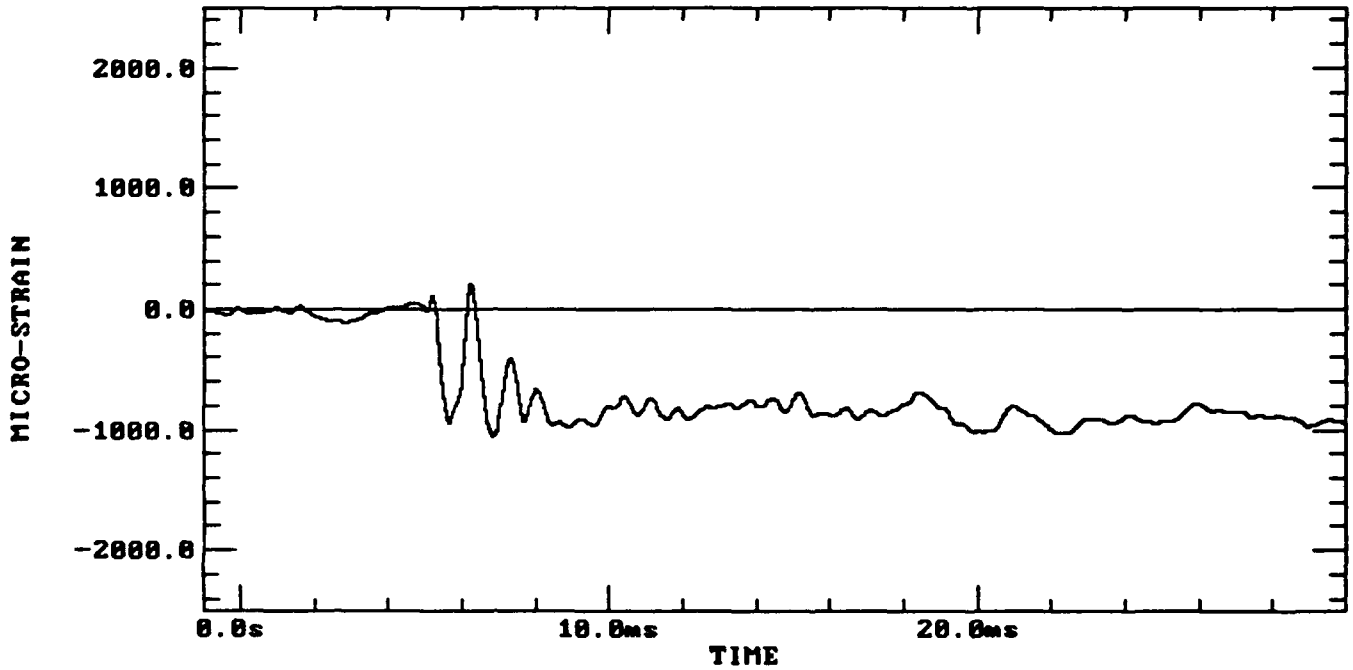


TIME HISTORY OF GAUGE B2L  
FILTERED AT 2000 HZ LOW PASS

# NPS PRECISION UNDEX TESTING

TEST 1

ZERO REPRESENTS DETONATION TIME

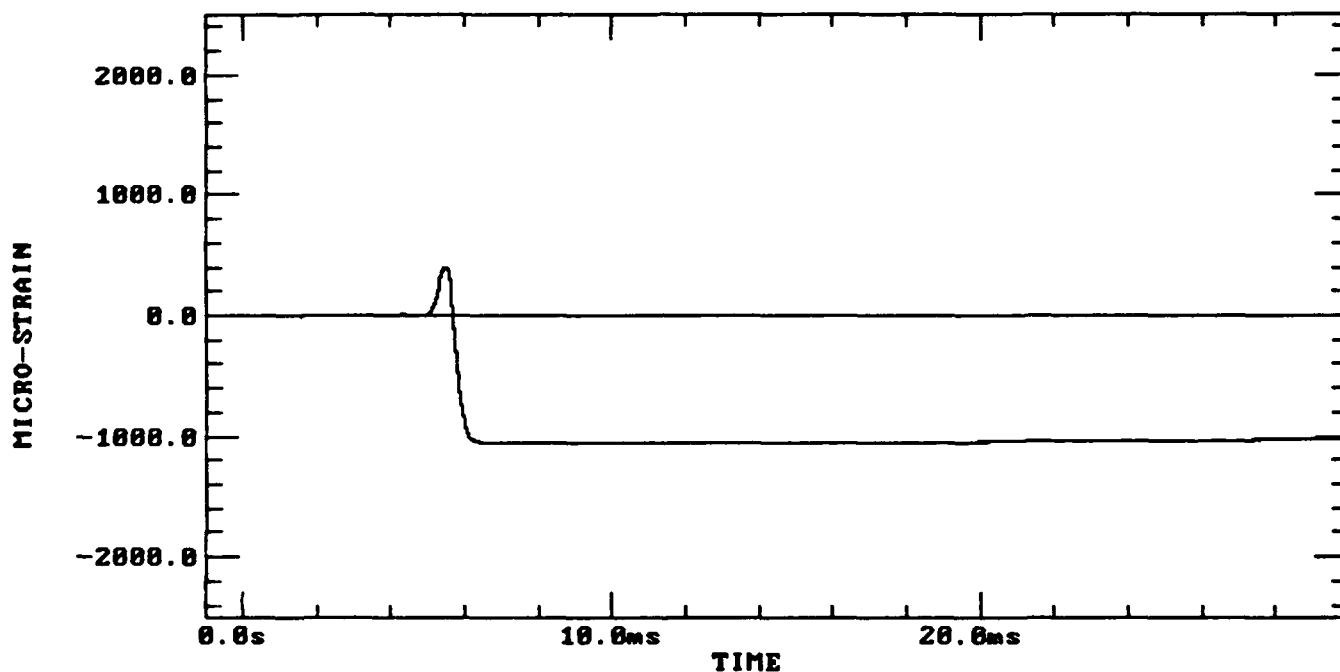


TIME HISTORY OF GAUGE C3L  
FILTERED AT 2000 HZ LOW PASS

# NPS PRECISION UNDEX TESTING

TEST 1

ZERO REPRESENTS DETONATION TIME

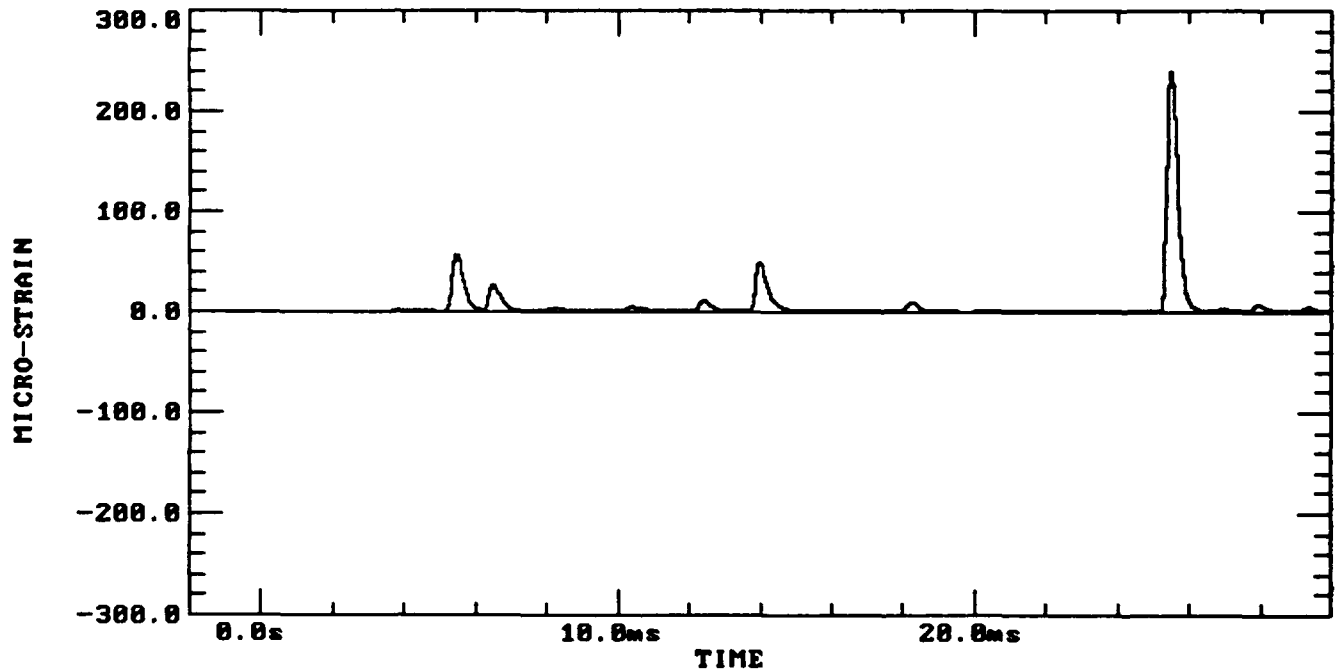


TIME HISTORY OF GAUGE A3C  
FILTERED AT 2000 HZ LOW PASS

# NPS PRECISION UNDEX TESTING

TEST 1

ZERO REPRESENTS DETONATION TIME

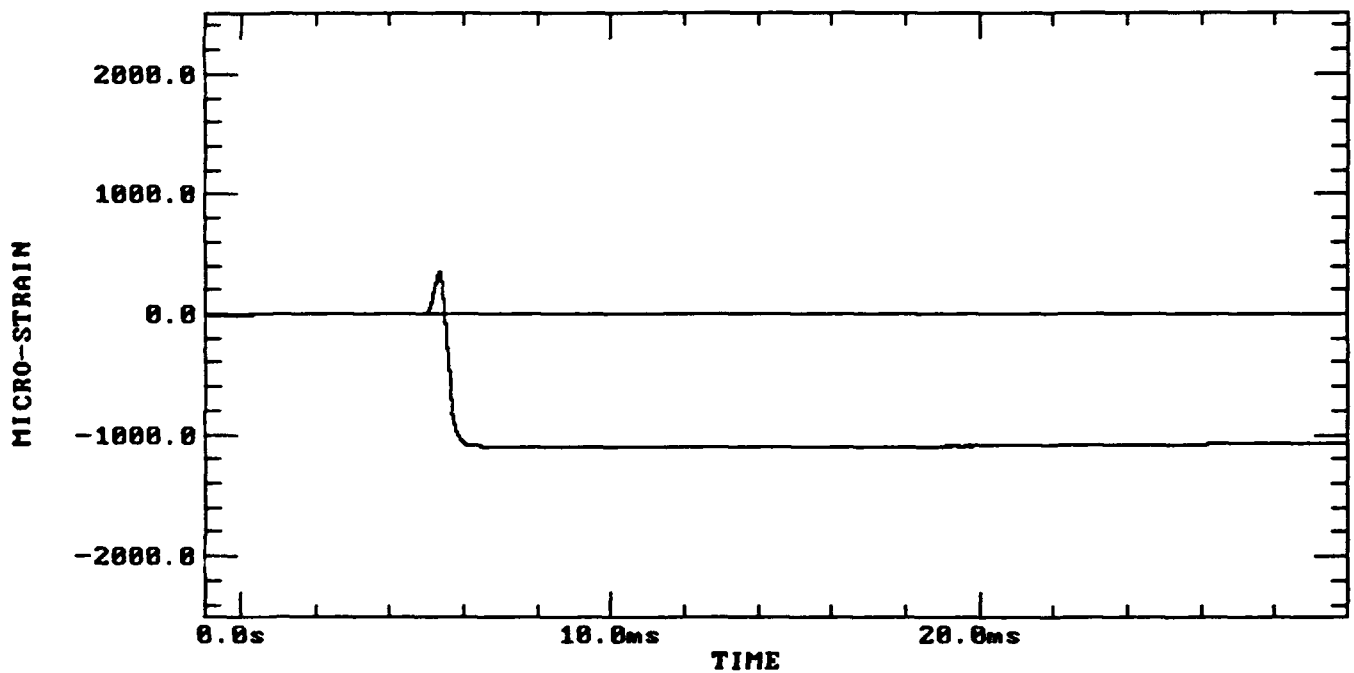


TIME HISTORY OF GAUGE B1C  
FILTERED AT 2000 HZ LOW PASS

# NPS PRECISION UNDEX TESTING

TEST 1

ZERO REPRESENTS DETONATION TIME

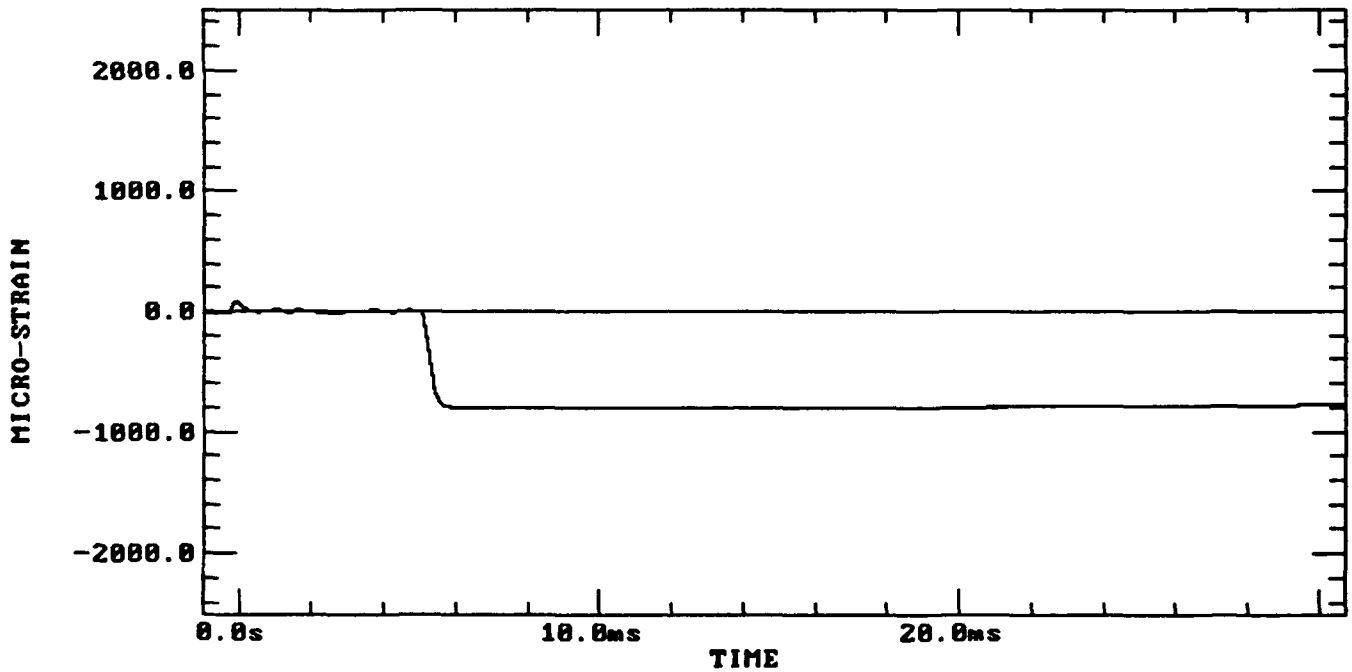


TIME HISTORY OF GAUGE B2C  
FILTERED AT 2000 HZ LOW PASS

# NPS PRECISION UNDEX TESTING

TEST 1

ZERO REPRESENTS DETONATION TIME



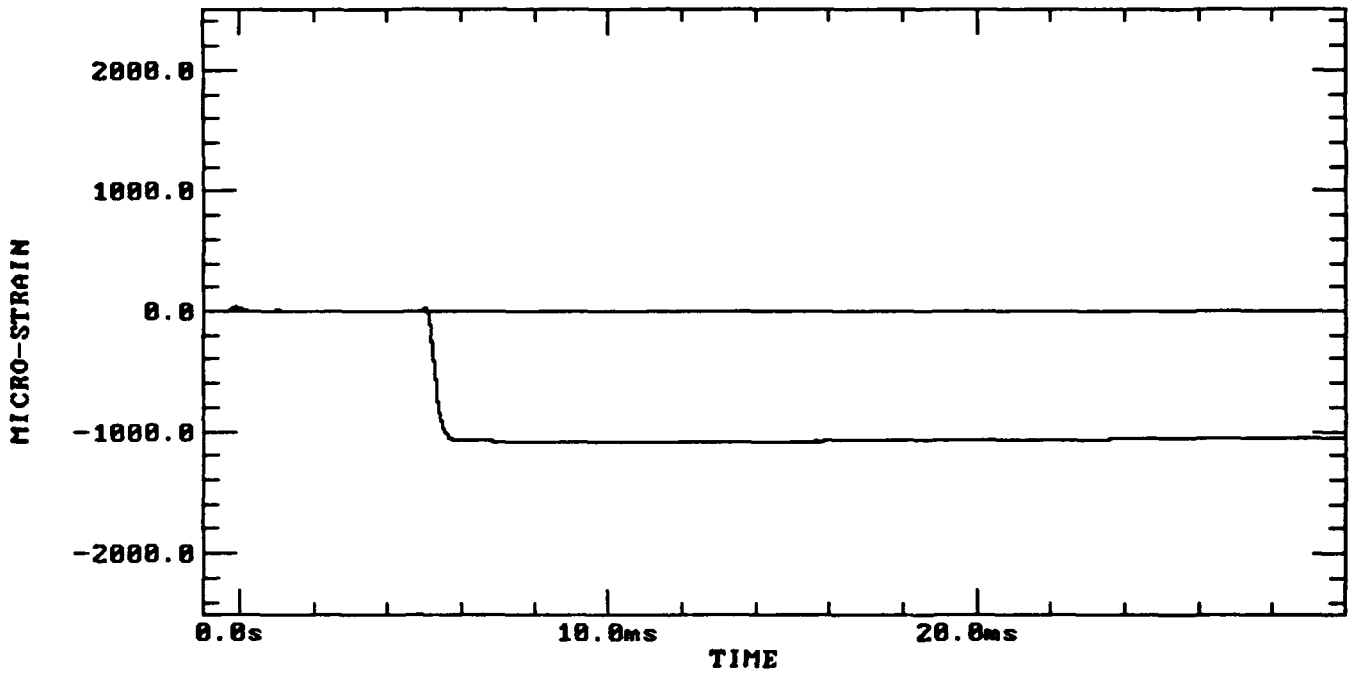
TIME HISTORY OF GAUGE B3C  
FILTERED AT 2000 HZ LOW PASS



# NPS PRECISION UNDEX TESTING

TEST 1

ZERO REPRESENTS DETONATION TIME

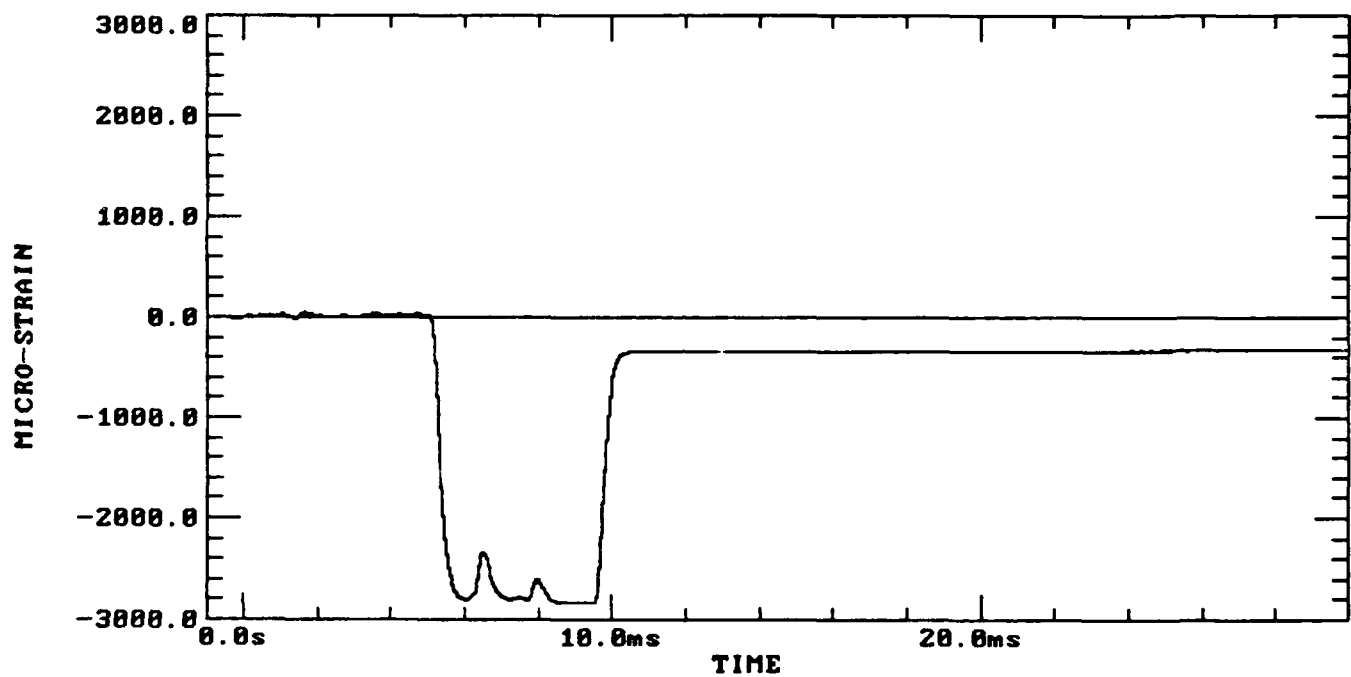


TIME HISTORY OF GAUGE C1C  
FILTERED AT 2000 HZ LOW PASS

# NPS PRECISION UNDEX TESTING

TEST 1

ZERO REPRESENTS DETONATION TIME



TIME HISTORY OF GAUGE C3C

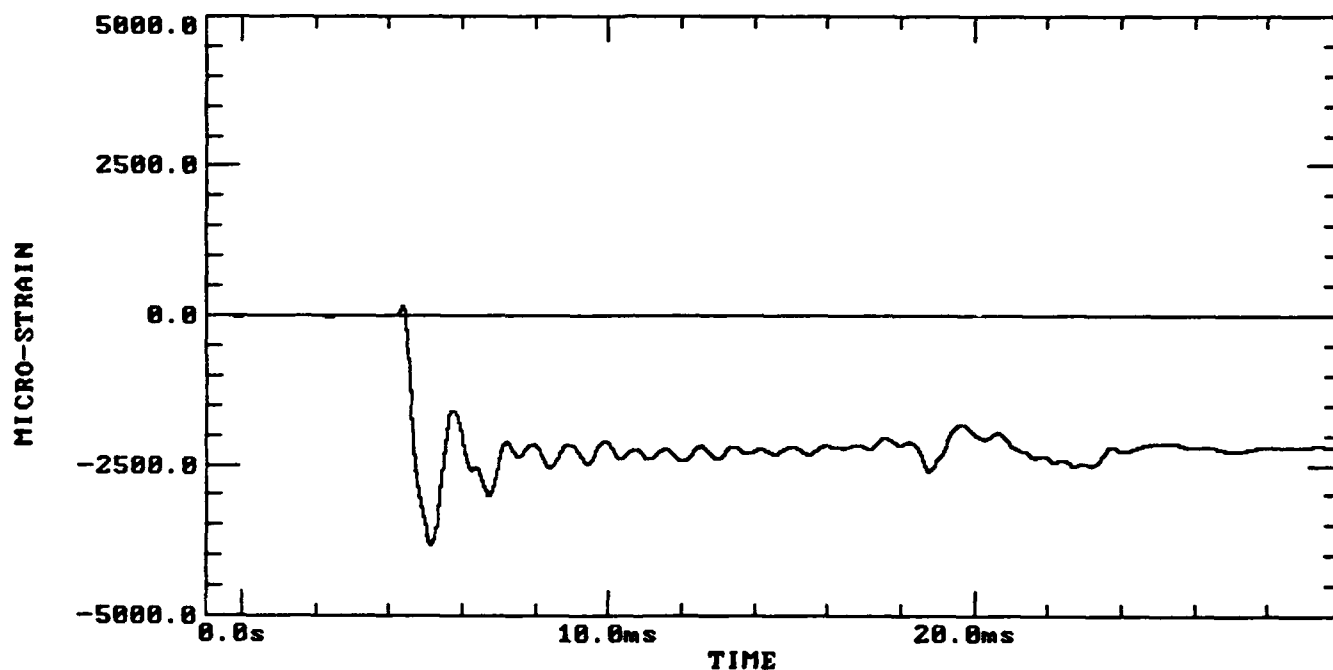
FILTERED AT 2000 HZ LOW PASS

*Test No. 2*

# NPS PRECISION UNDEX TESTING

TEST 2

ZERO REPRESENTS DETONATION TIME

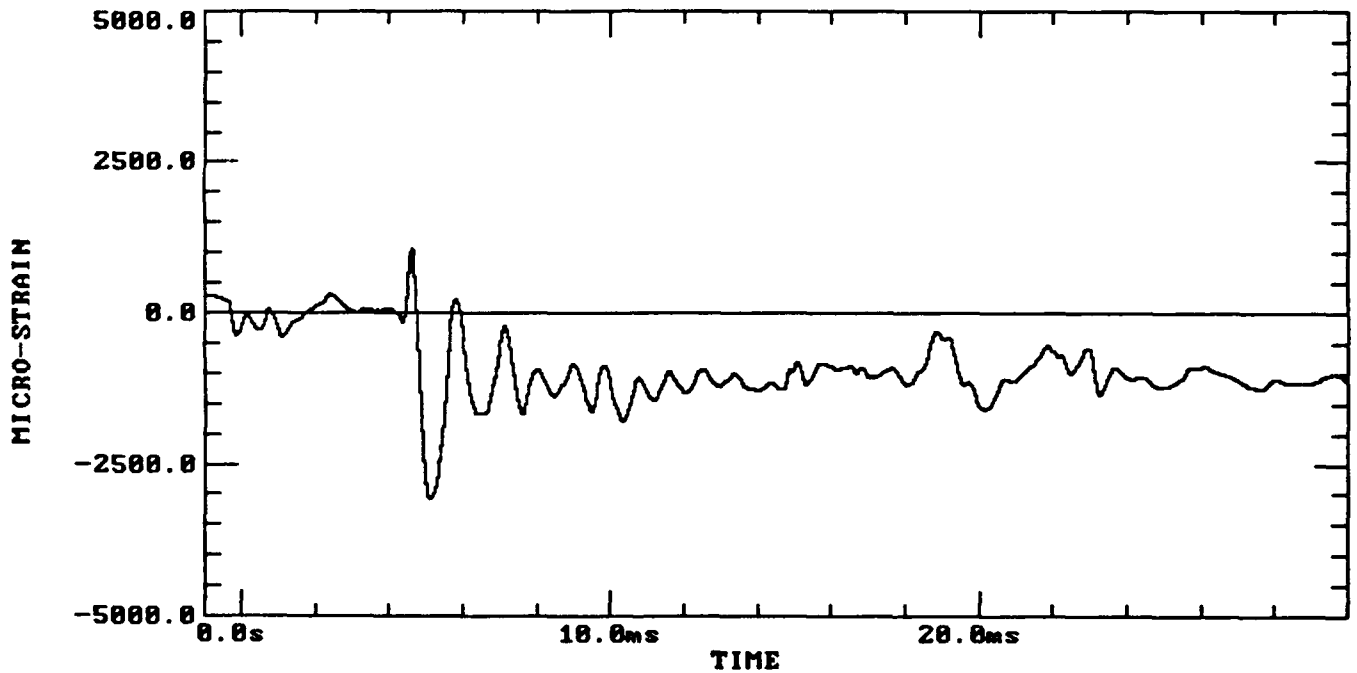


TIME HISTORY OF GAUGE A1L  
FILTERED AT 2000 HZ LOW PASS

# NPS PRECISION UNDEX TESTING

TEST 2

ZERO REPRESENTS DETONATION TIME

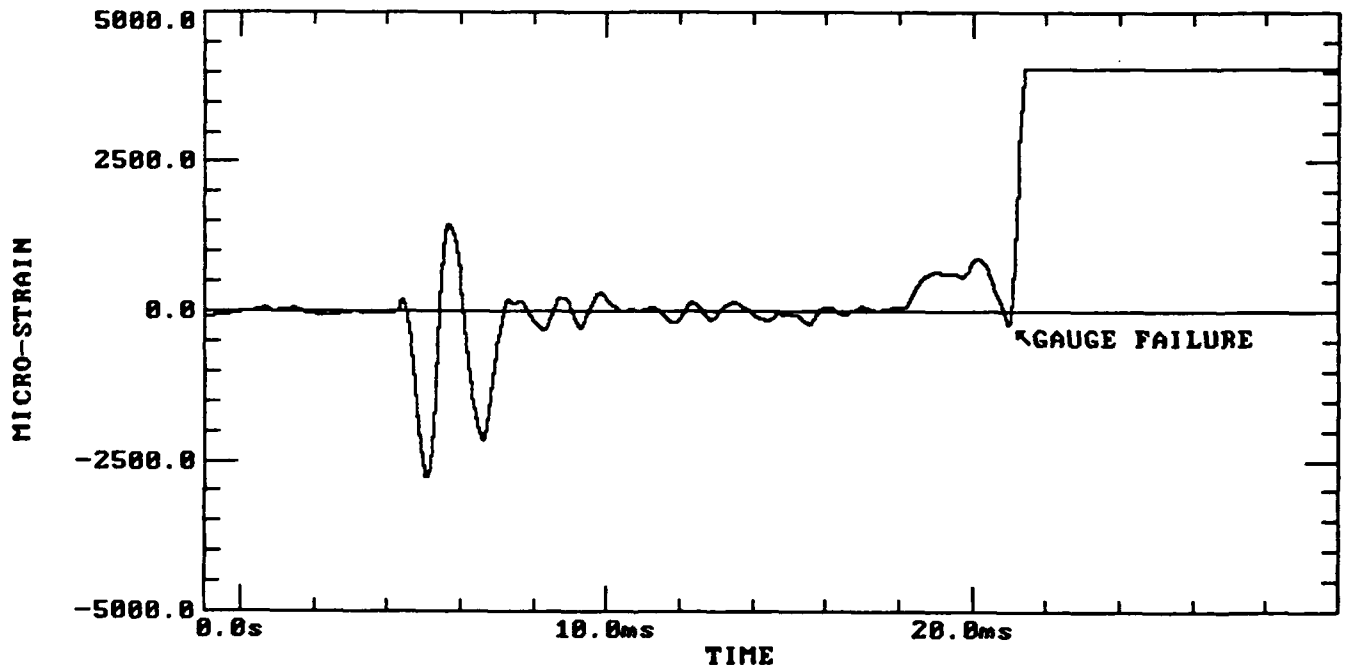


TIME HISTORY OF GAUGE A2L  
FILTERED AT 2000 HZ LOW PASS

# NPS PRECISION INDEX TESTING

TEST 2

ZERO REPRESENTS DETONATION TIME



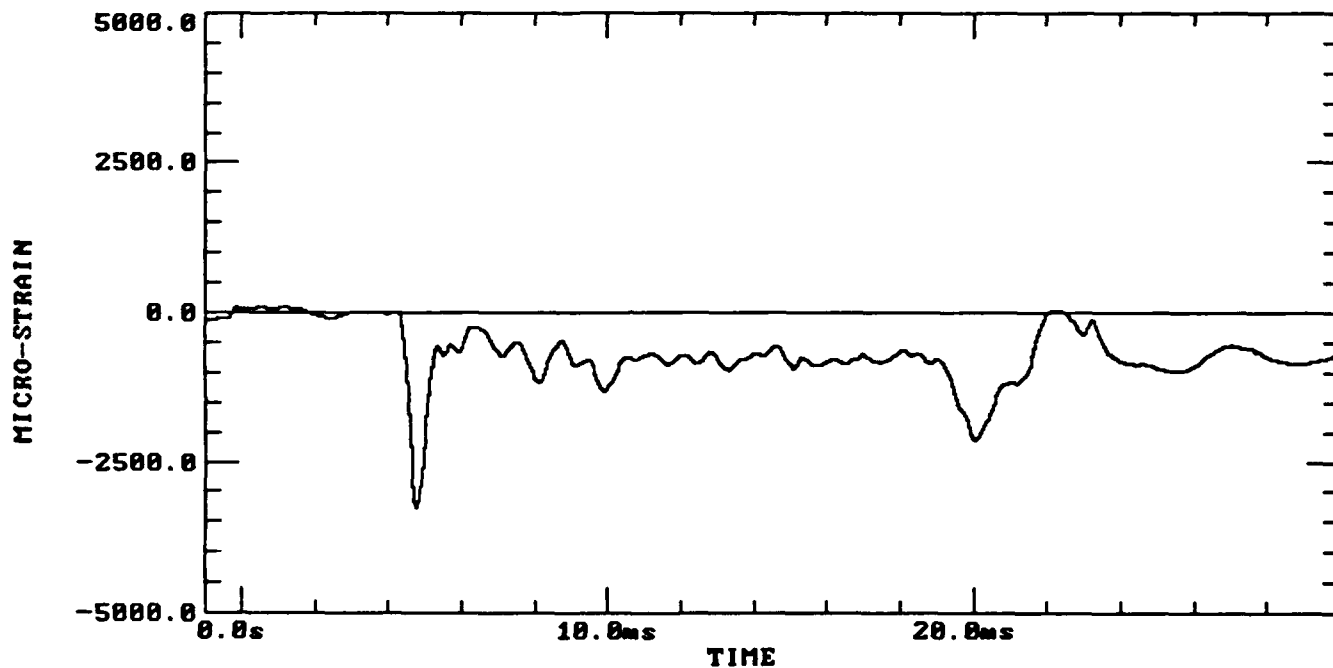
TIME HISTORY OF GAUGE B1L

FILTERED AT 2000 HZ LOW PASS

# NPS PRECISION UNDEX TESTING

TEST 2

ZERO REPRESENTS DETONATION TIME

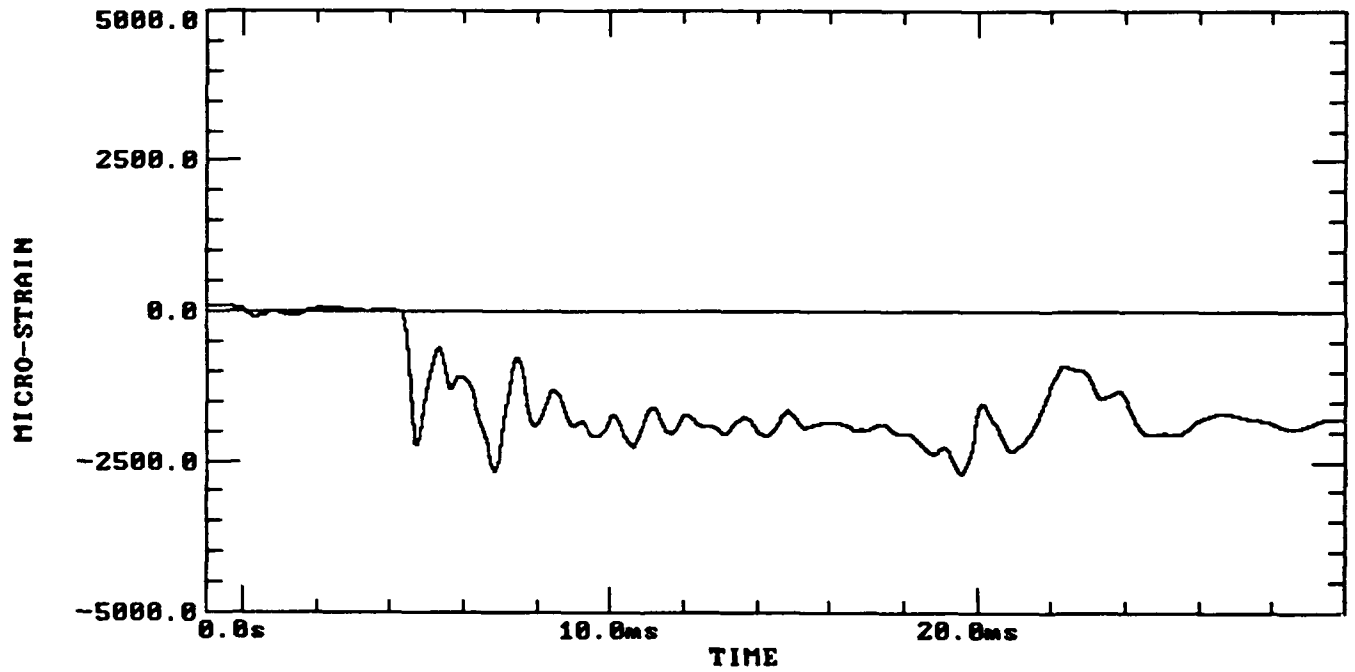


TIME HISTORY OF GAUGE B2L  
FILTERED AT 2000 HZ LOW PASS

# NPS PRECISION INDEX TESTING

TEST 2

ZERO REPRESENTS DETONATION TIME



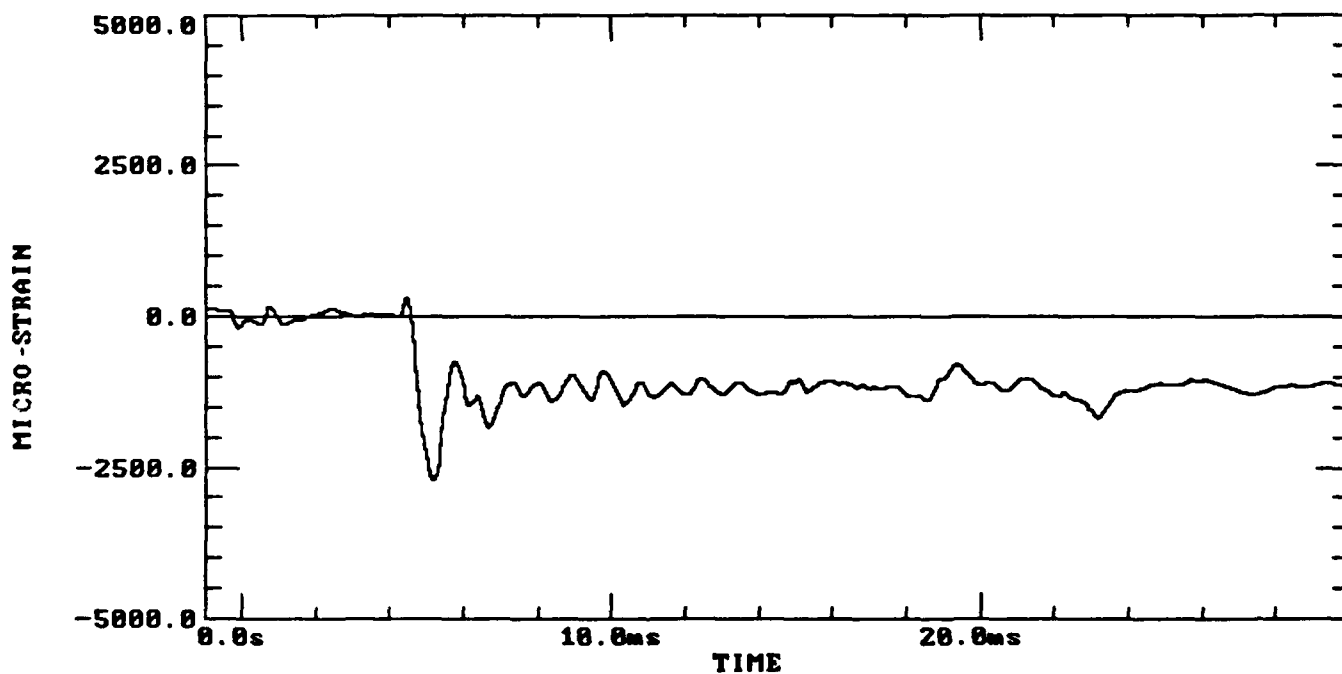
TIME HISTORY OF GAUGE B3L  
FILTERED AT 2000 HZ LOW PASS



# NPS PRECISION UNDEX TESTING

TEST 2

ZERO REPRESENTS DETONATION TIME

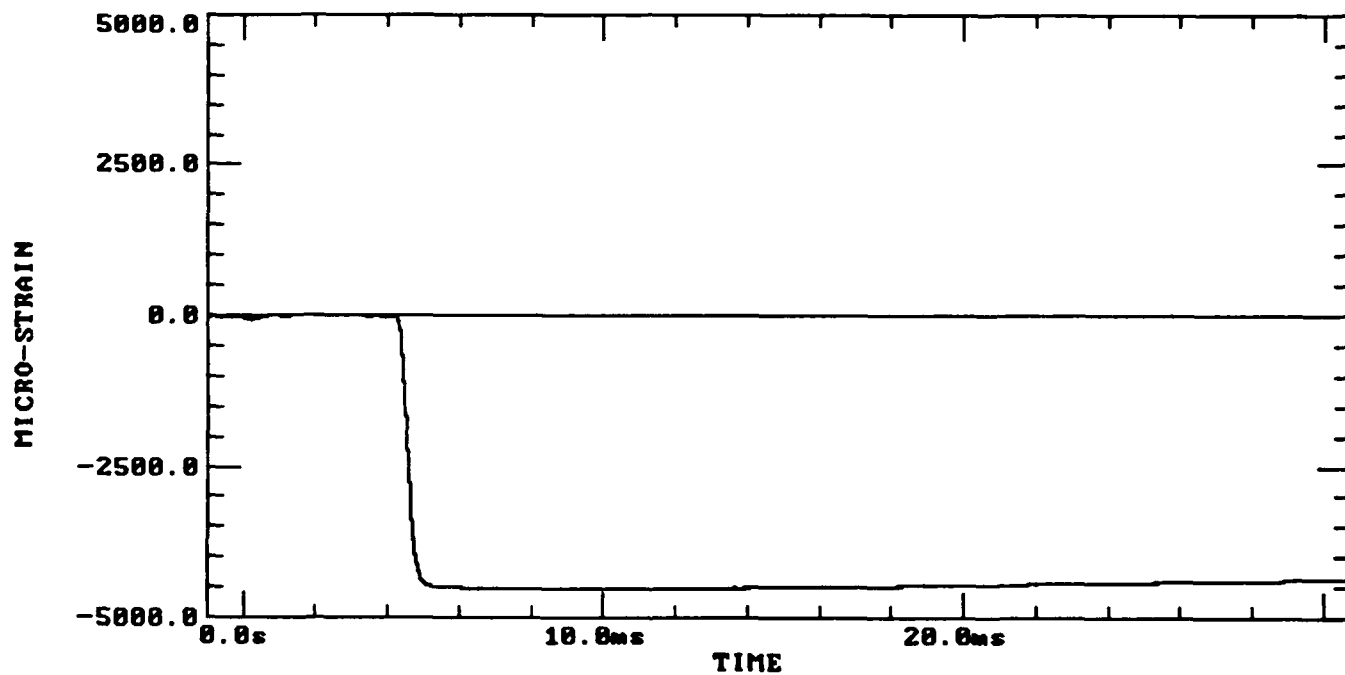


TIME HISTORY OF GAUGE C1L  
FILTERED AT 2000 HZ LOW PASS

# NPS PRECISION UNDEX TESTING

TEST 2

ZERO REPRESENTS DETONATION TIME

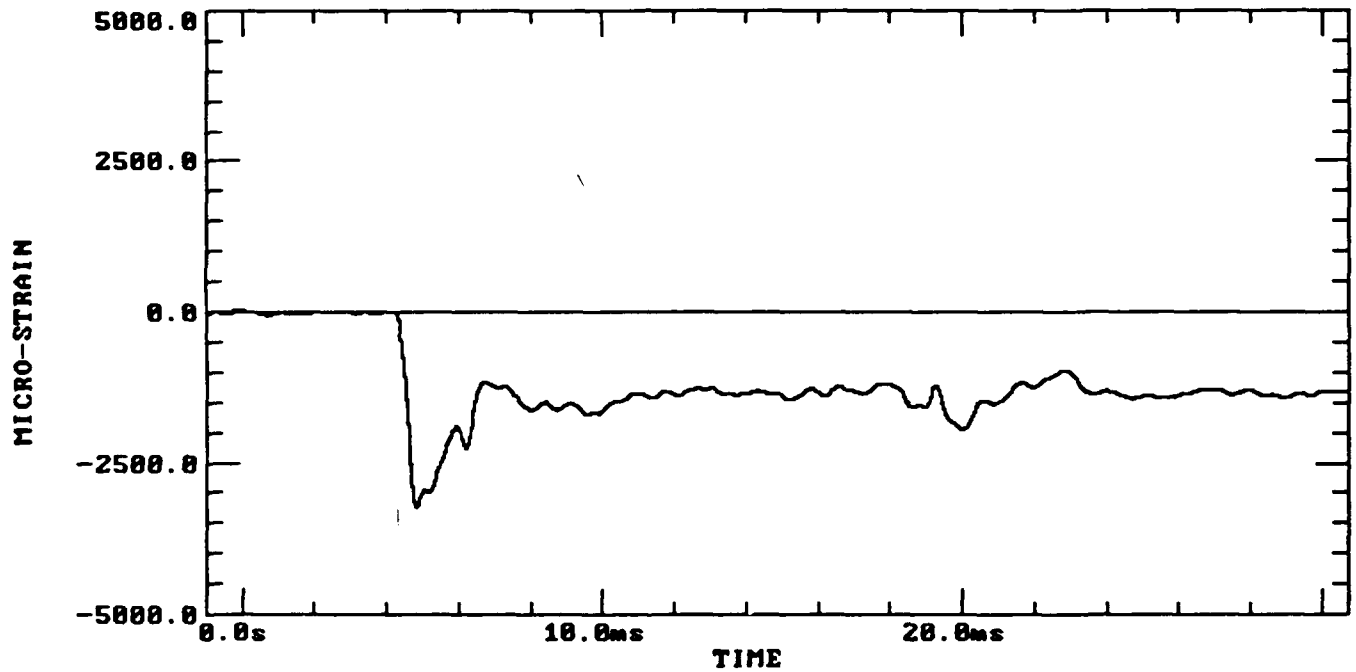


TIME HISTORY OF GAUGE A1C  
FILTERED AT 2000 HZ LOW PASS

# NPS PRECISION UNDEX TESTING

TEST 2

ZERO REPRESENTS DETONATION TIME

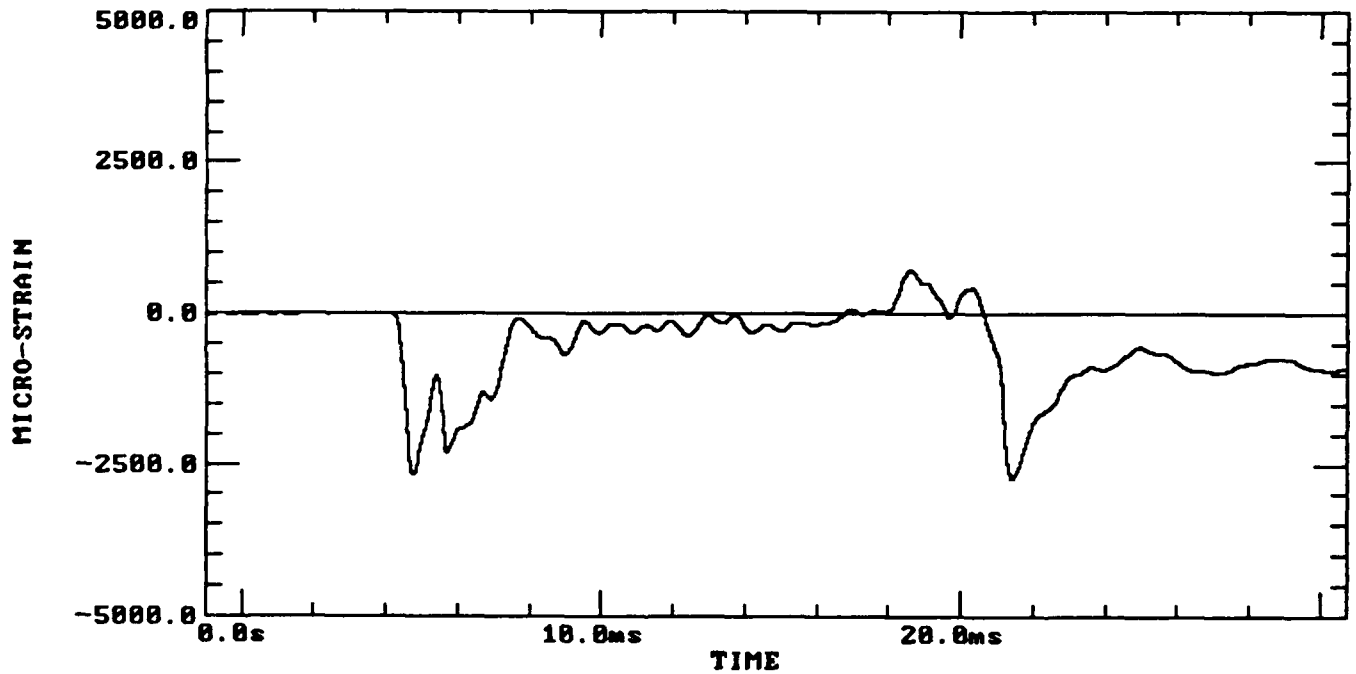


TIME HISTORY OF GAUGE AZC  
FILTERED AT 2000 HZ LOW PASS

# NPS PRECISION UNDEX TESTING

TEST 2

ZERO REPRESENTS DETONATION TIME

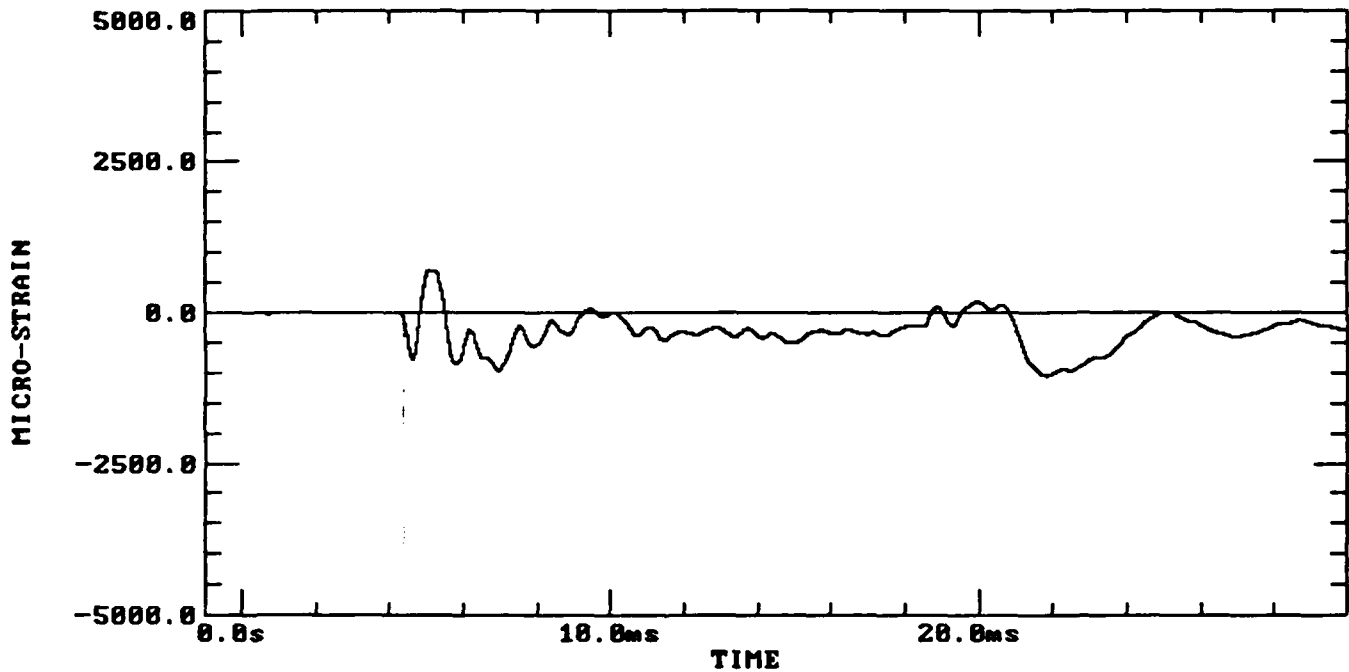


TIME HISTORY OF GAUGE B1C  
FILTERED AT 2000 HZ LOW PASS

# NPS PRECISION UNDEX TESTING

TEST 2

ZERO REPRESENTS DETONATION TIME

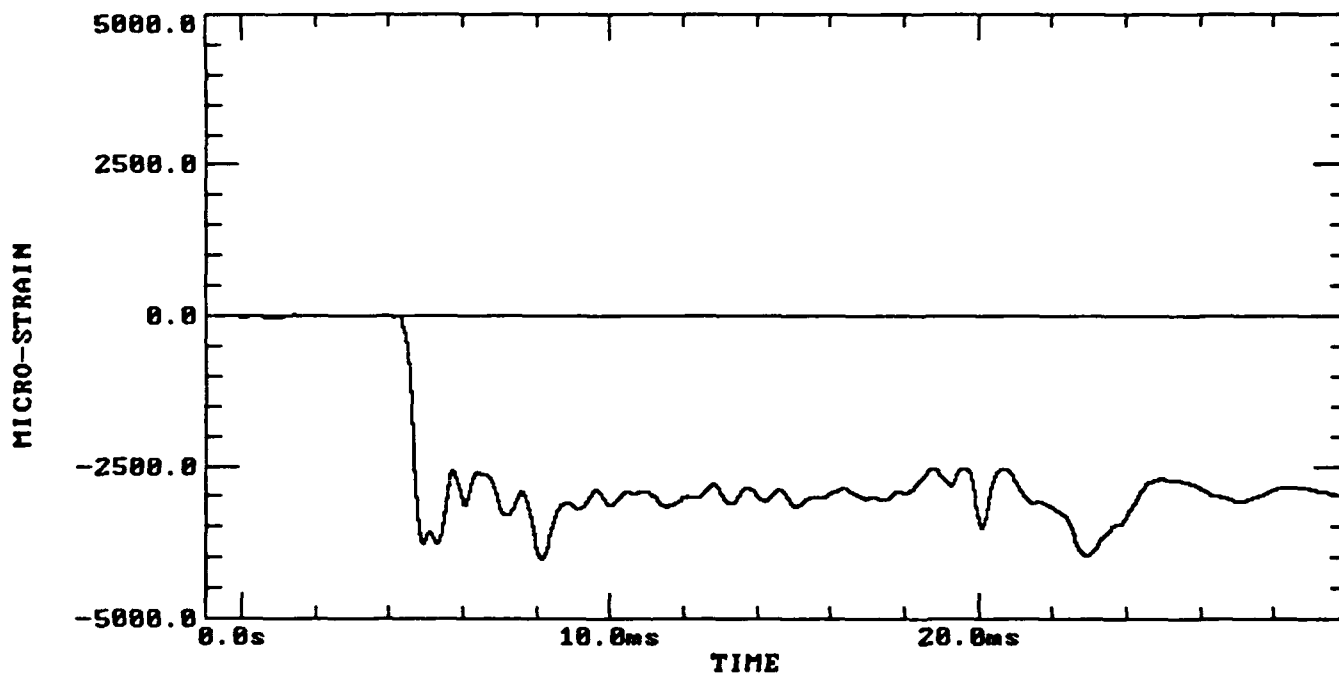


TIME HISTORY OF GAUGE B2C  
FILTERED AT 2000 HZ LOW PASS

# NPS PRECISION UNDEX TESTING

TEST 2

ZERO REPRESENTS DETONATION TIME

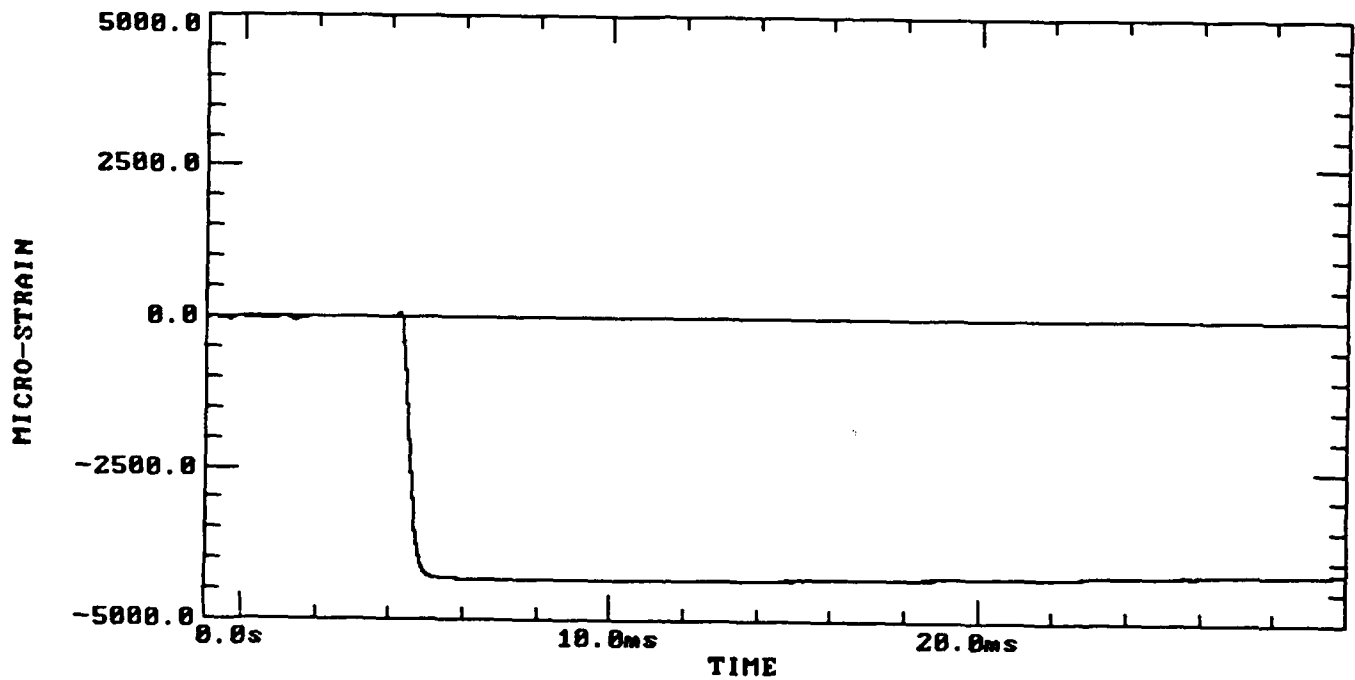


TIME HISTORY OF GAUGE B3C  
FILTERED AT 2000 HZ LOW PASS

# NPS PRECISION UNDEX TESTING

TEST 2

ZERO REPRESENTS DETONATION TIME

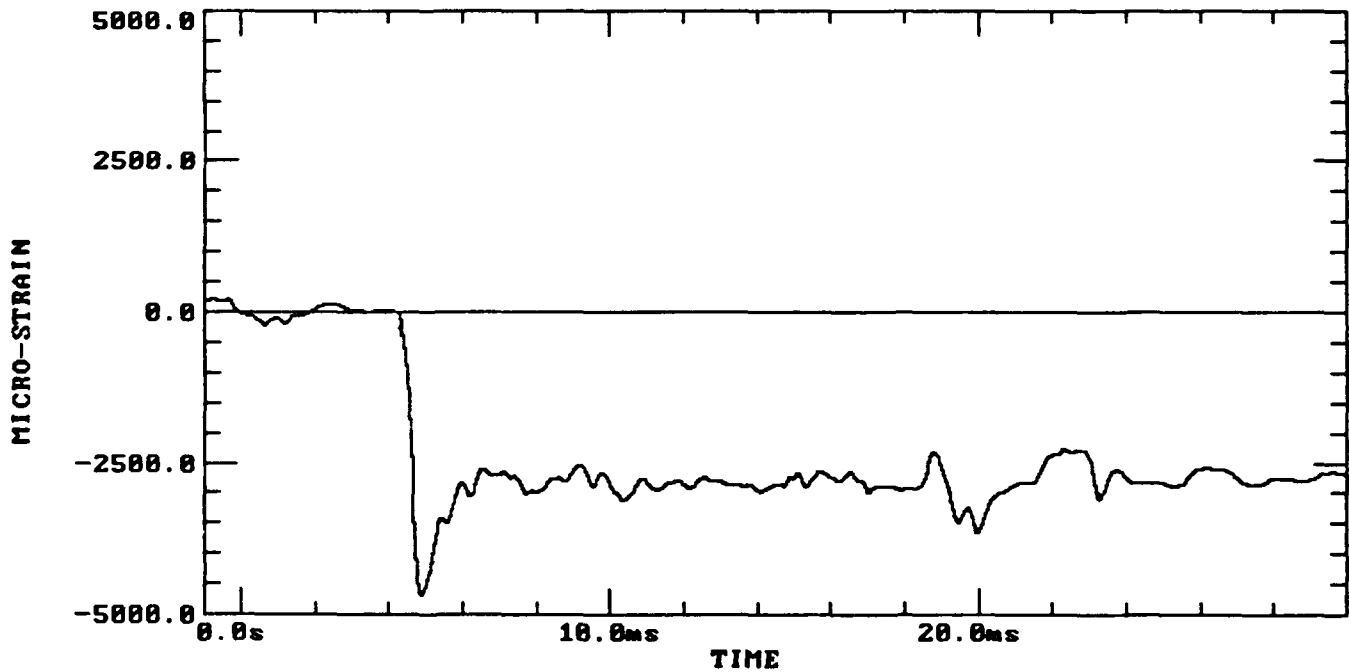


TIME HISTORY OF GAUGE C1C  
FILTERED AT 2000 HZ LOW PASS

# NPS PRECISION UNDEX TESTING

TEST 2

ZERO REPRESENTS DETONATION TIME



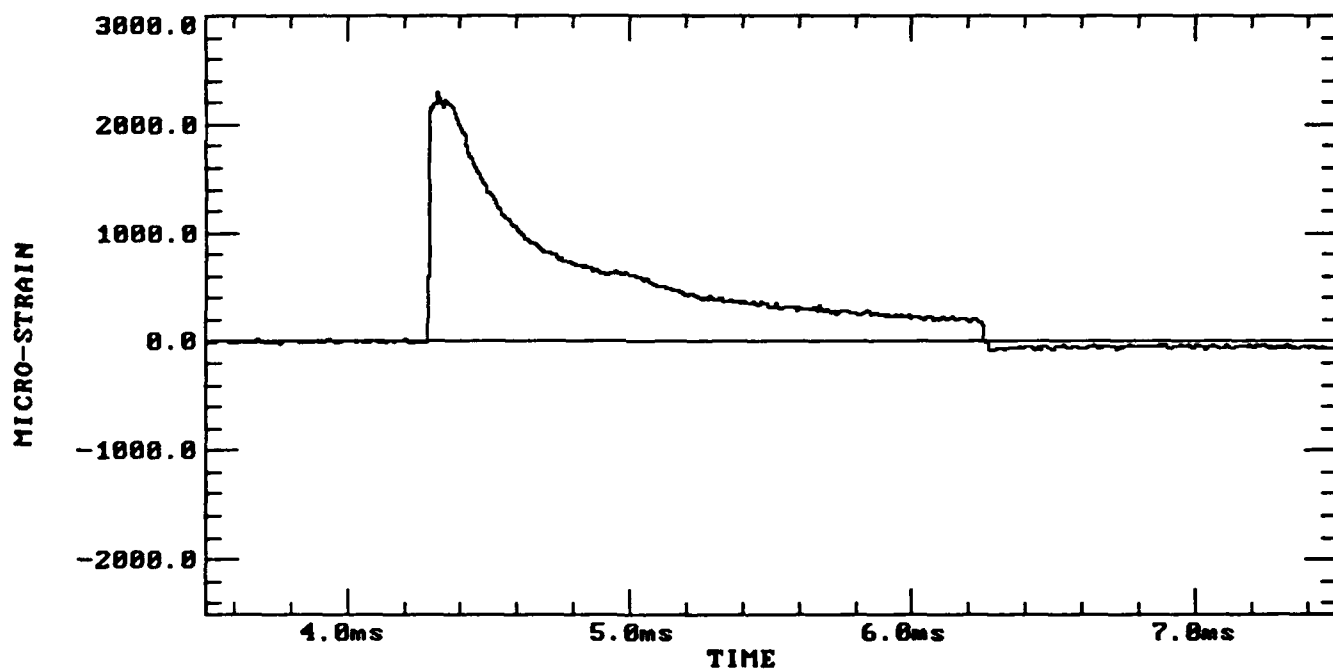
TIME HISTORY OF GAUGE C2C  
FILTERED AT 2000 HZ LOW PASS



# NPS PRECISION UNDEX TESTING

TEST 2

ZERO REPRESENTS DETONATION TIME



TIME HISTORY OF GAUGE P1

UNFILTERED

## INITIAL DISTRIBUTION LIST

	No. of Copies
1. Defense Technology Information Center Cameron Station Alexandria, Virginia 22304-6145	2
2. Library, Code 52 Naval Postgraduate School Monterey, California 93943-5002	2
3. Professor Y. W. Kwon, Code ME/Kw Department of Mechanical Engineering Naval Postgraduate School Monterey, California 93943	2
4. Professor Y. S. Shin, Code ME/Sg Department of Mechanical Engineering Naval Postgraduate School Monterey, California 93943	2
5. Dr. Thomas T. Tsai Defense Nuclear Agency 6801 Telegraph Road Alexandria, Virginia 22310	1
6. Dr. Kent Goering Defense Nuclear Agency 6801 Telegraph Road Alexandria, Virginia 22310	1
7. Mr. Douglas Bruder Defense Nuclear Agency 6801 Telegraph Road Alexandria, Virginia 22310	1
8. Dr. Phillip B. Abraham Office of Naval Research Mechanics Division, Code 1132 800 North Quincy Street Arlington, Virginia 22217-5000	1
9. Mr. Gene Remmers, ONT-23 Director, Office of Naval Technology 800 N. Quincy Street Arlington, Virginia 22217-5000	1
10. LCDR Padraic K. Fox RR 3, Box 181 Watertown, South Dakota 57201	1